Ionic Dynamics in Molecular Strong Field Ionization

A Dissertation presented

by

Arthur Xin Zhao

to

The Graduate School

in Partial Fulfillment of the

Requirements

for the Degree of

Doctor of Philosophy

in

Physics

Stony Brook University

August 2017

(include this copyright page only if you are selecting copyright through ProQuest, which is optional)

Stony Brook University

The Graduate School

Arthur Xin Zhao

We, the dissertation committe for the above candidate for the

Doctor of Philosophy degree, hereby recommend

acceptance of this dissertation

Professor Thomas Weinacht - Dissertation Advisor
Department of Physics and Astronomy

Assistant Professor Thomas Allison - Chairperson of Defense
Department of Physics and Astronomy
Department of Chemistry

Associate Professor Marivi Fernández-Serra
Department of Physics and Astronomy

Professor Bob Jones
Department of Physics, University of Virginia, USA

This dissertation is accepted by the Graduate School

Charles Taber
Dean of the Graduate School

Abstract of the Dissertation

Ionic Dynamics in Molecular Strong Field Ionization

by

Arthur Xin Zhao

Doctor of Philosophy

in

Physics

Stony Brook University

2017

This thesis studies the dynamics in strong field ionization (SFI) of small molecules, with a focus on the removal of electrons from multiple molecular orbitals, especially the mechanisms underlying the population of excited ionic states. To do this, we ionize molecular systems with ultrafast intense laser pulses ($\sim$ 10 fs, $>$ 10 TW/cm^2) and measure photoelectrons and photoions in coincidence with velocity map imaging (VMI) detection. The ionization is multiphoton by design, and due to its highly non-linear nature, intense laser pulses provide adequate temporal resolutions for probing molecular dynamics and certain electronic dynamics. VMI measures the momentum distribution of charged particles, and together with coincidence detection, the full kinematics of an ionization event can be reconstructed from the measurement. This allows for detailed studies of ultrafast spectroscopy, and allows us to discriminate two different pathways in producing excited ionic states either direct removal of an inner orbital electron or post-ionization excitation. For the latter, we carry out SFI experiments as well as theoretical simulations on a series of molecules, to study its dependence on electronic structure and the effect of non-adiabatic transition in populating excited ionic states, in particular, the importance of resonant transitions facilitated by nuclear dynamics.

Additional work is focused on the strong field molecular double ionization (DI), where we conjecture a connection between enhanced DI yields and the electronic structure in conjugated molecular systems.

To Science and my fellow Homo sapiens sapiens

Contents

List of Figures

List of Tables

List of Abbreviations and Symbols

SFI	Strong Field Ionization
VMI	Velocity Map Imaging
TOF	Time-of-flight
AOM	Acousto-optic Modulator
SI	Single Ionization
DI	Double Ionization
TDSE	Time-dependent Schrödinger Equation
RWA	Rotating Wave Approximation
CHD	Cyclohexadiene, C_5H_8
e	Elementary charge
$\hbar$	Reduced Planck's constant
a_0	Bohr radius

Publications

Péter Sándor, Arthur Zhao, Tamás Rozgonyi and Thomas C. Weinacht. Strong field molecular ionization to multiple ionic states: direct versus indirect pathways *J. Phys. B* 47, 124021 (2014)

Arthur Zhao, Péter Sándor, Tamás Rozgonyi and Thomas C. Weinacht. Removing electrons from more than one orbital: direct and indirect pathways to excited states of molecular cations. *J. Phys. B* 47, 204023 (2014)

Péter Sándor, Arthur Zhao, Vincent Tagliamonti, Matthia Rukenbauer, Philipp Marquetand, Tamás Rozgonyi and Thomas C. Weinacht. Strong-Field Molecular Ionization in the Impulsive Limit: Freezing Vibrations with Short Pulses. *Physical Review Letters*, 116, 063002 (2016)

Vincent Tagliamonti, Péter Sándor, Arthur Zhao, Philipp Marquetand, Tamás Rozgonyi and Thomas C. Weinacht. Nonadiabatic Dynamics and Multiphoton Resonances in Strong Field Molecular Ionization with Few Cycle Laser Pulses. *Physical Review A* (2016) 051401(R)

Arthur Zhao, Péter Sándor and Thomas Weinacht. Coincidence velocity map imaging using a single detector. *The Journal of Chemical Physics* 147, 013922 (2017)

Vincent Tagliamonti, Brian Kaufman, Arthur Zhao, Tamas Rozgonyi, Philipp Marquetand, and Thomas Weinacht. Time-resolved measurement of internal conversion dynamics in strong-field molecular ionization. (in press)

Arthur Zhao, Péter Sándor, Vincent Tagliamonti, Tamás Rozgonyi,, Philipp Marquetand, and Thomas Weinacht. Ionic Dynamics Underlying Strong Field Dissociative Molecular Ionization. (in press)

Arthur Zhao, Martin van Beuzekom, Bram Bouwens, Dmitry Byelov, Irakli Chakaberia, Chuan Cheng, Erik Maddox, Andrei Nomerotski, Peter Svihra, Jan Visser, Vaclav Vrba and Thomas Weinacht. Coincidence Velocity Map

Imaging Using Tpx3Cam, a time stamping optical camera with 1.5 ns timing resolution. (submitted)

Acknowledgements

Praise be to **EVOLUTION**, who, with the majesty of her speciation, anagenesis and extinction, has endowed me with sense, reason and logic. Best respect and peace be unto her messenger **Charles Darwin**, and his cautious and rational followers.

Thanks to Zaofu, a talented and brave charioteer in Chinese mythology, the ancestor of all with the surname Zhao.

Thanks to my parents and my family, who have created and facilitated my existence.

Thanks to TCW, who, as an adviser and a friend, has enlightened and guided me to achieve the highest degree in science. The times we've worked together and the discussions we've had regarding physics, life and everything, remain to be some of my most pleasant memories in grad school.

Thanks to my collaborators, group members and colleagues in the AMO labs, PS, TR, PM, SM, CC, AN, SH, YSL, MC, DG, ON, DS, TA, BJ, LK, JR, et al., without whom, this thesis would not have been possible. They have taught me a great deal and created a friendly and supportive working environment.

Thanks to those whom I've fortunately acquainted at SBU, ML, RV, ON, KC, AA, JP, GS, ASA, RL, ASC, SD, GS, DS, LD, et al. It's been such a pleasure and I'm proud to call you my friends.

Thanks to CM, JW and RS, whose friendships I shall always cherish.

Thanks to the government of the United States of America for funding my study and research work. Your support is essential in advancing fundamental science and the human condition.

Chapter 1

Introduction

The microscopic motion of electrons and ions are responsible for many physical, chemical and biological phenomena observed in nature, such as light absorption/emission, changes in molecular bonds and chemical compositions, and bioinformation storage and transportation. The development of adequate tools to probe electron dynamics in atoms and molecules can help us better understand these processes and possibly provide means of manipulation, which can ultimately lead to technological innovations. One such tool that relies on light-matter interactions is molecular strong filed ionization (SFI), which utilizes ultrafast intense laser fields to initiate and probe ionization and subsequent dynamics in molecules. The main merit of this approach lies in its time resolution due to the highly non-linear nature of the interaction. Generally speaking, in order to study the structure and dynamics of atomic and molecular systems, we need a physical quantity of comparable temporal gradient and sufficient interaction strength. The electric field in a hydrogen atom is $E = e/(4\pi\epsilon_0 a_0^2) \approx 5.1 \times 10^9$ V/cm, corresponding to an intensity of 3.5×10^{16} W/cm^2. Intense laser pulses can be focused into a volume comparable to its wavelength (sub-μm), producing an electric field comparable to that within an atom or molecule [3, 4]. The characteristic period of a Bohr electron orbital is about 2.4×10^{-17} s and the few meV energy spacing between typical molecular vibrational levels implies a tens of femtoseconds (1 fs = 10^{-15} s) characteristic time ($\Delta T \Delta E \approx \hbar$). Thanks to the technological advances in ultrafast optics, now we have access to diffraction-limited laser pulses of a few oscillation cycles (~ 10 fs). What's more important is the ionization itself, which is highly non-linear in nature. In the perturbative limit where the field is not too strong, ionization rate has

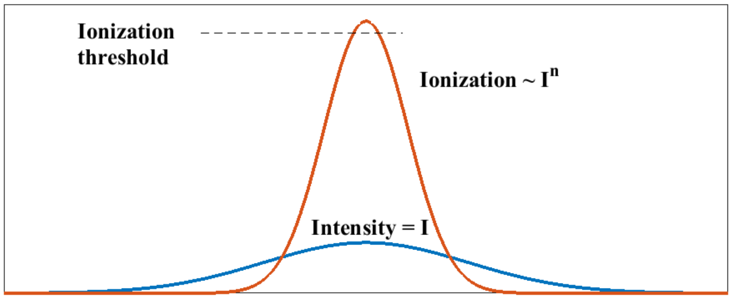

Figure 1.1: Intensity dependence of multiphoton ionization.

an I^n intensity dependence, where I is the field intensity and n is the number of photons required for ionization. As a result, ionization first takes place at or near the peak of the field (see Fig.1.1), corresponding to a time scale of a few or even sub-fs. In fact, most SFI is non-perturbative, which implies an even higher non-linearity and shorter time resolution. This opens the door for many interesting studies, such as probing and control of excited states dynamics[5, 6, 7, 8, 9], ultrafast imaging of molecular structure [10, 11] and plasma acceleration [12, 13]. Electrons liberated during SFI are still subject to the intense field, some of which can be accelerated to re-collide with the ion core to emit high harmonics into the deep UV regime. This makes SFI an important step towards attosecond (as) science (1 fs = 1000 as), where one can study fast electronic dynamics [14, 15, 16]. In addition to its time resolution, ionization is always possible in SFI so there is no dark state. From the signal detection point of view, ionization as a probe produces charged particles, which are relatively easy to collect. When the pulse envelope is of a few optical cycles long, the carrier-envelope phase (CEP) becomes relevant since the instantaneous field strength at the peak of the pulse can vary depending on the CEP. CEP is important in attosecond science and in studying electron dynamic in SFI. All data presented in this thesis are obtained as CEP-averaged results which are sufficient since we are mostly interested in ionic dynamics.

In this thesis, we focus on the dynamics in molecular ions following SFI of small molecules.

Strong field generally refers to the regime when the perturbative description does not give an accurate account of the ionization rate. This could be the case when there are resonant intermediate states. More importantly, when the light field is intense, all states experience a non-perturbative dynamic shift in energy, the so-called *AC Stark shift*, which makes a perturbative treatment difficult. This shift becomes more significant with increasing field strength, and affects weakly-bound Rydberg states more than tightly-bound valence states because the former are usually far-detuned. In the case of a free electron in an alternating field, this shift is termed *ponderomotive shift*, which is equal to the cycle-averaged quiver energy due to its oscillating motion:

$$\begin{aligned} U_p &= \frac{1}{2} m\omega^2 <x^2> \\ &= \frac{e^2 E_0^2 (1+\xi^2)}{4m\omega^2} \end{aligned} \tag{1.1}$$

where the angle bracket indicates cycle-averaging and ξ is the ellipticity with $\xi = 0$ corresponding to linear polarization and $\xi = \pm 1$ corresponding to circular. Since a weakly-bound Rydberg electron far away from the ion core behaves in a similar fashion as a free electron, we should expect the ionization potential Stark shifts up by the same amount as U_p (see Fig 1.2). Furthermore, since the ion is still subject to the laser field after ionization, an additional amount of energy is required for ionization, which is equal to the Stark shift of the ion, denoted as E_S. This leads to a modification of the conservation of energy in the photoelectric effect:

$$KE = n\hbar\omega - I_p^i - U_p - E_S^i \tag{1.2}$$

where KE is the kinetic energy of the liberated electron, n is the total number of photon absorbed and $\hbar\omega$ is the photon energy [17, 18]. The superscript i indicates the i^{th} excited ionic state. From this we expect the photoelectron energy should vary with intensity since the last two terms in the equation do so. However, an intermediate neutral state can Stark shift into resonance to produce resonance enhanced ionization, as shown in Fig 1.2. Since this resonance only occurs at a specific intensity, the resonant peak in the photoelectron spectrum manifests itself as a narrow peak which appears at a particular intensity and remains fixed in energy. This non-perturbative phenomenon is referred to as the Freeman resonance [19] .

A note on the U_p: Eq. 1.2 is valid under the assumption that the laser pulse is short such that as the pulse leaves the ionization region, the photoelectron's U_p is returned to the field. When the pulse is long comparing to the

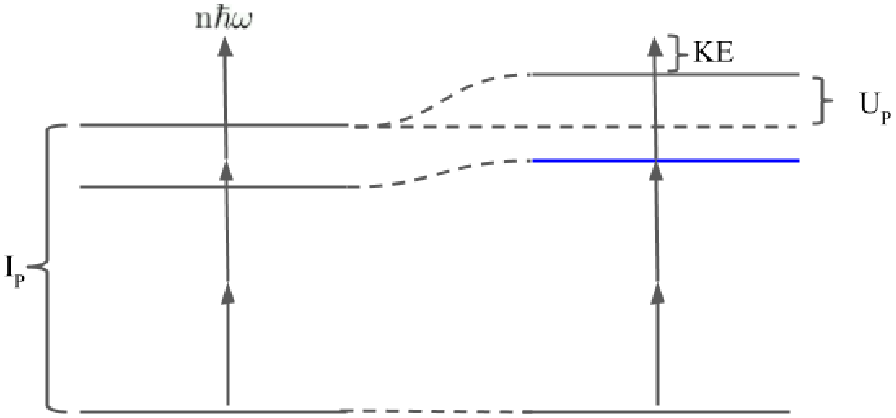

Figure 1.2: AC-Stark shift and Freeman resonance. Intermediate states and the continuum shifts upwards in energy with respect to the ground state in an intense electric field. Freeman resonance occurs when an intermediate state shifts into resonance (in the figure, a 2-photon resonance to the state denoted by the blue bar.) due to AC-Stark shift. The continuum is shift by U_p, known as the ponderomotive potential.

time for the liberated electron to escape the focus, the electron rides down the spatially varying potentials in the focus of the laser field, and transforms its U_p into kinetic energy [19, 20, 21, 22] .

Another interesting phenomenon that occurs in strong fields is above-threshold ionization (ATI)[17, 23], which happens when the liberated electron absorbs more-than-the-required number of photons during ionization (see Fig 1.3). This appears in the spectrum as a series of similar peaks equally spaced by one photon energy. It has been observed that with increasing intensity, higher order ATI peaks (larger number of excess photon absorption) can be as important as lower order ones[24]. This is another indication of the breakdown of perturbation theory, which requires the terms of higher order to get progressively smaller.

For even stronger electric fields that are comparable to the atomic or molecular Coulomb field, the electron's potential well is distorted so much that tunneling becomes important (Fig 1.3). It's common to use the so-called Keldysh parameter[25] to distinguish this mechanism from the above-

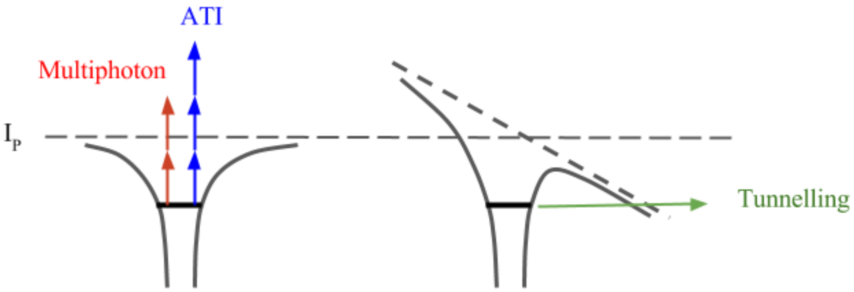

Figure 1.3: Multiphoton and tunneling ionization. Above-threshold ionization (ATI) occurs when more-than-the-required number of photons are absorbed during ionization. When the field strength is comparable to the internal electric field strength inside the atom/molecule, the potential well is tilted to enable tunneling ionization.

mentioned multiphoton ionization:

$$\gamma = \sqrt{\frac{I_p}{2U_p}} \tag{1.3}$$

$$= \frac{\omega_{\text{laser}}}{\omega_{\text{tunneling}}} = \frac{\omega}{\frac{eE_0}{\sqrt{2mI_p}}} \tag{1.4}$$

where $\omega_{tunneling}$ is a characteristic tunneling rate, calculated as the ratio of the electron velocity $\sqrt{\frac{I_p}{2m}}$ and the barrier width $\frac{I_p}{eE_0}$. γ can be interpreted as a comparison of atomic quantities and external field quantities, either in energy (1.3) or in time (1.4). If $\gamma << 1$, then the field interaction energy ($\sim U_p$) is larger than the atomic interaction ($\sim I_p$) and the probability for tunneling becomes significant within a laser cycle ($\omega_{tunneling} >> \omega$). We say the ionization is in the *tunneling* regime. One the contrary, when $\gamma >> 1$, the potential barrier is not substantially suppressed and the suppression time is too short to allow significant tunneling. This is called the *multiphoton* regime. Note that the word *multiphoton* here refers specifically to the parameter space where $\gamma >> 1$. All ionizations considered in this thesis are "multi-photon" in the sense that $I_p/\omega >> 1$, since they involve transitions from bound neutral states to the continuum ($\sim$ 10 eV) via coupling to near-IR (800 nm $\sim$ 1.6 eV) laser field, and thus the absorption of multiple photons from the field.

Since the early works by Keldysh[25], Faisal[26] and Reiss[27], much effort has been devoted to the theoretical understanding of SFI. Most methods calculate the ionization rate based on quasistatic and semiclassical tunneling in the limit $\gamma << 1$, and require strong field approximation and single-active-electron approximation[25, 28, 29], which ignores the Coulomb interaction between the freed electron and the ion core and assumes the field only acts on one electron[30]. In the *multiphoton* regime where $\gamma >> 1$, perturbation theory works well only when the field interaction is weak, which is generally not true in SFI. In fact, because the SFI observed in our experiments often corresponds to $\gamma \sim 1$, both *tunneling* and *multiphoton* characters in the Keldysh sense are important. In principle, one can obtain an accurate description of SFI by solving the time-dependent Schrödinger equation (TDSE), but it's computationally challenging, even if possible, and it doesn't always provide intuitions for understanding the problem or building theoretical models. As a result, it's important to carry out comprehensive experimental measurements in order to fully characterize molecular SFI and help develop better theoretical models.

In this thesis, we focus on identifying different SFI channels (which ionic states are populated) by measuring the full kinematics of photoelectrons and photoions in coincidence, and understanding the mechanism governing ionic dynamics in SFI. In addition, we conjecture a correlation between the electronic orbital structure and enhanced yield in strong field molecular double ionization.

The thesis is structured as follows: Chapter 2 describes the experimental apparatus. Chapter 3 and 4 discusses SFI and post-ionization excitation in polyatomic molecules, utilizing coincidence velocity map imaging (VMI) detection. Chapter 5 studies strong field molecular double ionization. Chapter 6 concludes and discusses future prospects.

Chapter 2

Experimental Apparatus and Design

In this chapter, we describe the ultrafast light source and various measurement techniques to study molecular SFI. Our light source is an amplified Ti:Sapphire laser system equipped with a gas cell filamentation setup, which produces a broadband spectrum that supports sub-10 fs pulses. An acousto-optic modulator (AOM) is used to compress and shape the pulse before it's sent to the science chamber 2.1 . In all experiments presented in this thesis, we measure photoelectrons and/or photoions using velocity map imaging (VMI) detection, which gives the transverse momentum of a charged particle. Additional design allows the detection of electrons and ions in coincidence 2.2 . We show two examples to illustrate the applications of coincidence and non-coincidence detection 2.3 . Finally, we introduce a time-resolved fast camera 2.4 and describe the algorithm used to recover the 3D momentum distribution from the measurement 2.5.

2.1 Light Source

The two-stage amplified Ti:Sapphire laser system produces 30 fs (FWHM intensity), 1 mJ pulses at 1 kHz, with a central wavelength of around 780 nm. First, a Kerr-lens modelocked oscillator (KM Labs) is pumped by a Coherent Verdi V5 laser to produce ultra-short pulses. Then, these pulses are stretched in time, sent through a multi-pass ring-cavity amplifier (KM Labs, HAP-AMP) pumped by a Q-switched Nd:YLF green laser(Photonics DM-

20), and finally compressed into high-power ultrashort pulses. This technique is known as chirped pulse amplification.

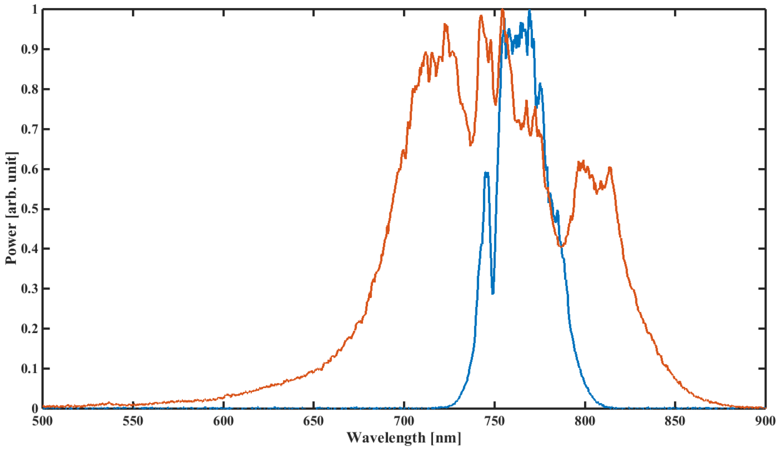

Figure 2.1: Optical spectra for amplified (blue) and filamentation (red) beam. The latter is obtained by focusing the former into a 1-m long Ar gas cell, where self-phase modulation generates new frequencies.

The amplified pulse is then focused into a 1 m long Argon cell ($\sim$ 1 atm) to produce a filament, as a result of self-focusing and plasma scattering [31, 32]. Due to the Kerr effect, high intensity at the focus modifies the refractive index: $\Delta n = n_2 I(t)$, $I(t)$ being the instantaneous field intensity. This change in turn causes a time-dependent phase delay, which generates new frequency components according to $\omega = \frac{\mathrm{d}\phi}{\mathrm{d}t}$. This phenomenon is termed self-phase modulation and in our case, it broadens the spectrum to over 150 nm (FWHM), which is capable of supporting a sub-10 fs pulse (Fig. 2.1). The output beam is collimated into pulse shaper for compression.

The pulse shaper (see Fig. 2.2)utilizes an acousto-optic modulator(AOM) and is set up in a 4f-configuration composed of two curved mirrors and two diffraction gratings. Different frequency components of the input beam are separated via a grating and then collimated and focused via a curved mirror into the AOM in the Fourier plane, where sound wave induced Bragg diffraction modulates their amplitudes and phases. Then they are recombined via the second curved mirror and grating to form a collimate output beam. Since the pulse shaping is linear – multiplicative amplitude and additive phase modulations, it can be used simultaneously as both a compressor

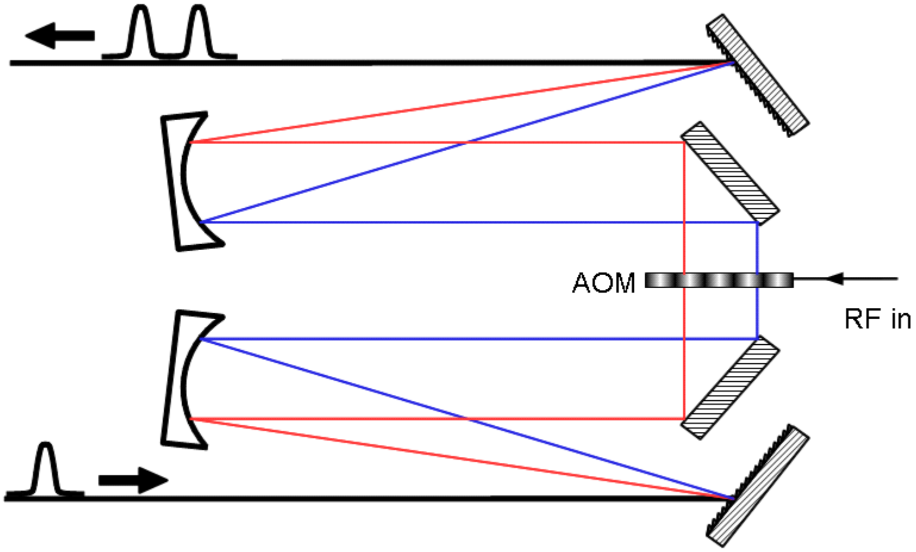

Figure 2.2: Pulse shaper in a 4f-configuration utilizing an AOM.

for the filament broadband beam and an active pulse shaping element. For instance, the pulse shaper is often used to digitally control the pulse intensity via amplitude modulation. It's also convenient to cut off certain spectral components to produce longer pulses and/or shift central frequencies. The overall efficiency of the pulse shaper for non-shaped pulse is about 15%. More details on the laser system, including the filament generation and pulse shaping, can be found in earlier theses from this lab[33, 34, 35].

2.2 Coincidence Velocity Map Imaging

The output beam from the pulse shaper is directed into a vacuum chamber where it interacts with an effusive beam of gas phase molecular samples. The vacuum chamber is backed by a turbo pump with a base pressure of $\sim 10^{-9}$ Torr, and the operating pressure usually ranges from $\sim 10^{-8}$ to $\sim 10^{-6}$ Torr, depending on the experiment. The beam is focused with a 5cm curved mirror in the center of a set of electrostatic lens, which extracts charged particles and sends them through a time-of-flight (TOF) tube onto a dual stack of microchannel plates (MCP) in chevron configuration (Fig 2.3) . The TOF tube is enclosed in μ-metal to shield the earth's magnetic

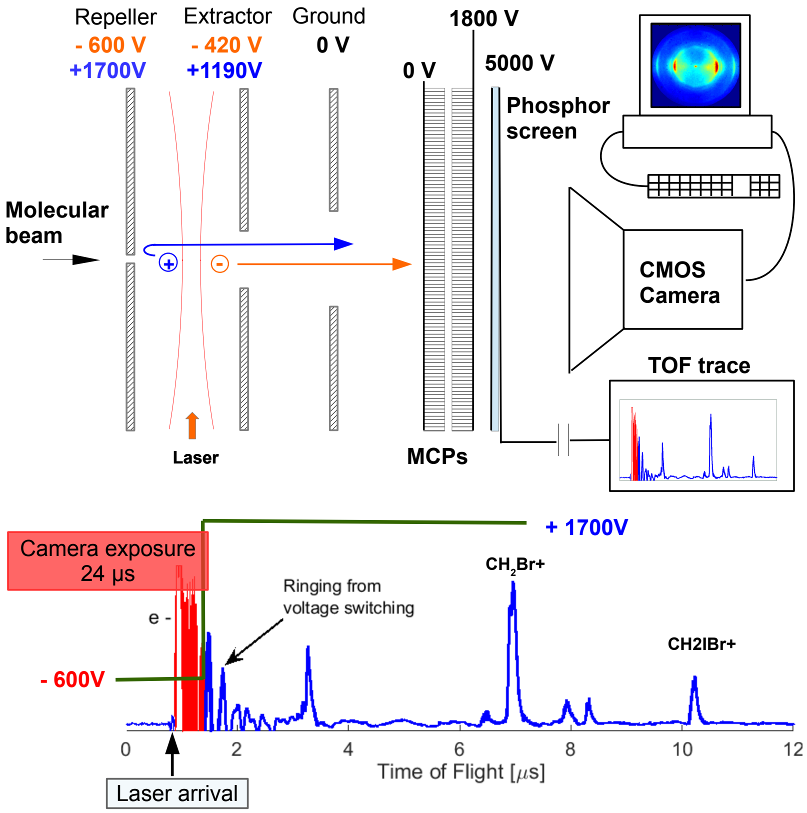

Figure 2.3: Apparatus for coincidence VMI and illustration of the voltage switching timeline. The voltage is first set for electron extraction. Once the electrons have left the accelerating region, the voltage is switched to positive for ion extraction. Due to the large mass ratio between ions and electrons, during electron extraction phase, ions don't deviate much from their starting positions. The MCPs front surface is set to ground, which lowers the detection efficiency but is necessary for detecting both electrons and ions. The camera has a minimum of 24 μs exposure time and is triggered earlier such that the shutter closes immediately after the arrival of the electrons. The arrival times for all charged particles are recorded as a TOF trace for mass calibration with a fast digitizer.

field. The incident particle hit triggers a cascade of electron showers in the MCPs, which in turn illuminate a phosphor screen behind the MCPs. The time-of-arrival information is recorded by a digitizer via a capacitor coupling for the time-of-flight mass spectrometry (TOFMS), and the hit positions are recorded by collecting the fluorescence from the phosphor screen with a fast CMOS camera (BASLER acA2000-340km, 360 × 360 pixel frames at 1 kHz). The image is thresholded and passed to a centroiding algorithm which identifies clusters that contain multiple connected pixels. Finally, the pixel value weighed center of each cluster is recorded for post-analysis.

The electrostatic lens consists of 3 conducting plates, Repeller, Extractor and Ground. We shall refer to them collectively as VMI plates. The voltage on the Extractor is set to a specific fraction (70% in our case) of that on the Repeller for Velocity Map Imaging (VMI), which maps the 3D momentum distribution of charged particles to their hit positions on a 2D detector[36, 37]. Let's consider a charged particle that has mass m and velocity component parallel to the detector $\vec{v_T}$. VMI renders the relationship $\sqrt{m}\,\vec{v_T} = A\,\vec{r}$, where $\vec{r}$ is the position on the detector and $A \propto \frac{\sqrt{qV}}{L}$ is a conversion factor determined by the particle's charge q, the Repeller voltage V and the TOF path length L. The choice of the Repeller voltage is mainly determined by the MCP's quantum efficiency which depends on the incoming particle's velocity and sign of charge. Generally speaking, the larger the velocity, the better the efficiency. However, it becomes sub-linear after an "optimal" voltage – the efficiency vs voltage plot flattens out. Since the energy gain from the VMI plates only depends on the particle's charge, a heavier ion has lower detection efficiency due to its lower incident velocity[38, 39]. The optimal voltage for electrons is much less than that for ions due to different scattering properties [40]. The ratio of voltages between the Repeller and Extractor depends on the exact dimensions of the VMI design. Usually we first set a desired voltage on the Repeller, and then adjust the voltage on the Extrator until we see a sharp focus of a point source (eg., zero-kinetic energy ions). When a system possesses cylindrical symmetry, its 3D distribution can be reconstructed from its 2D projection via the Abel inversion, provided that the symmetry axis is parallel to the detector. This is the case for, say, ionization with a linearly polarized laser beam, where the symmetry axis coincides with the polarization direction.

A voltage switching scheme is designed to detect both the ion and electron from a single ionization event (Fig 2.3). Because of the large mass ratio, the ion doesn't move much during the time the electron leaves the accelerating region. The voltages on the VMI plates are switched from negative to positive using two DEI Scientific Pulse Generators ($<$ 25 ns switching times), immediately after the departure of the electrons. On the detector end, the camera shutter is closed after the arrival of the electron. For reference purpose, here we give a list of steps for adjusting the trigger timing for each detector component:

1. The pulse intensity and the sample pressure are adjusted to give a reasonable amount of signal.

2. The voltage switch trigger time and the TOF digitizer trigger time/record length are adjusted to see the electron signal. Note that it's enough to see TOF signals as long as the electrons see a negative voltage, the exact voltage switch timing is not important.

3. The voltage switch trigger time is fine-tuned such that it switches right after the electron's arrival. One should see both electron and ion signals after this step.

4. The camera exposure is set to the minimum and the its trigger time is delayed until electrons appear. In our case, the minimal exposure is 24 μs and it needs to be trigger more than 24 μs before the arrival of the pulse. If this is not the case (seeing hits on the camera even with zero trigger delay), then decrease the delay on the master trigger and restart from step 1.

5. The appropriate thresholds for TOF trace is set by blocking/unblocking the laser and camera images threshold is set by using centroiding statistics.

6. The desired pulse intensity is set.

7. The sample pressure is fine-tuned such that on average $\sim$0.5 ionization event takes place per laser shot. This guaranteers most of the detected electron-ion pairs come from a single molecule. This value is interpreted from electron yield statistics, assuming detection efficiency and Poisson distribution in count. See Appx B for details..

This coincidence measurement, together with VMI, allows us to study the photoelectron spectrum associated with a particular ion species. This is particularly useful in identifying different ionization and dissociation pathways (see Ch. 3 and 4). Note that with the TOFMS, we have the mass information of all charged particles. However, due to a limited frame rate for the camera, we have access to the electron momentum only. This is a detector problem and can be solved by using a detector that has both temporal and spatial resolution, such as a delay line detector [41, 42] or Timepix camera [43, 44] (see Sec. 2.4).

A conventional two-sided coincidence VMI apparatus is usually equipped with delay line detectors and has the advantage of high temporal and spatial resolution. But it's limited to low count rate coincidence measurements due to the nature of the detector. The advantage of a single-side camera based coincidence VMI setup is two fold – (1) low cost and easy operation due to its simplicity, and (2) the ability to switch between coincidence and non-coincidence modes. The coincidence mode provides access to comprehensive kinematics of a reaction and is useful in discriminating various mechanisms and/or pathways underlying the reaction. More on this will be discussed in Chapter 3. On the other hand, non-coincidence mode allows a much higher data acquisition rate and is useful in exploring parameter space. For better illustration, we show two experiments carried out in each modes.

2.3 Examples: Coincidence vs Non-coincidence

The first example is a coincidence measurement of strong field ionization of CH_2IBr (Fig 2.4). Panel (a) is the TOFMS which contains an electron peak and all major ion peaks. The timing resolution depends on the TOF tube length and the VMI plate voltage. In this case, we can resolve all major fragments resulting from photo-dissociation but the resolution is not fine enough, for instance, to separate bromine isotopes or to identify single hydrogen removals. Panel (b) shows two photoelectron spectra, measured in coincidence with the parent ion CH_2IBr+ and a fragment ion CH_2Br+. There is a systematic way of assigning the peaks in the spectra which we will discuss in detail in Sec.3.1. For now, we just note that there are obvious differences in the two spectra, which helps us understand the ionization process and ionic dynamics. In comparison, a non-coincidence measurement will only generate one spectrum for all electrons, therefore obscuring many interesting

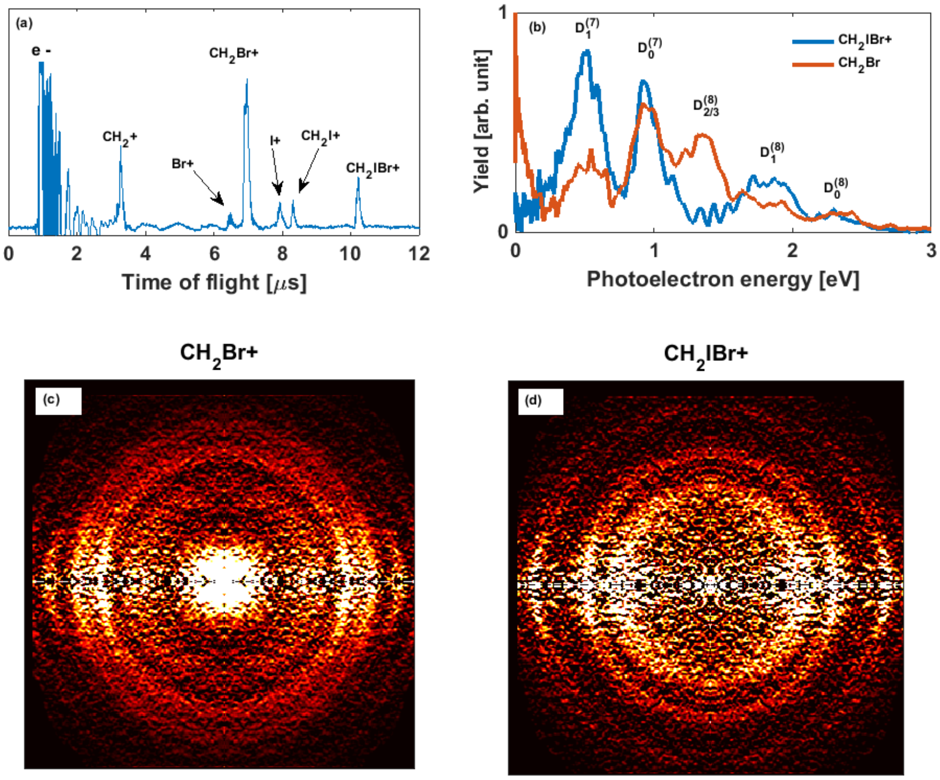

Figure 2.4: Coincidence photoelectron spectra data of CH_2IBr. (a) TOF trace showing electron and ion peaks. The electron peak is overlapping with a ringing signal from the switching voltage, but its amplitude is indeed large enough to be easily discriminated. (b) Spectra of photoelectrons measured in coincidence with the parent ion and the most abundant fragment ion, after Abel inversion and being normalized to total yield. Label $D_i^{(n)}$ indicates the electrons are resulting from a n-photon process and associated with the i-th excited ionic state. (c) and (d) 2D slices of Abel inverted images of photoelectrons measured in coincidence with CH_2Br^+ and CH_2IBr^+.

features. The bottom two panels are slices of the 3D electron distributions corresponding to the two spectra plotted in panel (b).

The second example is a non-coincidence experiment where we test the energy resolution of the detector. Ideally, we'd like to have a well defined

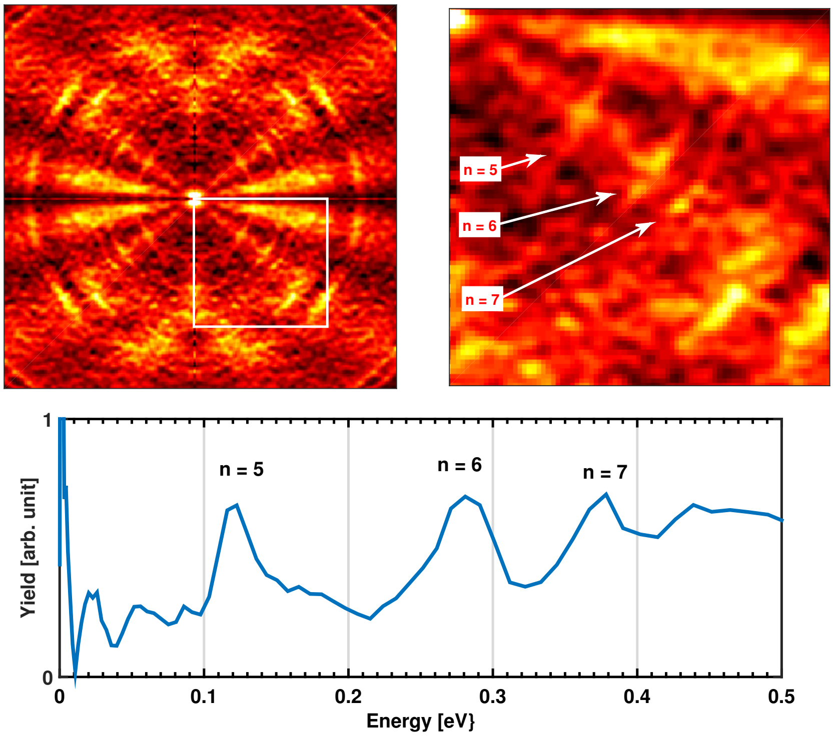

Figure 2.5: VMI images and photoelectron spectrum for strong field ionization of krypton atoms. Top panels are Abel inverted 2D images taken with the CMOS camera in non-coincidence mode, with the one on the right being zoomed onto the 4th quadrant. The lower panel is the low energy portion of the photoelectron spectrum, after background subtraction. Three peaks resulting from autoionization are labeled by their Rydberg orbitals.

(narrow and constant) energy feature for apparatus calibration. This naturally leads us to atomic systems where there are no nuclear dynamics. It's known that there are so-called doubly excited states in the strong field ionization of Krypton atoms, where one electron is in a high-lying Rydberg state while the ionic core is also excited. After the laser pulse passes, the Rydberg electron can be liberated by the energy released from the relaxation of the ion core. There is no Stark shift for this electron since the field is absent. It shows on the VMI image as a series of narrow peaks with well-defined energies that are independent of laser intensity[45] . We first calibrate (finding the conversion factor A) our apparatus with the ATI peaks, then we identify the first three Rydberg peaks in the Kr measurement shown in Fig 2.5. This gives a lower bound on the energy resolution of about 30 meV FWHM. In this setup, at 100 meV, about 30 pixels away from the center of the image, 30 meV in energy corresponds to about 5 pixels on the camera sensor, suggesting that the resolution is mostly limited by factors other than the camera, such as imperfect electrostatic fields in the VMI plates. The energy spread across a single pixel increases with energy. At about 180 pixels (2.6 eV) away from the center of the image(the camera is $360\times$ 360), one pixel corresponds to 30 meV. The upper panels in Fig 2.5 are Abel inverted images of photoelectrons, but now integrated over around the axis of symmetry (see 2.5 for different presentations of Abel inverted data). Comparing to coincidence mode, here we can no longer differentiate photoelectrons based their ion partner mass. However, while the coincidence data shown in Fig 2.4 is taken over a 12-hour experiment, the image in Fig 2.5 is a result of only a few minutes of continuous integration. This makes non-coincidence particularly useful for searching parameter space and obtain good statistics on interesting features identified in coincidence measurements.

2.4 TimepixCam Camera

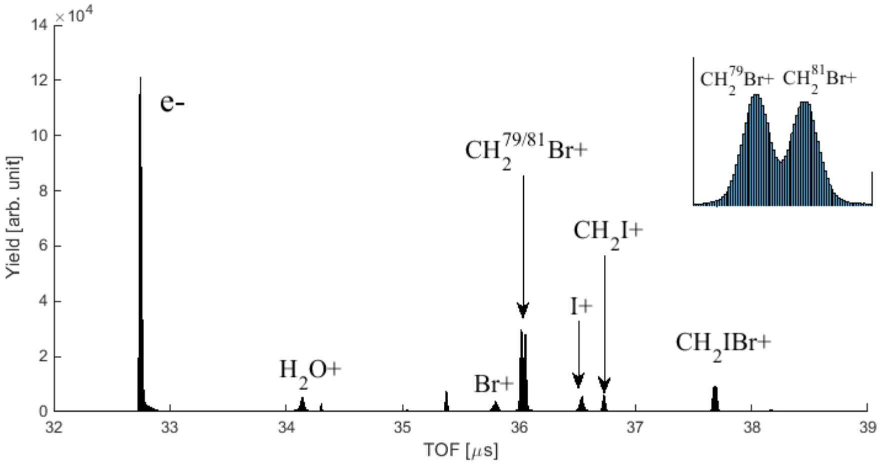

Figure 2.6: TOFMS obtained from TimepixCam camera. Note that the bromine isotopes are clearly separated in this measuremnt.

In coincidence measurements, both electrons and ions are collected by the MCPs and phosphor screen. However, the above described apparatus only measure the momentum distribution of electrons. The reason is that the camera can neither take one frame for each charged particle species due to limited frame rate, nor temporarily separate all incident hits. We set the shutter timing such that the exposure is stopped after the arrival of the electrons, so we know all hits are electrons. One way to overcome this limitation is to utilize a detector that has both spatial and temporal resolutions, such as a delay-line detector[42, 41] . However, this kind of detector design requires a low incoming flux of particle in order to temporarily resolve them. Here we present a simpler design utilizing a time-stamping camera – TimepixCam.

Compared with conventional cameras which have mostly been used as a static 2D detector, TimepixCam is designed to have the ability of recording an additional dimension – the time-of-arrival (TOA) of photons. It consists of a specialized silicon sensor[44], a Timepix3 chip[43] and a SPIDR readout system [46]. The silicon sensor has an AR-coated (anti-reflection) thin entrance window providing high quantum efficiency in 400 - 900 nm range and it's used to convert incoming light to electric current. It's connected to the Timepix3 chip via a bump bonding process which is commonly used for constructing hybrid-pixel detectors like TimepixCam. Timepix3 is developed at CERN, as the next-generation of the Timepix series [47]. It contains an array of 256×256 pixels, each of which is of (55×55 μm^2). Each pixel unit functions independently with a nominal ToA timing resolution of 1.6 ns (640 MHz), recorded in a 18-bit register. When the incoming photon flux on a pixel exceeds a pre-set threshold, its clocks the time and send it to the upstream readout borad (the SPIDR system in our case), along with the pixel's coordinates. So this camera can be used as both an imager as well as a fast digitizer. Combined with the MCP-phosphor detector, TimepixCam is capable of simultaneous detection of both the hit positions and TOA information of *all* charged particles. This is preciously what one needs for a *full* coincidence measurement – associating photoelectron spectra with photoions of particular species and momentum distribution, and *vice versa*. Since the pixels in TimepixCam operate independently and continuously, only triggered pixels send data upstream to the computer and then they reset themselves for new data acquisition. This alleviates the limited bandwidth problem in upstream data transfer that is common to high-speed cameras, and allows a long duty cycle due to continuous readout. In fact, the onboard master clock allows a 90-day continuous operation without reset. This makes it very convenient for long-duration and sparse data acquisition, such as coincidence experiments. Fig 2.6 shows a TOFMS recorded by TimepixCam, noting that the time resolution is good enough to discriminate bromine isotopes.

The TimepixCam and its implementation in the coincidence measurement is still in the test phase. We will show some preliminary results on double ionization at the end of Ch.5.

2.5 Abel Inversion

Here we describe an Abel inversion algorithm used to process all the data presented in this thesis. The Abel transform projects cylindrically symmetric 2D distribution $f(r)$ onto a 1D distribution $F(x)$, provided that the projection vector is perpendicular to the axis of symmetry. Note that the geometrical constraint implies that for a given $x = x_0$, only $f(r)$ with $r \geq x_0$ contributes to $F(x_0)$. Because of this, the transform mapping is one-to-one and the inverse transform can be used to recover the 2D distribution. Note that in the experiment, the 2D image is in fact inverted line-by-line to recover the 3D distribution.

We shall consider the discrete case of Abel transform, and by studying its geometrical constraint, derive the Abel inversion formula. In Fig 2.5, suppose we have a 2D distribution that contains 4 rings (the central disk and 3 annuli) of width 1 (same size as the Cartesian grid), which are projected along the negative y-axis onto the 7 pixels along the x-axis. The z-axis is the axis of symmetry. Cylindrical symmetry implies that we can assign a density value to each ring such the total number of particles falling in each ring is equal to the product of the ring's density and its area. And for each pixel, the contribution from one ring can be obtained by calculating the relevant patch covering that pixel. For instance, in the figure, the Abel projection of the outer most ring onto the pixel CB is twice the area of the shaded patch (and the bottom half) times the ring's density. We can also understand intuitively from the figure why the Abel inversion exist and is unique – since the outer most ring is the only contribution to the pixel BA, knowing the value of BA and the area of the ring that's projected on BA, we can recover the density of that ring. Then with this density, we can calculate the outer most ring's projection onto the pixel CB. The difference of this projection and the value of CB is the contribution from the second outer most ring, whose density can therefore be uniquely determined. Now all that's left to show is that all

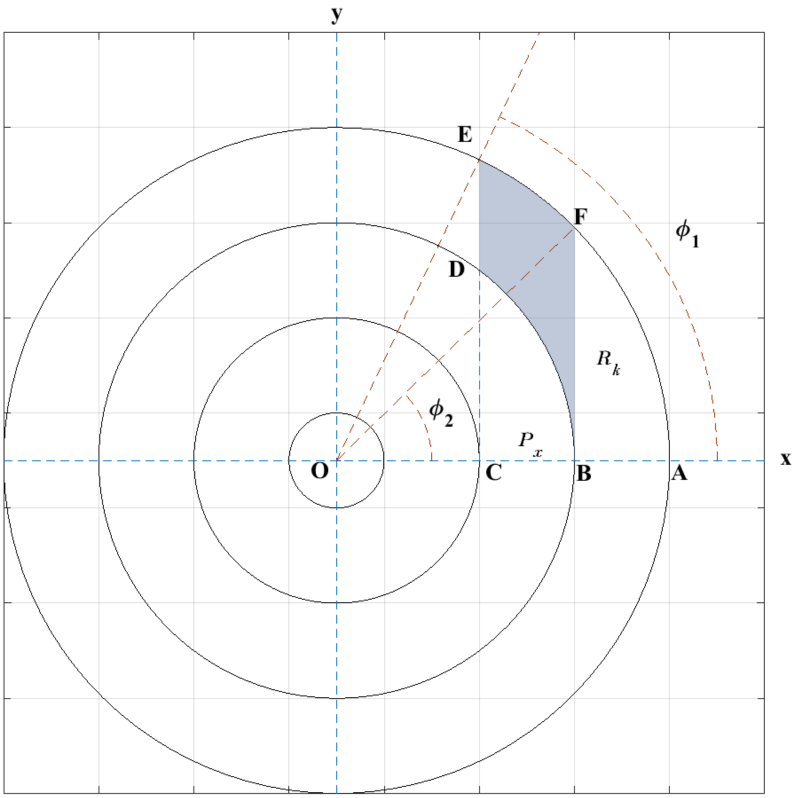

Figure 2.7: A 2D cylindrically symmetric distribution (represented by concentric rings), is projected on to pixels of a 1D detector (segments on the x-axis). Due to symmetry, each ring has a constant density value. For example, the contribution of the outer most ring to the pixel **BC** is the twice the product of the ring's density and the area **BFED**. For a given pixel of distance d away from the center, only rings with radii equal to or greater than d contribute to the projection. This implies a unique inversion to reconstruct the 2D distribution from the 1D projection. See text for details.

the patches projected onto each pixel have well defined areas. For this, let's denote by R a 4-by-1 vector such that its $k+1^{th}$ component R_k is the density value of the $k+1^{th}$ ring, counting outwards, and by P a 4-by-1 vector such that its $x+1^{th}$ component P_x is the value of the $x+1^{th}$ pixel on the x-axis. Note that $x, k = 0, 1, 2 \;\; or \;\; 3$ in this example. Let's consider the contribution on P_x from R_k, which is twice the shaded patch. The area of the shading is

$$\begin{aligned} BDEF &= OEA - OFA + OFB - OEC - CDB \qquad (2.1) \\ OEA - OFA &= \pi(k+\frac{1}{2})^2\frac{\phi_1-\phi_2}{2\pi} \\ OFB &= \frac{1}{2}(x+\frac{1}{2})\sqrt{(k+\frac{1}{2})^2-(x+\frac{1}{2})^2} \\ OEC &= \frac{1}{2}(x-\frac{1}{2})\sqrt{(k+\frac{1}{2})^2-(x-\frac{1}{2})^2} \\ \cos(\phi_1) &= \frac{x-\frac{1}{2}}{k+\frac{1}{2}} \\ \cos(\phi_2) &= \frac{x+\frac{1}{2}}{k+\frac{1}{2}} \end{aligned}$$

Eq 2.1 is indeed a recursive relation since the last term is the contribution on P_x from R_{k-1}. All the equations hold for $k \geq x$ and some special care is needed for $x = 0$. Denote the area of the shading by $\frac{1}{2}A_{xk}$, we see that $P_x = \sum_{k\geq x} A_{xk}R_k$, or in matrix form $P = AR$, more explicitly,

$$\begin{bmatrix} P_0 \\ P_1 \\ P_2 \\ P_3 \end{bmatrix} = 2\begin{bmatrix} \dots & \dots & \dots & \dots \\ 0 & \dots & \dots & \dots \\ 0 & 0 & BCD & BDEF \\ 0 & 0 & 0 & ABF \end{bmatrix}\begin{bmatrix} R_0 \\ R_1 \\ R_2 \\ R_3 \end{bmatrix} \qquad (2.2)$$

Note that A_{xk} is an upper triangular matrix, therefore A is invertible and the Abel inversion can be written as

$$R = A^{-1}P \qquad (2.3)$$

In our experiment, P is a line of pixels from the camera image and R contains all the information about the 3D momentum distribution. It's worth noting that Eq 2.3 is a linear equation with a constant linear transformation A^{-1}. This means that we only need to calculate A and its inverse once to process as much data as needed. In addition, this allows on the fly data processing since P is additive. An implementation of this algorithm is presented in Appendix C. Of course, Eq 2.3 assumes cylindrical symmetry and therefore requires a large data set. Based on our experience, 100k hits usually allows for a reasonable Abel inversion. There are other methods which are designed to deal with low statistics problem by fitting the data with multipixel basis sets [48, 49].

For historical reasons, in Fig 2.7, we have assumed the image centers on a pixel (the central circle inscribing a lattice unit). One can also derive a similar upper triangular A matrix when the center of the image is on a pixel intersection, which has the following advantage. Since a hit cluster contains multiple pixels, the centroiding algorithm renders a hit position with subpixel resolution. This makes it possible to refine the pixel array for better resolution. The simplest refinement involves sub-dividing a pixel which adds intersections to the interior of a pixel. Therefore an intersection-centered A matrix can easily adjust to this refinement.

Fig 2.8 shows the photoelectron data from the krypton experiment mentioned in the previous section. The 2D image in panel (a) is the raw camera image. The 3D distribution is obtained by applying the Abel inversion formula derived above. There are several ways to view this distribution. One can simply look at a cross section through the axis of symmetry (z-axis), as shown in panel (b), or integrate over the azimuthal angle around the z-axis to obtain panel (c). which shows the yield as a function of polar angle and radial momentum. Integrating once more around the center of the image gives the total yield as a function of transverse momentum. After converting pixels into energy, with the conversion factor given by VMI, we end up with the photoelectron spectrum, as shown in panel (d). Note that panel (c) preserves all angular dependence of the yield. Instead of integrating over all angles, one can select a certain direction. In fact, all spectra in this thesis are assumed to be produced by integrating over a ± 30 °sector about the polarization axis unless otherwise specified. This choice is based on the fact that most yields lie within this sector. And because of possible angular distributions, excluding other sectors makes the features in the spectrum more visible.

In the following chapters, we will show several experiments carried out using the VMI detection, in both coincidence and non-coincidence modes, and discuss new physical findings from them.

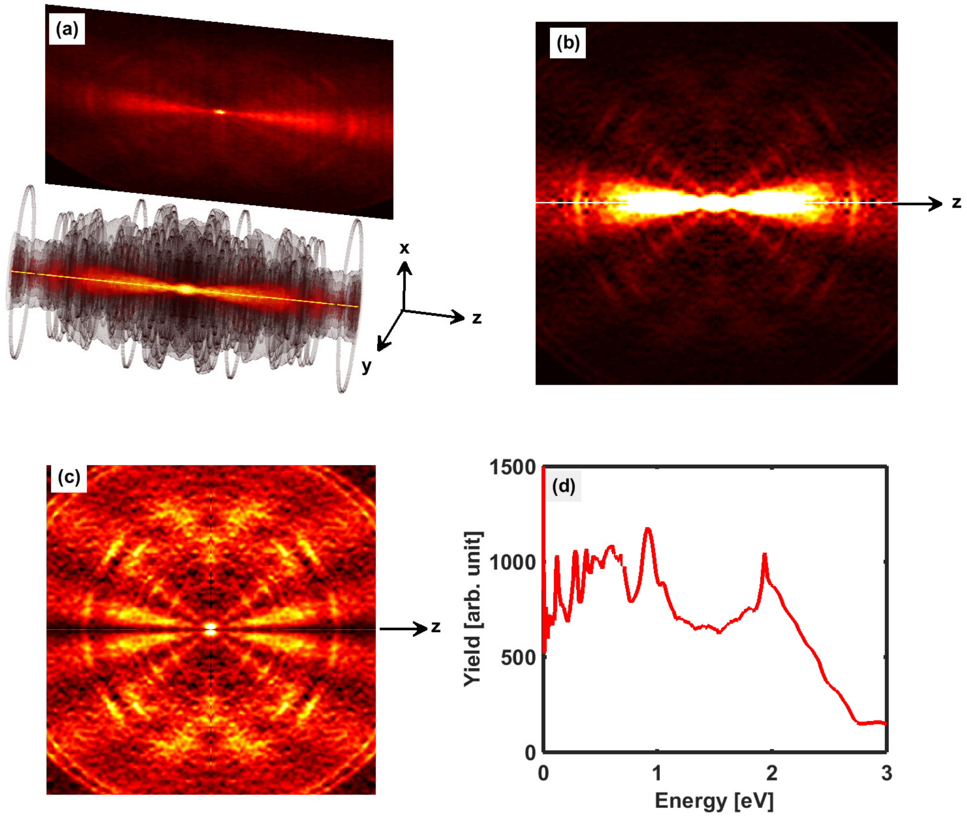

Figure 2.8: Going from 3D distribution to 1D spectrum. Panel (a) shows the reconstructed 3D momentum distribution of photoelectrons with its projection on a 2D surface. The 2D projection is what we measured with the camera in the experiment. We denote the axis of symmetry as the z-axis, which is the bright central axis of the 3D distribution. In this experiment, it's also the direction of the laser polarization. Panel (b) is a cross section of the 3D distribution, cutting through the z-axis. Panel (c) is obtained by angularly integrating over the azimuthal angle, around the z-axis. This shows the distribution of the photoelectrons as a function of polar angle and radial momentum. Panel (d) is obtained via further integration over the polar angle, around the center of the images in panel (c).

Chapter 3

Molecular SFI with Coincidence VMI Detection

As mentioned in Chapter 1, SFI is a non-linear multi-photon process that is very sensitive to the intensity of the field. Consequently, it first occurs at or near the peak of the pulse, and is naturally an ultrafast process. This allows us to use SFI as a tool to study ultrafast processes in molecular dynamics. Several recent experiments (in addition to one earlier work [50]) have provided evidence of SFI from multiple orbitals [51, 52, 53, 54, 55, 56, 57, 58, 59]. A detailed study of which orbitals are involved and what final ionic states are populated by SFI is important for understanding electronic dynamics underlying SFI. In this chapter , we discuss in detail the SFI photoelectron spectrum obtained in coincidence VMI measurement, specifically, the assignment of the peaks in the spectrum to various ionic states (Sec. 3.1) and the concept of indirect ionization (Sec. 3.2)[35, 60]. In a coincidence experiment, since electrons and ions are measured in pairs, we can discriminate the electrons based on their partner ions' masses and obtain one photoelectron spectrum in coincidence with each ion species. Often, with the knowledge of ionic potential energy surfaces and the dissociation energies for various fragmentation pathways, one can associate an ionic state with a specific ion species, and ultimately with a specific peak in the photoelectron spectrum using energy conservation. This can provide new insights into the ionization process. For instance, if an ion species is produced solely via the dissociation of a particular excited ionic state, then we know the detection of electrons in coincidence with this ion species necessarily results from the population of this excited ionic state. While assigning peaks in electron spectra, we find that some of the peaks in the photoelectron spectrum measured in coincidence with the parent ion also appear in the spectrum measured in coincidence with certain fragment ions. This suggests an ionization pathway in which the molecule is first ionized to a non-dissociative state, then field-excited to a higher dissociative state during the remainder of the pulse. We call this *indirect ionization* and shall discuss this in detail in Sec. 3.2 . In the next chapter, we will study the mechanisms underlying indirect ionization. Most experiments are carried out with halomethanes molecules which are derivatives of methane (CH_4) with one or more hydrogen atoms replaced by halogen atoms (F,Cl,Br and I). The closely spaced ionic states in this family of molecules provide a good system for studying the dynamics in the ion after SFI. In addition, the lab has a great deal of expertise in these molecules, both experimental data and electronic structure calculations, particularly, CH_2IBr [1, 2, 35]. Other small organic molecules are also uses for exploring the dependence on molecular parameters.

3.1 Coincidence Photoelectron Spectra

In this section, we use an example to illustrate coincidence VMI experiments and the procedure of assigning peaks in the photoelectron spectra. The experiment is carried out with the apparatus described in Sec 2.2 and Fig 2.3, and 30 fs amplifier pulses (no filament). We first mass-calibrate a TOF trace (similar to Fig 2.6) and mark time windows for electrons and all relevant ions (excluding background signals such as H_2O). Then we set the timings, pulse intensity and pressure according to the steps given in Sec. 2.2. For each laser shot, one TOF trace and one image are recorded by a Labview program, which processes them in the following fashion: it first checks the trace to see if there is an electron peak (without counting the number of electrons) and an ion peak in one and only one of those pre-defined ion windows (being outside implies it's either noise or coming from the background). If this is the case, then it proceeds to centroid the image; otherwise, it dumps everything and waits for the next laser shot. The centroiding algorithm thresholds the image and identifies connected pixel clusters as an incident electron hit. If there is one and only one hit, the code records the ion bin number and the electron hit coordinate; otherwise, it does nothing. This is effectively analyzes the data on the fly and drastically reduces the data file size. For post-analysis, we first construct a 2D image from the electron coordinates, for each ion species. Then we Abel invert the images and integrate twice (see Sec 2.5) to obtain the spectra – electron yield as a function of its kinetic energy. As discussed in Ch 1, energy conservation dictates the photoelectron kinetic energy:

$$KE = n\hbar\omega - I_p^i - U_p - E_S^i \qquad \text{from Equation} \quad 1.2$$

where KE is the kinetic energy of the electron, n is the number of photons absorbed, ω is the central frequency of the laser pulse, I_P^i is the ionization potential to the i^{th} continuum, U_P is the ponderomotive shift and E_S^i is the AC Stark shift of the i^{th} excited ionic state. This provides a basis for identifying various peaks in the spectra. The photon energy is about 1.6 eV for the central wavelength of 780 nm. The ionization potentials are taken from [61]. The equilibrium geometry in D_0, the excitation energies at the Franck-Condon position and dissociation channels (Fig.3.1) are from *ab initio* electronic structure calculations[1, 2]. The ponderomotive potential $U_p = \frac{e^2 E_0^2}{4m\omega^2}$ scales linearly with field intensity and therefore can be interpolated from the intensity dependent shift of non-resonant photoelectron peaks. By measuring this shift with varying intensity, one can indeed obtain an intensity calibration. In the data shown below, the pulse peak intensity is calibrated to be around 10 TW/cm^2. We expect a spread of U_p due to volume averaging effects, that is, at high intensity, not all ionization takes place at the peak of the pulse. The dynamic Stark shifts of the ionic states at the intensity used in the experiment are estimated to be small ($\sim$ 100 meV) and therefore neglected in assigning peaks. The simulation model used for making this estimation is discussed in Appendix C.

Fig 3.2 shows the photoelectron spectra in coincidence with the parent and the most abundant fragment ion from the SFI of CH_2IBr. Peak label $D_x^{(n)}$ denotes the ionization to the x^{th} ionic state by absorbing n photons. From Fig. 3.1 we see that D_4 has a much larger IP than the first 4 states and therefore we shall neglect it in the peak assignment. This simplification is backed by the observation that there are few I+ and CH_2I+ ions in the TOF trace, which are associated with the dissociation from D_4[61]. We first calculate the energy differences among peaks and compare these values to those from the calculation to form assignment hypotheses. Then we note that D_0 and D_1 are the only non-dissociative states and therefore electrons in coincidence with the parent ion should be associated with these 2 states. These two observations fix the assignment of D_0 and D_1, which are the only

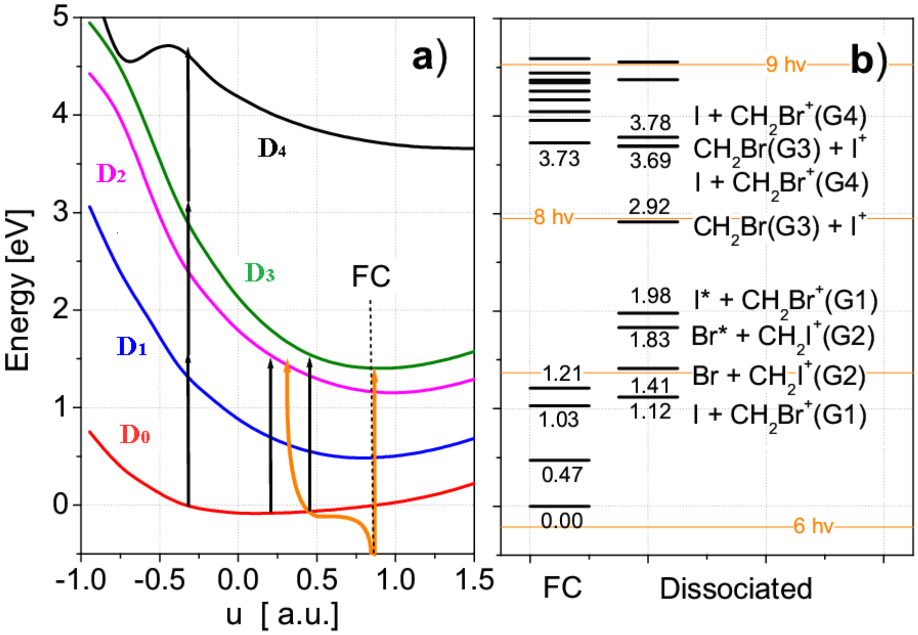

Figure 3.1: Potential energy curves as a function of nuclear coordinate for CH_2IBr cation (Left) and dissociation channels (Right) [1, 2].

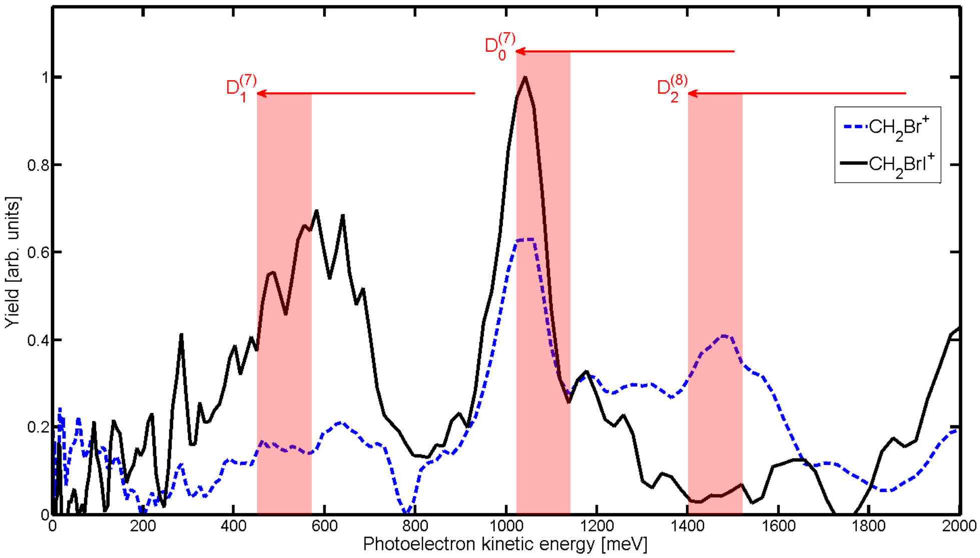

Figure 3.2: Photoelectron spectra coincident with the parent ion (black solid) and one fragment ion (dash blue)from strong field single ionization of CH_2IBr. Peak label $D_x^{(n)}$ denotes the ionization to the x^{th} ionic state by absorbing n photons. We see two peaks $D_1^{(7)}$ and $D_0^{(7)}$ in the photoelectron spectrum measured in coincidence with CH_2IBr+, while there is an extra peak $D_2^{(8)}$ associated with CH_2Br+. The tails of red arrows (the right ends) indicate the appearance energy calculated based on peak assignment (see main text) and Eq. 3.1, with $U_p = 0$. The heads (the left ends) indicate the appearance energy with U_p = maximum (at the peak of the pulse). The shaded regions are where the U_p lies within 70% of its maximum, which is where we expect most ionization to take place[35].

major peaks in the spectrum coincident with the parent ion. Those peaks *not* in coincidence with the parent ion and not having the same energies as D_0 or D_1 must be associated with D_2 or D_3. What's left now are the peaks in coincidence with the fragment ion while having the same energy as D_0 or D_1. Energy conservation dictates that these electrons must result from ionizations to D_0 and D_1. The fact that they are measured in coincidence with the fragment ion suggests that the ion is further excited to D_2 or D_3 after the initial ionization. In fact, as suggested by Fig.3.1, there is a 1-photon resonance from D_0 to $D_{2/3}$ not far away from the Franck-Condon (FC) point (the position where ionization takes place). Even though the estimated time for a wavepacket on D_0 to evolve from the FC to the resonance is about 80 fs[62], the strong coupling can still excite a fair amount of population (also see Sec.4.3 for more discussion on off-resonant transitions). With the estimate value for the pulse intensity, we can calculate U_p and the absolute energies we expect from Eq. 3.1. This confirms our assignment and give the photon order n for each peak, as labeled in the Fig 3.2.

This peak assignment procedure is generally applicable for molecules we've studied. In some cases, there are many closely spaced peaks due to either high intensity (so one can no longer ignore high-lying ionic states) or neutral resonances (each neutral resonance can result in a separate peak with energy close to that of the non-resonant peak), which makes the assignment difficult. One way to circumvent this problem is to start from lower intensity and assign lower states first. Then we can go to non-coincidence mode and increase intensity while following assigned peaks and note newly appearing peaks. Once reaching the target intensity, we can again use coincidence measurements to resolving the new peaks. If possible, one can also tune the laser central wavelength to map out resonances.

3.2 Direct vs Indirect Ionization

When talking about the ionization of atoms or molecules, it's intuitive to think of the removal of an electron from the highest occupied molecular orbital (HOMO) since it requires the least amount of energy. However, in molecular SFI, as we see in Fig. 3.2 (D_2 peak), it's possible to directly liberate an inner orbital electron with intense pulses (~ 10 TW/cm^2) and produce an excited ion (panel b in Fig. 3.3).

On the other hand, in Fig 3.1 we see that the parent ions are associated

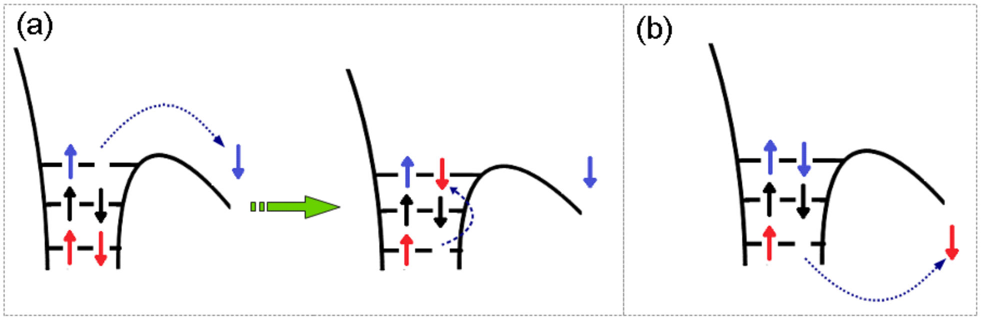

Figure 3.3: (a) *Indirect ionization*: initial ionization liberates an electron from the HOMO, and then the field excites the ion by promoting an inner orbital electron. (b) *Direct ionization*: direct removal of an electron, in this case, an inner orbital electron.

with either D_0 or D_1, and fragment ions result from the dissociation from D_2 or higher states. However, we note that electrons of certain energy that are detected in coincidence with both the parent and fragment ions. The fact that an electron is detected in coincidence with the parent ion implies that the molecule is ionized to either D_0 or D_1. The only way for this electron to be detected in coincidence with a fragment ion is that the ion in state D_0 or D_1 is further excited to a dissociative state by the field after the initial ionization, as illustrated in panel a in Fig. 3.3. The net result is the detection of a fragment ion in coincidence with an electron whose energy is consistent with ionization to a non-dissociative state. We shall refer to this kind of ionization *indirect ionization* (also know as *post-ionization excitation*). Fig. 3.3 compares these two different ways of creating excited ionic states. Note that as far as the final ionic state is concerned, there is no difference between these two pathways. However, the liberated electrons generally differ in their kinetic energies, and possibly angular distributions. In other words, by measuring the electron's kinetic energy, we can learn about the actual ionization process and the state of the ion at the moment of ionization. Since the occurrence and the kinetic energy release of a dissociation is determined by the final state of the ion at the end of the pulse, by measuring the ion mass and/or momentum in coincidence with its partner electron, we can study what happens between the time of the initial ionization and the end of the pulse, for instance, how did the post-ionization excitation take place.

Fig 3.4 shows photoelectron spectra from the coincidence measurement

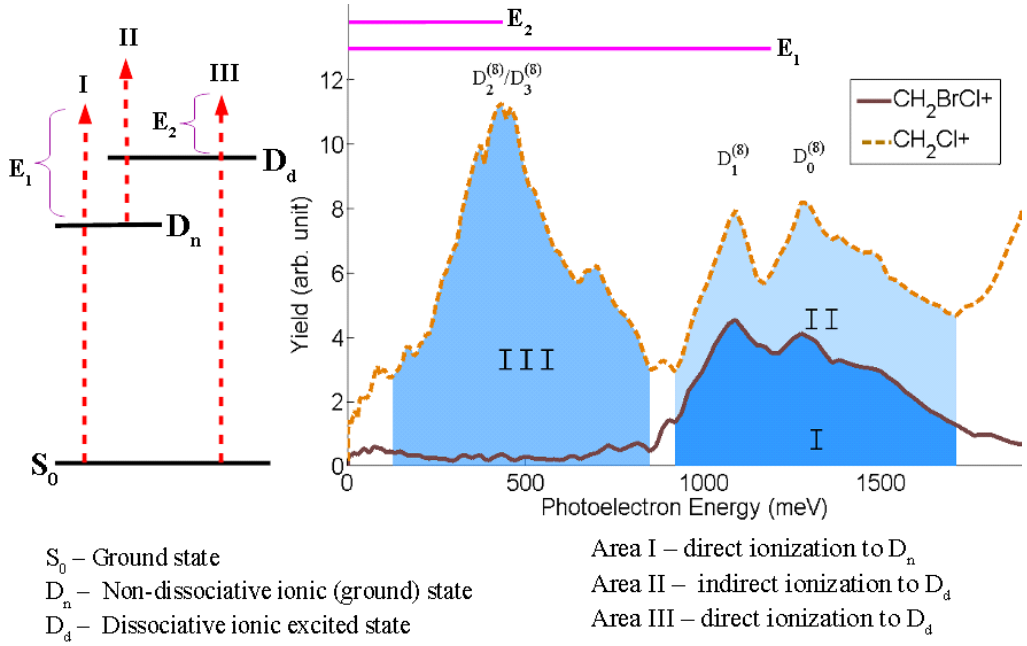

Figure 3.4: Comparing direct and indirect ionizations. The photoelectron spectra are from a coincidence measurement of the ionization of CH_2BrCl. 3 ionization pathways are identified and associated with features in the photoelectron spectra. D_n and D_d denote non-dissociative and dissociative ionic states, respectively and collectively. Note that the sum of area I and II is the total *initial* ionization to D_n, the former remaining in that state while the latter being further excited to other states. Consequently, photoelectrons coming from path I and II have the same kinetic energy, E_1. Those from ionization path III have less energy, E_2, since the ions end up in more highly excited states.

of SFI of CH_2BrCl together with a schematic comparison of 3 different ionization pathways. Pathway I and III are direct ionization, going to non-dissociative states D_n (D_0 and D_1 in this case) and dissociative states D_d (D_2 and D_3 in this case) states, respectively. Pathway II is indirect ionization, corresponding to the population that is initially ionized to D_n and then excited to D_d. The sum of I and II is the total ionization *initially* to D_n. Now one may ask: what effects the ratio between direct and indirect ionization? And what effects the ratio between ionization to D_n and D_d? In the next section, we try to answer these questions by comparing various molecular systems.

3.3 A Survey of Ionization Pathways

In order to explore the physical quantities that affect various ionization pathways, we carry out VMI coincidence measurements on 8 different molecules: Carbon disulfide(CS_2), 1,3-Cyclohexadiene(C_6H_8), $\alpha-$terpinene($C_{10}H_{16}$), 1,3-butadiene(C_4H_6), Iodobenzene(C_6H_5I), Trifluoroiodomethane(CF_3I), Bromochloromethane(CH_2BrCl) and Iodobromomethane(CH_2IBr), which represent a range of sizes, structures and energy gaps between D_n and D_d. The gap energy ranges from below 1 eV to above 4 eV. Note that the photon energy used in these experiments is about 1.6 eV. Table 3.1 lists the IPs and gap energies for all the molecules used in this study. Wherever possible we have used experimental values. Since we are interested in the gap between non-dissociative states (D_n) and dissociative states (D_d), we treat different D_n-D_d pairs within each molecule separately as long as we can discern them in the measured spectrum.

We obtain the absolute yields for different states by integrating over portions of the spectra in the same fashion as illustrated in Fig. 3.3 (shaded areas) and then compute the ratios between various pathways, which are shown in table 3.2. The total parent ion yield refers to all the ionization initially going to D_n, which is the sum of I and II in Fig. 3.3. We consider 3 different ratios here: R_F, the percentage of the total ionization yield that ends up in D_d, either directly or indirectly. R_{IF-P}, the percentage of the D_n that is excited to D_d. R_{DF-P}, the percentage of the initial ionization that ends up in D_d. We will discuss these ratios separately in the remainder of this section.

Since we are comparing results for different molecules, we try to maintain a constant ionization rate for all experiments by adjusting the laser pulse intensity and molecule sample pressure. We also worked to achieve a total ionization yield of about 0.6 per laser shot in order to obtain a good true coincidence rate (i.e., $\lambda = 0.6$ in the notation used in Appendix B, λ being the mean of the Poisson distribution.). The systematic uncertainty in this experiment is mainly due to the intensity variation. We estimate that the ionization rate varies between molecules within a factor of two above and below the mean value. Given the strong intensity dependence of the ionization process, we estimate that this corresponds to a 10 percent variation in the

Species	D_0(eV)	D_1(eV)	D_2(eV)	D_3(eV)	Gap Energy (eV)
CH_2IBr [63]	9.69	10.26	10.91(d)	11.12(d)	11.02-10.26=0.76 [b]
CH_2BrCl [63]	10.77	11.03	11.72(d)	11.81(d)	11.76-10.90=0.86 [a]
C_6H_5I [64]	8.75	9.45	9.74	10.55(d)	10.55-9.60=0.95 [a]
CH_2IBr [63]	9.69	10.26	10.91(d)	11.12(d)	11.02-9.69=1.33 [b]
C_6H_5I [64]	8.75	9.45	9.74	10.55(d)	10.55-8.75=1.80
CF_3I [65, 66, 67]	10.37	11.09	13.02(d)	15.17(d)	13.02-11.09=1.93
C_4H_6 [68]	9.09	11.50(d)	12.44(d)	n/a	11.50-9.09=2.41
CF_3I [65, 66, 67]	10.37	11.09	13.02(d)	15.17(d)	13.02-10.37=2.65
$C_{10}H_{16}$ [69]	7.57	10.25(d)	10.71(d)	n/a	10.48-7.57=2.91 [b]
C_6H_8 [70]	8.25	11.67(d)	13.19(d)	13.26(d)	11.67-8.25=3.42
CS_2 [71]	10.08	12.70	14.47(d)	16.19(d)	14.47-10.08=4.39

Table 3.1: Ionization potentials and gap energies for all the molecules used in the experiments, sorted by the increasing gap energy, which is defined as the energy difference between a dissociative ionic states and a non-dissociative one. "(d)" labels dissociative states. Notice that since CH_2IBr, C_6H_5I and CF_3I all have two reasonably resolved peaks in their photoelectron spectra in coincidence with the parent ions (see Figure A.1, A.2 and A.3 in Appendix A), all of them are listed twice in the table.
In case two states lie too close to each other to be resolved in the photoelectron spectra, we treat them as one state with their average IP:
[a] averaged non-dissociative states' energy;
[b] averaged dissociative states' energy.

intensity. We carry out an intensity study on a chosen molecule: CH_2BrCl. We use the differences between the spectra taken at different intensities to estimate error bars for the graphs shown below. In order to check that the uncertainties we estimate based on CH_2BrCl are reasonable, we measured the photoelectron spectrum in non-coincidence mode as a function of intensity for all the other samples, and find that for the small variations in intensity in our experiments there is only variation in the total yield and no obvious change in the shape of the spectra. Thus, we believe the relative uncertainty obtained from CH_2BrCl provides a reasonable estimate of the uncertainty for the other samples. The error bars in Figure 3.6 and 3.7 are obtained in this fashion. The coincidence photoelectron spectra for all the molecules other than CH_2BrCl are shown in Appendix A.

Ratio	Definition	Plot	Source
R_F	total fragment ion yield vs. total ionization yield	Figure 3.5	fragment-to-all
R_{IF-P}	fragment yield via excitation vs. total parent ion yield	Figure 3.6	II-to-(I+II)
R_{DF-P}	direct fragment yield vs. total parent ion yield	Figure 3.7	III-to-(I+II)

Table 3.2: Definition of ratios and corresponding figures. The last column indicates how these ratios are obtained from the spectra illustrated in Figure 3.4. The first ratio R_F is directly calculated from the total number of photoelectrons measured in coincidence with parent and fragment ions.

Since the efficiency of the MCPs varies with mass for a given energy [39, 38], we have corrected our measured photoelectron spectra with the detection efficiencies extrapolated from Fig. 3 in [39]. The details of the correction algorithm are given in Appendix B.

3.3.1 Fraction of Fragment Ions

Now we examine the ratios listed in Table 3.2. The first ratio R_F plotted in Figure 3.5 shows the fraction of the ionization that is dissociative, i.e., the fraction of the photoelectrons in coincidence with the fragment ions. Since CH_2IBr, C_6H_5I and CF_3I all have two energy gaps listed in Table 4.1, in this plot we use their average values: 1.10 eV for CH_2IBr, 1.37 eV for C_6H_5I and 2.29 eV for CF_3I. The measurement shows a trend of decreasing ionization to excited states with increasing gap size. We note that the photon energy (1.6 eV) roughly divides the molecules into ones which have a significant dissociative ionization yield and ones which don't. There are two possible explanations for this behavior: (1) When the gap energy is closer to the photon energy, it's more likely to populate D_d via a 1-photon resonance from D_n, that is, via indirect ionization. This is examined in Fig. 3.6 and the text following it. (2) When the gap energy is larger than the photon energy, direct ionization requires an extra photon. This is examined in Fig. 3.7 and the text following it.

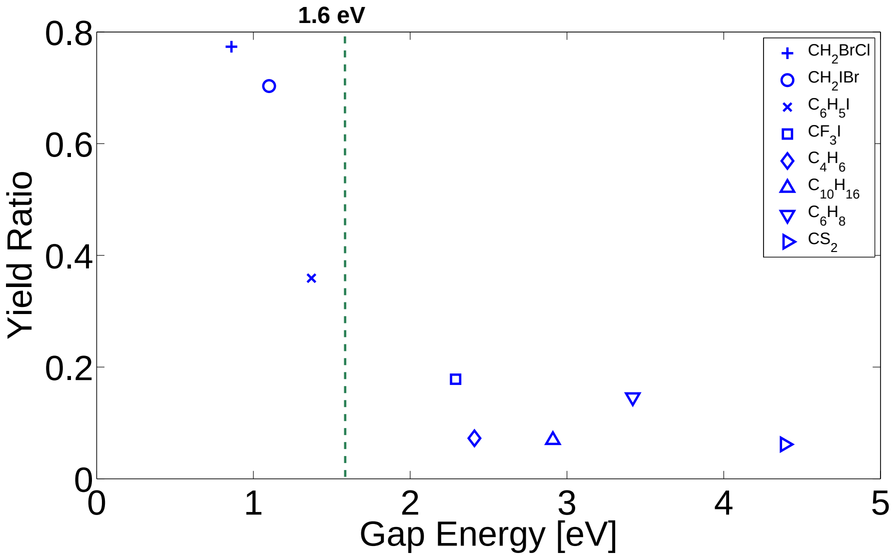

Figure 3.5: R_F, total fragment ion yield divided by the total ionization yield. The ratios are calculated directly from the numbers of photoelectrons collected in coincidence with the parent and fragment ions, hence no error bars shown. Here the fragment production includes both direct and indirect pathways.

3.3.2 Indirect Fragment vs Parent

R_{IF-P}, plotted in Figure 3.6 shows the fraction of ionization to non-dissociative states followed by further excitation in the laser field to dissociative states, as a function of the gap energy. While there is clearly a trend of decreasing indirect ionization with gap energy, there is also a non-trivial spread. Earlier work has noted the importance of ionic resonances in determining whether dissociation occurs in SFI [72, 73, 74, 75]. While the energy separations and transition dipole moments between ionic states at the Franck Condon (FC) point for vertical ionization are important, vibrational dynamics during the ionization process can also lead to dynamic resonances and transitions between ionic states away from the FC point [76].

In order to illustrate how the various factors (resonance conditions, vibrational dynamics and transition dipole moments) can influence the extent of indirect ionization, we compare two of the molecular samples more detail. For CH_2IBr, we measure substantial indirect ionization from D_0 despite the fact

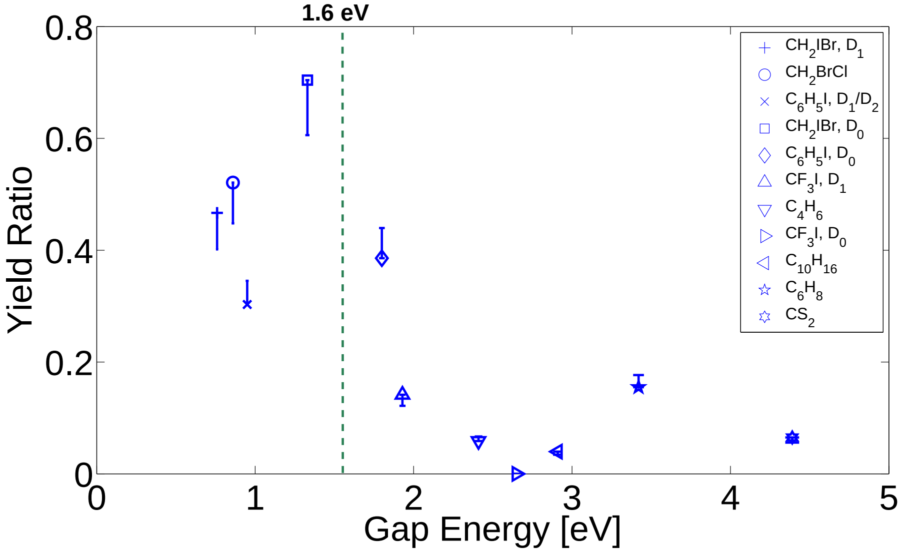

Figure 3.6: $R_{\mathrm{IF-P}}$, fragment production from excitation of parent ion divided by total parent ion production. This shows the fraction of the initially produced parent ions that are further excited to dissociative states. The ratios are calculated by integrating relevant regions in the photoelectron spectrum measured in coincidence with the parent and fragment ions. The choice of these regions is illustrated in Fig, 3.3, in this case, the ratio between Area II and (Area I + Area II).

that there is no resonance at the FC point. However, there is evidence that motion along the D_0 potential energy surface can lead to a resonance between D_0 and D_2/D_3 during the laser pulse [62]. Since the transition dipole moments between these states is large, population can be efficiently transferred to D_2/D_3 during the tail of the ionization pulse, leading to the large indirect ionization yield observed. In contrast, we observe little indirect ionization to D_2 (the first dissociative state) from D_0 in CF_3I (see the data point at around 2.6 eV as well as Figure A.3). We believe this is due to small transition dipole moments between these states (calculated at the same level of theory as in earlier work [2, 63]) and the fact that the states are separated by an energy much larger than the photon energy, even if one considers vibrational motion along D_0. In Ch.4, we will come back to these two molecules and present a more quantitative study on the underlying mechanism of indirect ionization.

3.3.3 Direct fragment vs parent

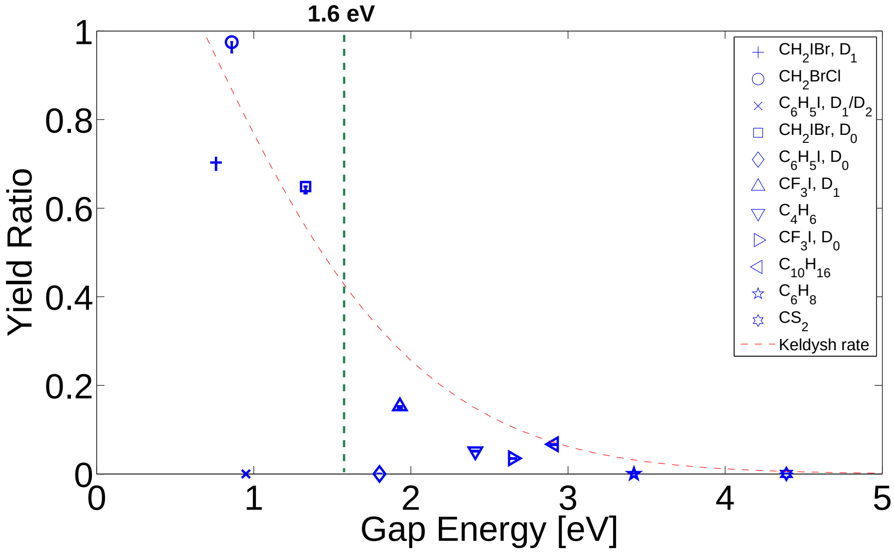

Figure 3.7: R_{DF-P}, direct fragment production divided by total parent ion production. The latter includes all the population reaching non-dissociative states, whether staying there in the end or excited further to dissociative states. This figure compares the likelihoods of ionising a high-lying and a low-lying orbital electron. The ratios are calculated by integrating relevant regions in the photoelectron spectra measured in coincidence with the parent and fragment ions. The choice of these regions is illustrated in Figure 3.4, in this case, the ratio between Area III and (Area I + Area II).

R_{DF-P} plotted in Figure 3.7 compares two competing ionization processes from the neutral: direct removal of an electron from a high-lying vs more deeply bound orbital. The ratio shows a strong dependence on the gap energy, especially near the photon energy of 1.6 eV, where an abrupt jump can been seen. One framework for interpreting the measurements is provided by the strong field approximation (SFA), where the ionization rate is proportional to the product of the Dyson norm and the Keldysh rate, $G_{lm}K(\mathrm{IP}_{lm}, E_0)$, where IP_{lm} is the ionization potential and E_0 is the amplitude of the electric field. The Dyson norm $G_{lm} =< \phi_{lm} \,|\, \phi_{lm} >$ is simply the norm of the Dyson orbital, which is a one-electron wavefunction defined as the overlap between the neutral state $|N_m\rangle$ and ionic states $|I_l\rangle$,

$|\phi_{lm}\rangle = \sqrt{n} < I_l \,|\, N_m >$, n being the number of electrons. The Keldysh rate results from the calculation of tunnel ionization and is approximately proportional to an exponential term $e^{-\text{IP}}$. Considering low-lying ionic states here, one expects the Dyson norms to be all close to unity, since the low lying ionic states are dominated by single hole configurations, corresponding to removing an electron from a single orbital. Considering now the dependence on the IP, we focus on two ionic states: a non-dissociative state a with IP E_a and a dissociative state b with IP E_b. The ionization rates to these two states are proportional to e^{-E_a} and e^{-E_b} and it follows that the ratio of their yields is simply given by $e^{-(E_b-E_a)}$. But $E_b - E_a$ is nothing but the gap energy. The ratio is plotted as a red dashed curve in Figure 3.7, with appropriate multiplicative factors obtained from fitting the data. We note that while this curve captures the general decreasing trend of the data, the experimental ratios are consistently lower than expected above the photon energy. Furthermore, a few of the molecular species, notably iodobenzene (C_6H_5I) deviate significantly from the curve. In addition, C_6H_5I, C_6H_8 and CS_2 show no significant direct ionization to excited dissociative states. This suggests that the SFA prediction is less reliable when the photon order varies, consistent with earlier measurements and calculations [57], where the authors find SFA performs better in one-photon XUV ionization than SFI.

Through a systematic study of several molecular systems, we've seen that the photon energy (1.6 eV) appears to be an important threshold in determining the amount of ionization to excited states. In the next chapter, we will continue exploring the effect of gap energy in excited states ionization, but with a focus on the indirect ionization pathway.

Chapter 4

Ionic Dynamics Underlying Indirect Ionization

In the last chapter, we introduced coincidence VMI measurement and discussed two ionization pathways – *direct* and *indirect* ionization. A natural question one can ask is how exactly an *indirect* ionization takes place and what physical parameters it depends on. In this chapter, we will try to answer this question by proposing two possible mechanisms underlying indirect ionization. As the alternative name, post-ionization excitation, suggests, both mechanisms are concerned with what happens to the ion after the initial ionization. The first mechanism, *resonant transition facilitated by nuclear dynamics*, studies the effect of nuclear motion induced resonances. The second mechanism, *non-adiabatic transition induced by the laser field*, explores the non-adiabaticity of the field-molecule interaction. Note here by non-adiabaticity, we specifically refer to the non-adiabaticity induced by the fast varying external field, in contrast to the nuclear dynamics induced non-Born-Oppenheimer effects. We carry out SFI experiments and theoretical simulations on two molecular systems to compare these mechanisms. Both experimental data and simulation results confirm the importance of the *resonant transition* and provide insight into the *non-adiabatic transition*.

4.1 Resonant Transition vs Non-adiabatic Transition

In this section, we describe two mechanisms in detail and compare their similarities and differences. Fig. 4.1 shows a cartoon illustration of these two mechanisms. In the case of resonant transition facilitated by nuclear dynamics, shown in panel (a), the molecule is first ionized from the ground neutral state S_0 to the ground ionic state D_0 at the Franck-Condon (FC) point, then as the wave packet evolves along the potential surface, it reaches a one-photon resonance where the ion is excited to a higher state D_N. Depending on the molecule, nuclear motion is not always necessary but usually required to reach a resonance. This sets a natural timescale of tens of fs or longer, which means we can experimentally study this effect by using pulses of different durations. In fact, we can use a sub-10 fs pulse to effectively "freeze" the nuclear motion and suppress the resonant behavior [77].

The second mechanism is non-adiabatic transitions induced by the laser field. In contrast to the non-adiabaticity associated with the breakdown of the Born-Oppenheimer approximation, which involves nuclear motion and depends on the molecular system, the non-adiabaticity we are interested in here is caused by the varying laser field, which has a natural time scale of the carrier period and is present in all systems. Since we expect this non-adibaticity to be important in an intense field with strong molecule-field couplings, we should work in the instantaneous eigenbasis of the Hamiltonian. More precisely, we call the eigenstates of the *bare* Hamiltonian (no external field) *diabatic* states, denoted by $\mathrm{D}_\mathrm{N}, \mathrm{N} = 0, 1, 2...$, and those of the *total* Hamiltonian (molecule + field) *adiabatic* states, denoted by $\mathrm{D}'_\mathrm{N}, \mathrm{N} = 0, 1, 2....$ Let's consider a simple case of tunnel ionization at the peak of a laser pulse, in which an electron is liberated, leaving the cation in the lowest *adiabatic* ionic state D'_0, shown in panel (b) in Figure 4.1. This state can be expressed as a linear combination of *diabatic* states, assuming only 2 states, $\mathrm{D}'_0 = a\mathrm{D}_0 + b\mathrm{D}_1,\ |a|^2 + |b|^2 = 1$. Suppose now the field turns off so rapidly that there is no time for any population transfer, then the molecule is projected onto the *diabatic* states such that we find a probability of $|a|^2$ of being in D_0, and a probability of $|b|^2$ of being in D_1. This is known as the Sudden Approximation. Generally speaking, since the field varies in time, the diagonalization of the *total* Hamiltonian is time-dependent and its eigenvectors experience a rotation in the Hilbert space. This rotation introduces

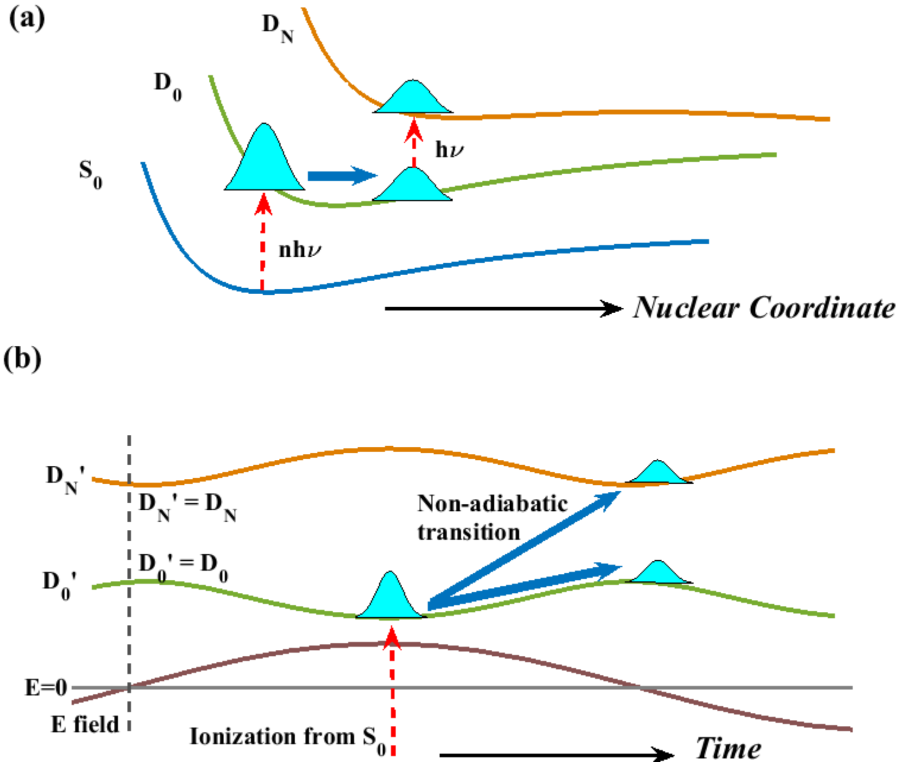

Figure 4.1: Cartoon illustrations of two possible indirect ionization mechanisms: (a) resonant transition facilitated by nuclear dynamics. After ionization, the nuclear wavepacket starts evolving along the potential surface from the Franck-Condon point towards the minimum of the potential. A transition to a high-lying ionic states can occur if a resonance condition is met. (b) Non-adiabatic transition induced by the laser field for a half cycle. After tunnel ionization near the peak of the field, the varying laser field induces a “hoppings” between two *adiabatic* states. This is most likely to happen when the laser field crosses zero when the transition rate is the largest. Note the x-axes in the two panels are different.

a coupling among *adiabatic* eigenstates because the time derivative of one eigenstate has a non-zero projection onto other eigenstates. So the coupling depends on time via the rate of change of the field. In fact, the faster the variation of the field and the smaller the energy gaps among the states, the larger the rate of non-adiabatic transitions. This non-adiabatic transition manifests itself as indirect ionization since it takes place after the initial ionization.

In order to better compare the differences between these two mechanisms, we consider an example of a 2-level system coupled to an external field via dipole couplings. First let's look at resonant transitions. The TDSE $i\hbar\frac{\mathrm{d}}{\mathrm{d}t}\Psi(t) = H(t)\Psi(t)$ can be written in the matrix form:

$$i\hbar\frac{\mathrm{d}}{\mathrm{d}t}\begin{pmatrix} a(t)e^{-i\omega_a t} \\ b(t)e^{-i\omega_b t} \end{pmatrix} = \begin{pmatrix} E_a & V(t) \\ V(t)^* & E_b \end{pmatrix}\begin{pmatrix} a(t)e^{-i\omega_a t} \\ b(t)e^{-i\omega_b t} \end{pmatrix} \tag{4.1}$$

where $E_a = \hbar\omega_a$, $E_b = \hbar\omega_b$ and $|a(t)|^2+|b(t)|^2 = 1$. We assume a real coupling $V(t) = -\mu\epsilon(t)\cos(\omega t) = V(t)^*$, where μ is the transition dipole moment, $\epsilon(t)$ is the pulse envelope and ω is the carrier frequency. A resonance implies a small detuning, $\Delta = \omega - (\omega_b - \omega_a) << \omega$. Under this condition we can apply the rotating wave approximation (RWA) to Eq. 4.1 and arrive at

$$\begin{cases} \dot{a}(t) = \frac{i\chi(t)}{2}e^{+i\Delta t}b(t) \\ \dot{b}(t) = \frac{i\chi(t)}{2}e^{-i\Delta t}a(t) \end{cases} \tag{4.2}$$

where $\chi(t) = \mu\epsilon(t)/\hbar$ is the Rabi frequency. The coupling consists of an amplitude ($\sim \chi(t)$) and a phase ($\sim \Delta t$). It's instructive to look at the pertubative behavior of Equation 4.2 when the population transfer is small, that is, assuming $a(t) \approx 1$ for all $0 \leq t \leq t_0$.

$$b(t_0) \approx \frac{i}{2}\int_0^{t=t_0} \chi(t)e^{-i\Delta t}\mathrm{d}t \tag{4.3}$$

Note that (1) a small Δ is required for coherent population transfer, which is equivalent to a resonance condition. (2) $\chi(t)$ is a positive value and varies on the time-scale of the pulse envelope. So when Δ is small, only a moderate $\chi(t)$ is needed to produce significant population transfer. (3) Equation 4.3 is a perturbative result. One can indeed solve Equation 4.2 non-perturbatively to obtain the Rabi oscillations. With an initial condition $|a(0)|^2 = 1$ and

$|b(0)|^2 = 0$, we get:

$$\begin{cases} |a(t)|^2 = (\frac{\Delta}{\Omega})^2 + (\frac{\chi}{\Omega})^2 \cos^2(\frac{\Omega t}{2}) \\ |b(t)|^2 = (\frac{\chi}{\Omega})^2 \sin^2(\frac{\Omega t}{2}) \end{cases} \tag{4.4}$$

We see that the population cycles between two states at the frequency of $\Omega/4$, where $\Omega = \sqrt{\chi^2 + \Delta^2}$. In the case of $\Delta = 0$, $\Omega = \chi$ and a pulse of duration $t = \pi/\chi$, all population is transferred from one state to the other. Such a pulse is termed a π-pulse. (4) Even though nuclear dynamics is not included in the derivation here and we have assumed constant E_a, E_b and Δ, nuclear motion is generally required to reach a resonance condition. In other words, Δ generally depends on time indirectly via nuclear dynamics.

The solutions 4.3 and 4.4 are derived in the limit of a small detuning. Now we consider the non-adiabatic transition which takes place in the limit of a large Rabi frequency, or equivalently, an intense field, assuming the transition dipole moments remain the same for the same 2-level system. We can no longer apply the RWA because there is no constraint on the detuning now. Since the field is intense and the Stark shifts are significant, we should work in the *adiabatic* basis. Let $U(t)$ be the unitary transformation that diagonalizes the instantaneous Hamiltonian $H(t)$:

$$U^{-1}(t)H(t)U(t) = D(t) \tag{4.5}$$

$$D(t) = \begin{pmatrix} E'_a & 0 \\ 0 & E'_b \end{pmatrix} \tag{4.6}$$

$$\Psi' = U^{-1}\Psi = \begin{pmatrix} a'(t)e^{-i\omega'_a t} \\ b'(t)e^{-i\omega'_b t} \end{pmatrix} \tag{4.7}$$

One can show that for a 2-level system,

$$U(t) = \begin{pmatrix} \cos(\frac{\theta}{2})e^{-i\phi/2} & -\sin(\frac{\theta}{2})e^{-i\phi/2} \\ \sin(\frac{\theta}{2})e^{+i\phi/2} & \cos(\frac{\theta}{2})e^{+i\phi/2} \end{pmatrix} \tag{4.8}$$

where

$$E'_{a/b} = \frac{1}{2}(E_a + E_b) \pm \frac{1}{2}\sqrt{(E_a - E_b)^2 + 4V^2} \tag{4.9}$$

$$\tan\theta = \frac{2|V|}{E}, \quad E = E_a - E_b \equiv \hbar\omega_0 \tag{4.10}$$

$$V = |V|e^{i\phi} \tag{4.11}$$

Since we've assumed $V = V^*$, $\phi = 0$. Substituting Eq. 4.6, 4.7 and 4.8 into the TDSE 4.1, we get

$$i\hbar\frac{\mathrm{d}}{\mathrm{d}t}\begin{pmatrix} a'(t)e^{-i\omega'_a t} \\ b'(t)e^{-i\omega'_b t} \end{pmatrix} = \begin{pmatrix} E'_a & \frac{i\hbar\dot{\theta}}{2} \\ -\frac{i\hbar\dot{\theta}}{2} & E'_b \end{pmatrix} \begin{pmatrix} a'(t)e^{-i\omega'_a t} \\ b'(t)e^{-i\omega'_b t} \end{pmatrix} \tag{4.12}$$

which simplifies to

$$\begin{cases} \dot{a}'(t) = +\frac{\dot{\theta}}{2}\, e^{+iEt/\hbar}\, b'(t) \\ \dot{b}'(t) = -\frac{\dot{\theta}}{2}\, e^{-iEt/\hbar}\, a'(t) \end{cases} \tag{4.13}$$

where

$$\dot{\theta} \;=\; \frac{2\dot{V}E}{4V^2 + E^2} \tag{4.14}$$

Again, let's examine the perturbative limit when $a'(t) \approx 1$:

$$b'(t_0) \;\approx\; -\frac{1}{2}\int_0^{t=t_0} \dot{\theta}e^{-iEt/\hbar}\mathrm{d}t \tag{4.15}$$

Despite the structural similarities between Equations 4.3 and 4.15 (or Equation 4.2 and 4.13), they have very different physical interpretations. The phase of the coupling ($\sim E/\hbar = \omega_a - \omega_b$) now corresponds to the energy gap between the two *diabatic* states, and the amplitude of the coupling ($\sim \dot{\theta}$) depends on the molecule and laser field parameters in a more complicated manner. We note the following: (1) the coupling between states is proportional to the time derivative of the molecule-field coupling, V(t), i.e., non-adiabaticity is important for strong fields which vary rapidly. The coupling amplitude is maximum when the instantaneous field crosses zero. However, due to the phase term, the population change is not necessarily maximal at zero field. In fact, at zero field, the population in one state could be increasing or decreasing, depending on whether the relative phase is constructive or destructive (also see Fig. 4.5). (2) The energy difference between the states influences both the coupling amplitude and the phase evolution. For an energy gap E much larger than V, this coupling amplitude is suppressed as $1/E$. A smaller energy gap minimizes the phase evolution, and hence, more constructive transfer. (3) The detuning Δ no longer plays a significant role - hence this mechanism doesn't require a resonance condition or nuclear dynamics. (4) Population transfer now takes place on a sub-cycle timescale, since $\dot{V}$ contains the carrier frequency. In contrast, in the case of resonant transitions, the RWA effectively eliminates the carrier frequency and the population transfer is better measured with the pulse area.

We note that we've used the *diabatic* representation to solve the TDSE in the case of resonant transition, and the *adiabatic* one in the case of non-adiabatic transition. This gives us a similar set of solutions (4.3 and 4.15) for easy comparison. In addition, it suggests that two mechanisms are important in different coupling regimes – resonant transition requires a small detuning but can otherwise occur with a moderate Rabi frequency, while non-adiabatic transition requires a large Rabi frequency.

Now a natural question arises – how do we reconcile these two seemingly different mechanisms? Can they co-exist or do they only manifest themselves separately in different parameter spaces? To answer this question, let's go back to the TDSE in the *adiabatic* basis, applying Eq. 4.5, 4.6 and 4.7 to $i\hbar\frac{\partial}{\partial t}\Psi(t) = H(t)\Psi(t)$:

$$i\hbar\frac{\partial}{\partial t}\Psi'(t) \;=\; D(t)\Psi'(t) - i\hbar U^{-1}(t)\frac{\partial U(t)}{\partial t}\Psi'(t) \tag{4.16}$$

Since $D(t)$ is diagonal, the second term is the only coupling among states. When $\frac{\partial U(t)}{\partial t}$ *is small*, we can neglect this term, which is equivalent to the adiabatic approximation, which states that all populations remain in the same adiabatic states through time. On the contrary, when this term is *not* negligible, we have non-adiabatic transitions, Eq.4.12. Now how does the resonant transition enter this equation? We know it must be contained in the second term as well since there is no other coupling. It turns out that there is some subtlety in the condition "$\frac{\partial U(t)}{\partial t}$ *is small*". To see this, let's go back to the 2-level system described earlier. Let's assume the field is now on resonance but very weak. From Eq. 4.12 and 4.14 we see that the coupling $U^{-1}\frac{\partial}{\partial t}U \sim \dot{\theta} \propto \chi$, which is consistent with a π-pulse of duration $t = \pi/\chi$. In other words, while on resonance, no matter how small the coupling χ is, as long as we wait long enough, we can always have complete population transfer. The reason for this lies in the coupling phase – while off resonance, even though a large coupling amplitude induces a large transition rate, the wave function transfered at each time instances can add either constructively or destructively. While on resonance, all transfered wavepackets add up in phase and therefore even a small coupling amplitude can move a large amount of population. In this aspect, the resonant transition is really a special case of the non-adiabatic transition. However, we will keep the distinction between these two mechanisms in the following discussion for two reasons: (1) The off-resonance non-adiabatic transition is only noticeable when the coupling is strong, such as in SFI. And in order to study this phenomenon, we should avoid any resonances. (2) The resonant transition is often effected by the nuclear motion and therefore offers a way of studying the nuclear dynamics in the ion.

4.2 Experimental Data

In the last section, we saw that resonance is a relationship between the energy gap and laser carrier frequency ($\Delta = \omega - (\omega_b - \omega_a)$), and the former depends on time indirectly via nuclear motion. On the other hand, non-adiabaticity depends on the energy gap (coupling phase) and the instantaneous field (coupling amplitude) independently. This implies that resonant transitions facilitated by nuclear dynamics prefer relatively long pulses for they allow more time for the nuclear wave packet to reach a resonance, while non-adiabatic transitions are mostly sensitive to the carrier frequency and the peak field strength of the pulse [1]. In order to compare these two effects, we carry out four coincidence VMI experiments measuring the indirect ionization yields, using 2 molecules bromoiodomethane (CH_2BrI) and trifluoroiodomethane (CF_3I), and 10 and 30 fs pulses. We choose these two molecules because they have similar molecular structures (both belonging to the halomethane family)and IPs, but the former shows much more indirect ionization than the latter, as shown in Sec. 3.3. The setup is otherwise similar to that described in Sec. 2.2. Since this experiment involves the comparison of two different molecules, the pulse intensity is chosen to yield a similar ionization rate for all four measurements presented below. However, we note that for each molecule, the pulse peak intensities for 10 and 30 fs pulses are estimated to be within a factor of 2. Even though this is a somewhat large variation in SFI, since we're mainly concerned with the post-ionization dynamics, which are mostly 1-photon processes, this variation in intensity should not change our interpretation of the underlying physics.

Figure 4.2 and Figure 4.3 show photoelectron spectra measured in coin-

---

[1] The time variation of the intensity envelope will be important only when the pulse is very short, that is, the time scale of the change in the intensity envelope is comparable to the period of the carrier.

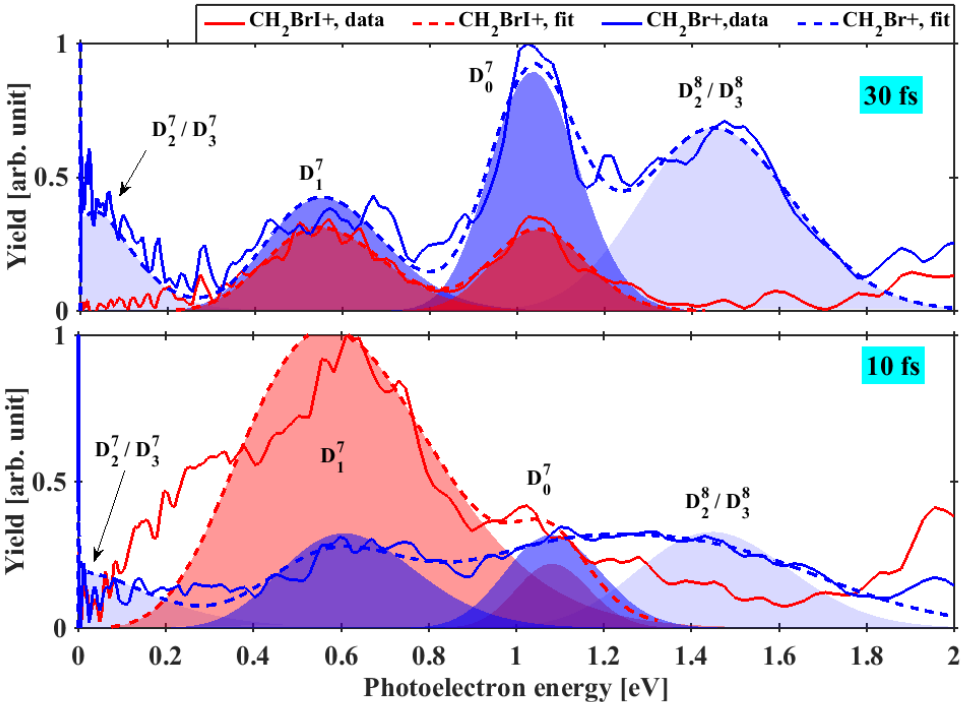

Figure 4.2: Coincidence photoelectron spectra for CH$_2$BrI, with 30 fs (upper panel) and 10 fs (lower panel) pulses. Solid lines are measurements and dashed line are fits, which are the sums of all the shaded Gaussians of the respective color. Labels D_i^n denotes electrons n-photon ionization to the ith excited ionic state. i=0 indicates the ground ionic state. Spectra in each experiment are scaled to a fixed value – the maximum in either parent's or fragment's photoelectron yield.

cidence with photoions, for CH$_2$BrI and CF$_3$I , respectively. The top panels are measured with 30 fs pulses and the bottom ones with 10 fs ones. Red curves are the photoelectron spectra associated with the parent ion and the blue ones with the dominant fragment ion. For these two molecules, the parent and the chosen fragment account for more than 90% of the yield in these experiments. Solid lines are measured data. Shaded areas are Gaussian fits whose sums are plotted as dashed lines.

In order to fit the data, we start with a multi-Gaussian fit of the spectra in coincidence with the parent ion for 30 fs pulses. Then we fit the spectra associated with the fragment ion and impose the constraint that the indirect

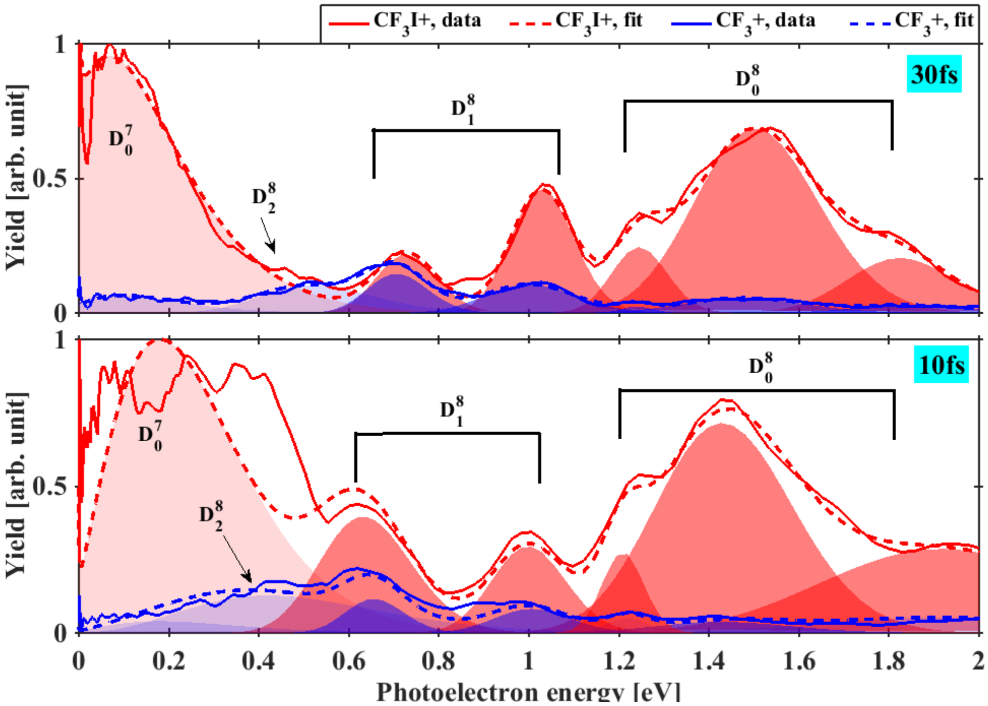

Figure 4.3: Coincidence photoelectron spectra for CF_3I, with 30 fs (upper panel) and 10 fs (lower panel) pulses. Solid lines are measurements and dashed line are fits, which are the sums of all the shaded Gaussians of the respective color. Labels D_i^n denotes electrons n-photon ionization to the i^{th} excited ionic state. i=0 indicates the ground ionic state. There are multiple peaks which are collectively labeled by a single ionic state. They are Freeman peaks which shift into resonances at different intensities, therefore appearing with kinetic energies due to the ponderomotive shifts (see Ch.1 for more discussion on Freeman resonance). Spectra in each experiment are scaled to a fixed value – the maximum in either parent's or fragment's photoelectron yield.

ionization peaks have the same centers and widths as their counterparts associated with the parent ion. This constraint is due to the fact that indirect ionization is concerned with post-ionization dynamics, which does not affect the liberated electron. Next, we fit the spectra taken with a 10 fs pulse. Generally speaking, the spectra may be shifted compared to those taken with 30 fs pulse since the central frequencies are not exactly the same. So we allow a constant shift of all the Gaussian fits. Moreover, since the optical spectrum is broader for a short pulse, we constrain the fitting to be no narrower than their counterparts for the 30 fs pulse. All measurements and fits are color-coded to distinguish between electrons in coincidence with parent and fragment ions. The sum of shaded areas gives the total fit plotted in dashed lines, which is to be compared with the measurement plotted in solid lines. Now we can simply integrate each shaded Gaussian to calculate the yield associated with each pathway. Note that for CF_3I, we have named several peaks collectively D_0 or D_1. The reason is that there are multiple intermediate neutral states which shift into resonance at various intensities. The photoelectrons produced via each of these resonances are born at different intensities and experience different ponderomotive shifts[78].

Species	D_0(eV)	D_1(eV)	D_2(eV)	D_3(eV)
CH_2BrI [63]	9.69	10.26	10.91(d)	11.12(d)
CF_3I [65, 66, 67]	10.37	11.09	13.02(d)	15.17(d)

Table 4.1: Ionization potentials at the FC point for CH_2BrI (from *ab initio* electronic structure calculations) and CF_3I (experimental values from the references). D_0 denotes the ground ionic state and D_i denotes the ith excited ionic state. "(d)" labels dissociative states.

.

	CH_2IBr		CF_3I	
	D_0^7	D_1^7	D_0^8	D_1^8
30 fs	0.67	0.50	0.05	0.22
10 fs	0.58	0.14	0.07	0.13

Table 4.2: Ratio of non-dissociative states that undergo post-ionization excitation, which is calculated as $\frac{\text{dark blue area}}{\text{dark blue area + dark red area}} = \frac{D_0 \text{ (or } D_1\text{) peak in coincidence with fragment}}{\text{sum of two } D_0 \text{ (or } D_1\text{) peak}}$ in Figure 4.2 and 4.3. We estimate the errors in these ratios be about ±0.1, based on the background signal level.

We are interested in indirect ionization, which in these two molecules corresponds to those peaks labeled by D_0^n and D_1^n, which are the only non-dissociative states. For a quantitative comparison, we ask two questions:

what percentage of the initially populated non-dissociative ions are field-excited to dissociative states? And how does the ratio change with various parameters? Table ?? lists the percentage of the non-dissociative ionic states that undergo indirect ionization. We note the following: (1) For CH_2IBr, the amount of indirect ionization generally decreases with pulse duration. This suggests that, under the conditions of our experiment, the resonant transition plays an important role. The amount of indirect ionization that persists in going from 30 fs to 10 fs could be due to two factors: First, since the non-adiabatic transition is less sensitive to pulse duration, it's likely the cause of the indirect ionization associated with D_1^7 for 10 fs pulses. And the difference in yield between 10 and 30 fs experiments is likely a result of resonant transition which is sensitive to the pulse duration. Second, even though 10 fs pulses leave little time for nuclear dynamics, because of a broader range of available photon energies and a certain spatial spread of the nuclear wavepacket, it's still possible for some portion of the wavepacket to reach a resonance, if it's close to the FC point. This should contribute to the indirect ionization associated with D_0^7 since the ratio is large comparing to that for D_0^7 and from electron structure calculation (see Section 4.4) we know there is a resonance near the FC point. (2) In comparison, there is much less indirect ionization in CF_3I, regardless of the pulse duration. This suggests there is no resonant transition between D_0 or D_1 and higher lying dissociative states in the cation. (3) Note in Table 4.1 that the energy gaps between non-dissociative and dissociative states in CH_2IBr are smaller than our photon energy (~ 1.6 eV), as well as those in CF_3I. The smallest energy gap in CF_3I at the FC is between D_1 and D_2, and is about 2 eV. We will show in Sec. 4.3 that along the nuclear coordinate which largely describes the motion on D_0 and D_1 after ionization., there are 1-photon resonances in CH_2IBr near the FC while there is only one 2-photon resonance in the CF_3I that is far away from the FC.

4.3 Simulation of Resonant Transition

In order to better understand our experimental data, in this section and the next, we will present two simulations, one on resonant transition and the other on non-adiabatic transition. All molecular parameters used here are obtained from *ab initio* electronic structure calculations obtained from

Tamás Rozgonyi [2]

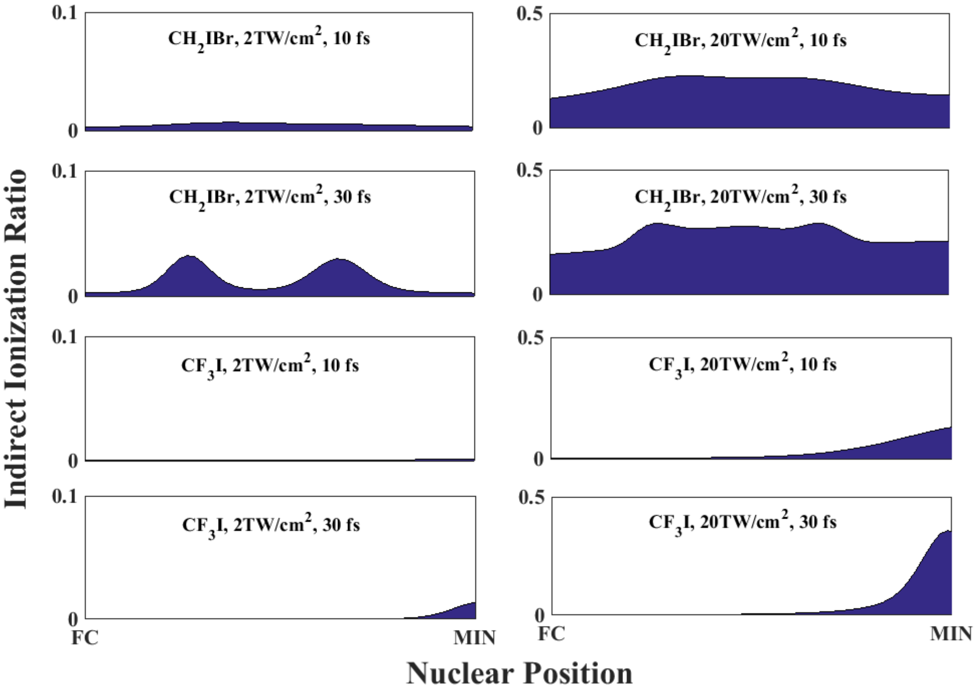

Figure 4.4: Fractions of the initial ionic states populations (D_0 and D_1) excited to higher states, for 10 and 30 fs pulses, and 2 and 20 TW/cm^2 peak intensities. 8 ionic states for CH_2IBr and 10 for CF_3I are included in the TDSE. There are 51 uniform sampling points between FC and MIN. Each point is an average of contributions from both initial states and of 10 different orientations of the molecule with respect to the laser polarization. Note the difference in y-axis range for left and right columns.

The most straightforward way of simulating resonant transitions is to solve the TDSE, including nuclear dynamics. However, this brute force method is computationally demanding, especially when the nuclear motion is multi-dimensional. Instead, we solve the TDSE and calculate the fraction of the non-dissociative states' population that is excited to dissociative states at 51 fixed nuclear positions sampled uniformly between the Franck-Condon

---

[2] Institute of Materials and Environmental Chemistry, Research Centre for Natural Sciences, Hungarian Academy of Sciences, Budapest 1117, Magyar tudósok körútja 2, Hungary

point (FC) and the minimum of the potential (MIN), shown in Fig.4.4. This effectively tells us how much population transfer one can expect at a specific nuclear coordinate *if* the wavepacket reaches there. The results at the positions near the FC are most relevant for short pulses while those at positions close to the MIN are expected to contribute with longer pulses. The potential energies and transition dipole moments (TDM) at each nuclear position are linear interpolations of the values at FC and MIN, which are obtained from *ab initio* electronic structure calculations. 8 ionic states for CH_2IBr and 10 for CF_3I are included in the TDSE. There are two non-dissociative states in each molecule (D_0 and D_1). We manually put unity population in an *adiabatic* non-dissociative state (D'_0 or D'_1) at the peak of the pulse and then solve the TDSE until the end of the pulse to calculate the fraction of the population that is excited to dissociative states (D_i, $i \geq 2$). Note that in the absence of the field, $D_i = D'_i$. The relative orientation of the TDMs with respect to the field polarization is taken into account by uniformly averaging the simulation results over 10 different angles.

In order to check the validity of our approximation of linearly interpolating energies and TMDs, we solve the TDSE with nuclear dynamics on a 3-state system (the ground neutral state, the ground ionic state and an excited ionic state). The system is modeled on CH_2BrI, that is, using the potential energy curves (PEC) and TDMs from the *ab initio* calculation. The simulation shows a similar result: significantly more population in $D_{2/3}$ with a 30 fs pulse than with a 10 fs pulse. This approach is difficult to apply to CF_3I because, unlike in CH_2IBr, the dynamics in CF_3I doesn't occur along a single nuclear coordinate. So for simplicity, we only present the first approach here.

In Figure 4.4 , we plot the population percentage in dissociative states (starting with all the population in a non-dissociative state). As mentioned earlier, we see that there are two resonances in CH_2BrI which are closer to the FC point. The only resonance in CF_3I in this simulation only comes at around the MIN point. At off-resonance locations, there is a lot more indirect ionization with 20 TW/cm^2 pulses than 2 TW/cm^2, especially for $CH2_IBr$. The fact that there are less non-adiabatic transitions in CF_3I than CH_2IBr results from a larger energy gap (see Table 4.1) as well as weaker TDMs. Finally, we note that at the intensity closest to our experimental conditions (10$\sim$20 TW/cm^2), the amount of indirect ionization in both molecules is in qualitative agreement with our measured results.

4.4 Simulation of Non-adiabatic Transition

The second simulation is aimed to better illustrate the effect of non-adiabatic transitions. We consider a 2-level system in a laser field, (Fig. 4.5). The TDMs used here are borrowed from the *ab initio* calculation in CH_2IBr, while we set the pulse intensity, energy gap and detuning manually to explore different regimes. For simplicity, we assume ionization via tunneling at the peak of the pulse by manually putting all the population in the *adiabatic* state D_0'. Then we solve the TDSE and see how the populations in both *adiabatic* and *diabatic* states change as the field turns off. This simple assumption aims to illustrate the behavior of non-adiabatic transitions. Indeed, the coupling rate is independent of the population in each state. Were the adiabatic approximation valid, we would have expected the population to remain in the lower *adiabatic* state D_0' the whole time as the field oscillates to zero. As the *adiabatic* and *diabatic* states coincide in the absence of the field, this implies that the system would have been in the ground ionic state at the end of the pulse. As we can see in panel (b) in Fig. 4.5, this is close to the case with 2 TW/cm^2 pulse. The missing population in D_0' can be seen as the non-adiabatic response of the system to the applied field. This effect is more obvious with higher intensity, as shown in panel (a), where the peak intensity is 20 TW/cm^2. In addition to the dependence on pulse intensity, we also see that the amount of non-adiabatic transfer is effected by the carrier frequency, comparing panel (a) and (c), and gap energy, comparing panel (a) and (d), as expected.

To summarize, we've measured the pulse duration dependence of indirect ionization yields for two molecules, where we see most indirect ionization yields when there are resonant transitions. However, in a strong field, off-resonance non-adiabatic transitions also have a non-negligible contribution to the indirect ionization. Our simulations on resonant transitions provide a qualitative agreement with experimental data and confirms our hypothesis that there is much more resonant contribution in CH_2IBr than CF_3I. The simulation on non-adiabatic transition illustrates the dependence on the pulse intensity, carrier frequency and gap energy. It also suggests an increasingly important role of off-resonance non-adiabatic transitions as we go to more intense laser fields. Consequently, although the experimental data is consistent with a small non-adiabatic contribution, a more specifically designed experiment is needed to isolate this effect.

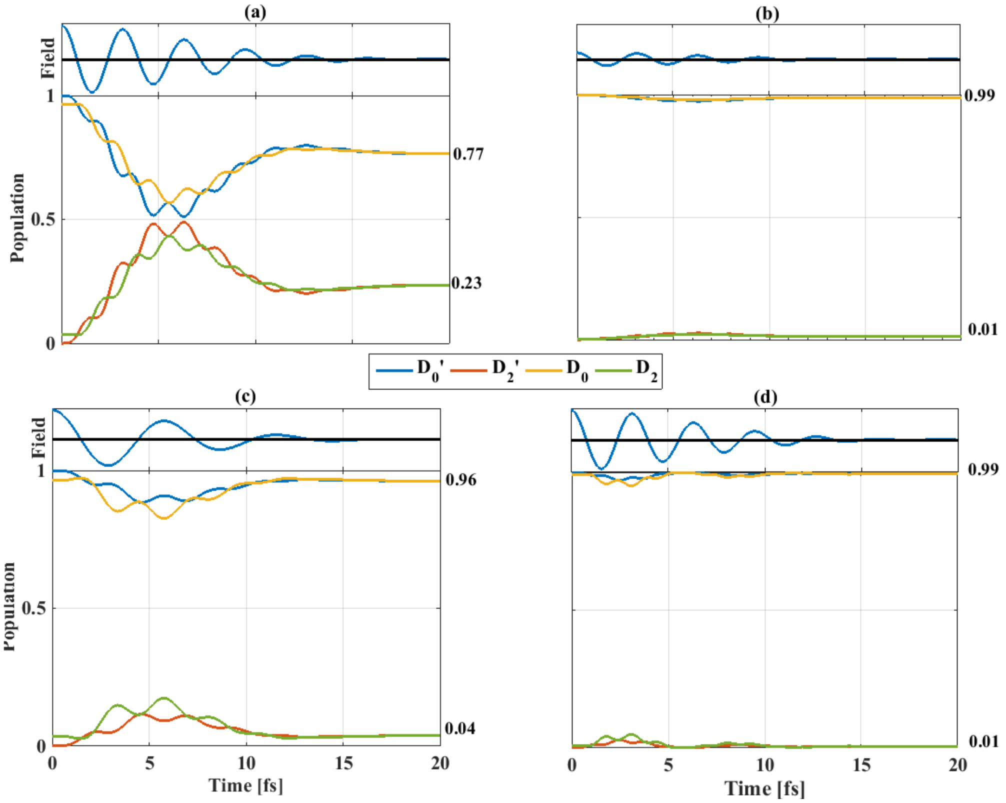

Figure 4.5: *Adiabatic* and *diabatic* state populations during the laser pulse. A unit population is put into the *adiabatic* state D_0' by hand at time t=0. The populations oscillate as the field goes to zero, at which point the *adiabatic* and *diabatic* states become identical. In the end, some population is left in the second *diabatic* state, D_2. (a) 20 TW/cm^2 peak intensity, 1 eV energy gap, 1.3 eV photon energy. (b) 2 TW/cm^2 peak intensity, 1 eV energy gap, 1.3 eV photon energy. (c) 20 TW/cm^2 peak intensity, 1 eV energy gap, 0.7 eV photon energy. (d) 20 TW/cm^2 peak intensity, 2 eV energy gap, 1.3 eV photon energy.

Chapter 5

Strong Field Molecular Double Ionization

We now move our focus to molecular double ionization (DI). DI in a strong laser field has been of great interest as an important part of light-matter interaction and as a window to electron correlation [79, 80]. Since the early observations of DI over three decades ago[81, 82, 83], there have been three main proposals for the underlying dynamics: (1) In sequential DI shown in panel (a) in Fig.5.1, two electrons are removed from the atom/molecule independently, one after the other [81, 83, 84]. This turns out to be important in the case of saturated single ionization (SI), and it persists for elliptically polarized light. (2) In non-sequential re-scattering shown in panel (b), one electron first tunnels into the continuum, then it is driven back to the ion core in the alternating laser field, where it inelastically re-scatters and liberates a second electron. This includes the possibility that the re-scattering only delivers enough energy to excite the second electron, which is then tunnel-ionized at a later time in the field[85, 86, 87, 88, 89]. Since this process requires the first electron to come back to the ion core, it is particularly sensitive to the ellipticity of the field. A circularly polarized light field is unlikely to produce re-scattering in noble gas atoms and small molecules. (3) In a direct "shake-off" process shown in panel (c), the sudden removal of one electron causes a quiver motion of the electron cloud that shakes off a second electron.[90] Another way of thinking of this process is to note that after the removal of the first electron, the electronic wavepacket of the ion relaxes to a new minimal – from an eigenstate of the molecule to one of the ion. This excited wavepacket has a non-trivial projection onto the continuum.

Note that both (2) and (3) involve explicit electron correlation. Most of our knowledge about DI, including these three possible mechanisms, come from the study of rare gas atoms, in which non-sequential re-scattering appears to play a dominant role.[84, 83, 89, 91, 92, 93] For other atoms and molecules, the situation is richer and more complicated. [94, 95, 96, 97, 98]

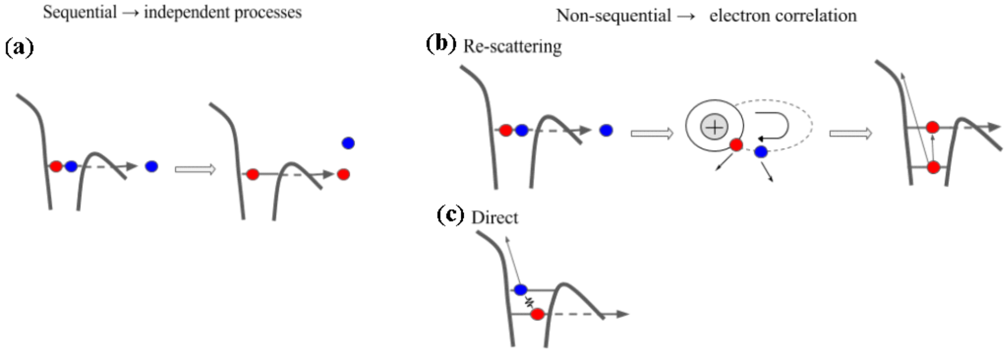

Figure 5.1: Three mechanisms underlying strong field DI.

In the rest of this chapter, we first present an observation of enhanced DI in the molecule 1,3-Cyclohexadiene (C_6H_8, abbreviated to CHD). We utilize ion-ion coincidence to separate DI from SI, where we find a roughly constant kinetic energy release (KER) in all fragmentation channels. A survey on 4 different molecules suggests that the DI enhancement is connected to molecular structure. Another measurement in which we vary the ellipticity of the laser field suggests the DI enhancement is *not* due to re-scattering. In the last section, we present a *full* coincidence measurement of DI using the TimepixCam, where we detect two electrons and two ion fragments from an DI event. The hope is that this new setup with the TimepixCam will eventually allow us to study the electron-electron correlation during DI and help us understand the relationship between the electronic structure and the DI enhancement.

5.1 Ion-ion Coincidence Measurement

This first VMI experiment is carried out in the non-coincidence mode where we measure the ion fragments produced from the dissociative SFI of 1,3-Cyclohexadiene. Fig. 5.2 shows the results for the $C_2H_x^+$ and $C_4H_x^+$ frag-

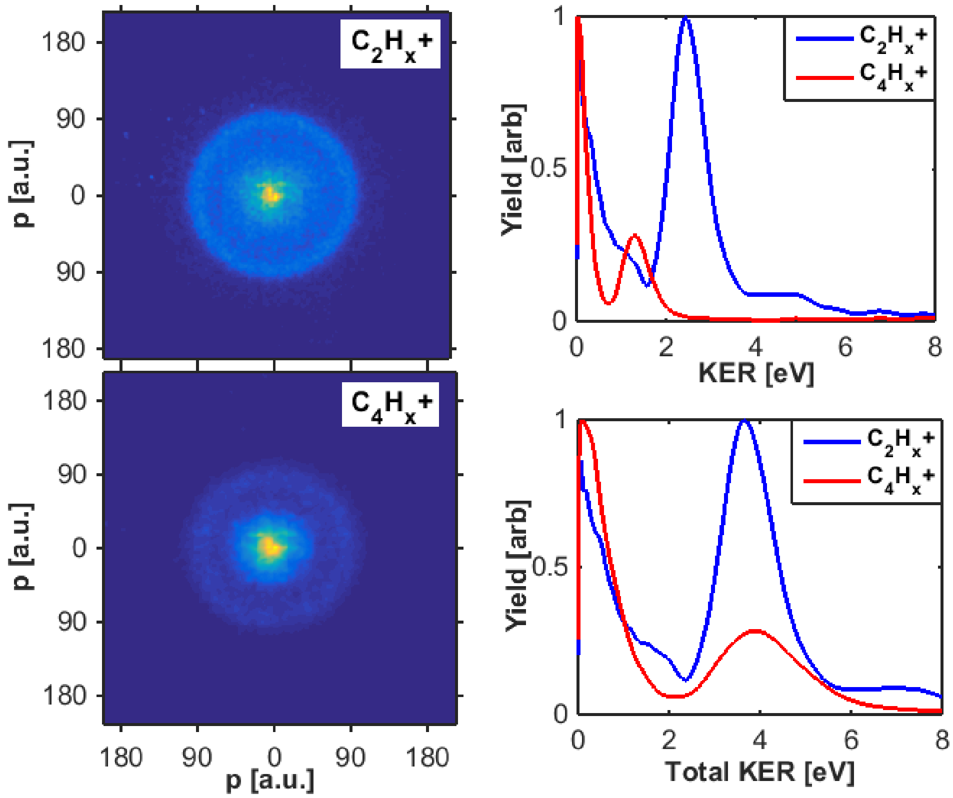

Figure 5.2: 1,3-Cyclohexadiene ionization measurement with 10 fs pulse. Left panels show raw 2D VMI images of $C_2H_x^+$ and $C_4H_x^+$ fragments from 1,3-Cyclohexadiene before any processing. The top right panel shows the normalized ion yield vs. KER (kinetic energy release), and bottom right panel shows ion yield vs. total KER, obtained by applying an Abel inversion, angular integration and a low-pass Fourier filter to the raw image. The total KER is calculated based on momentum conservation, assuming two-body breakup.

ments. The subscript x indicates that we include fragments with different numbers of hydrogen atoms - mostly 2-4. From the raw VMI images two main features are evident: a central spot and an outer ring, corresponding to ion peaks in the photoion spectra with low and high kinetic energy release (KER), respectively. We denote these as slow peak (low KER) and fast peak (high KER). Measurements of other fragment ions show similar slow and fast peaks in the KER spectra. While the energy of the fast peak varies between fragments, we can calculate the total KER for a given fragment assuming a two-body axial breakup and applying momentum conservation. It turns out all fragments have roughly the same total KER, which is about 4 eV. This large and roughly constant energy for fragment pairs leads us to conjecture that the fast peaks result from DI followed by Coulomb explosion.

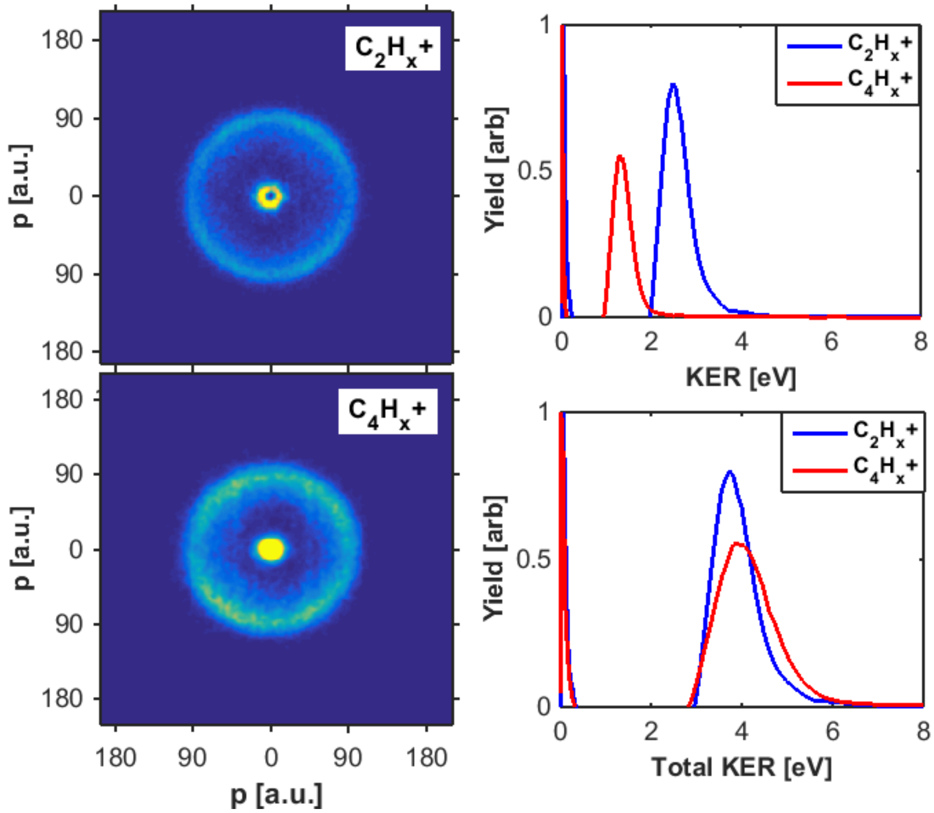

Figure 5.3: 1,3-Cyclohexadiene fragments $C_2H_x^+$ and $C_4H_x^+$, similar to Figure 5.2 but measured in coincidence with 9 fs pulses. Left panels show VMI raw images and right panels show ion yield as a function of either KER measured from the VMI image or total KER calculated assuming two-body breakup. See the text for a more detailed description.

In order to directly verify our DI conjecture, we carry out an ion-ion coincidence measurement. The setup is similar to that used for the SI experiment except that now VMI images are selectively recorded when there are exactly two hits on the image and for which the vector sum of the momenta for the two fragments is zero in the plane of the detector. This allows us to measure the momentum distribution for charged fragments which are produced in pairs from the same parent molecule - i.e. fragments which come from DI. Figure 5.3 shows the same type of images and plots of the same two fragments as in Figure 5.2, but now measured in coincidence. The left two panels show the 2D VMI images for $C_2H_x^+$ and $C_4H_x^+$ fragments, while the right panels show the integrated yield vs KER and total KER assuming two body breakup. The presence of the outer rings (fast peaks) directly confirms our DI conjecture since fragments produced from a singly ionized molecule cannot contribute to the coincidence measurements, which requires two fragment ions who make up the whole molecule. The center spot appearing in the raw coincidence images is mostly due to SI since our metric for admitting Coulomb explosion pairs allows some uncertainty in their total momentum. Low KER ions coming from two SI events could easily pass this filter. This uncertainty ϵ (such that the sum of the momenta $p_1 + p_2 \leq \epsilon$) in calculating the conservation of momentum is necessary because discrete detection and the uncertainty in centroiding. ϵ is set to be the FWHM of the fast peak in the non-coincident VMI image. Note that we focus on the DI that yields high KER ion fragments. Some of the low KER fragments may also result from DI, so the fast peak yield is only a lower bound on DI yield. Furthermore, because we normalize each spectrum to its own maximum, which often corresponds to the height of the slow peak, the fast peaks for the two fragments appear with different heights. However, the absolute integrated yields of these fast peaks are equal. The difference in their shape (which is very small once set to the same height) is due to the nonzero ϵ. If we halve the value of ϵ, then the two peaks are identical.

Having established the origin of the high KER fragments as DI, we turn back to Figure 5.2. Electronic structure calculations indicate that the vertical ionization potential is about 1 eV above the adiabatic ionization potential for the dication. A previous study[99] shows that the dissociation barrier is more than 2.5 eV, even though there is a positive KER (less than 1 eV) upon dissociation. This leads us to believe that the ground state of the dication is bound. This is also consistent with the narrow C_3H_x peak in Fig.5.4. With the ground state being bound, and the dissociation energy being small, the high KER peak comes from the population of highly excited states of the dication.

Analysis of the ionization yields shows that of all ionization events, about

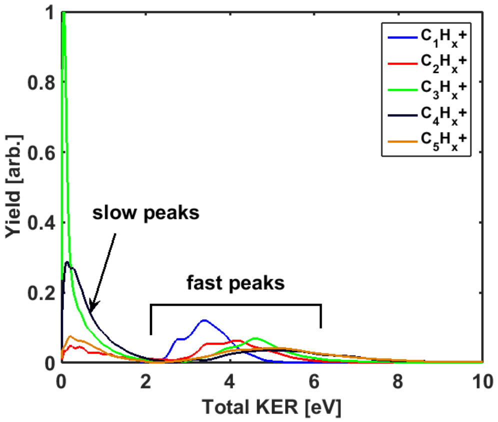

Figure 5.4: Yields of all fragment ions for 1,3-cyclohexadiene (CHD) plotted as a function of total KER. Due to the size and shape of the slow peak in the $C_3H_x^+$ spectrum, we argue that it contains contributions from both $C_3H_x^+$ and CHD^{++}. We subtract the CHD^{++} contribution from this peak in Figure 5.5 based on the fitting procedure described in the text.

40% correspond to DI, 38% of which dissociates producing fragments with high KER. This fraction is much higher than what one would expect from re-scattering. These values are calculated from a set of CHD data shown in Figure 5.4, taken with 30 fs linearly polarized pulse with a peak intensity of 26 TW/cm^2. The most striking feature is the high yield in the $C_3H_x^+$ slow peak. The shape and height of this slow peak differs notably from the others. Given the fact that the arrival time of a fragment at the detector depends only on the mass to charge ratio, a significant portion of this peak can be due to CHD^{++}. In order to single out the contribution of stable dication, assuming CHD^+ and CHD^{++} have the same momentum distribution (given that they come from the same neutral molecules and have no appreciable momentum exchange partner, and taking into account the fact that a doubly charged ion will be accelerated with twice the kinetic energy), we first fit the slow peak in the parent cation spectrum with a Gaussian function, denoted by f(E). Then we fit the $C_3H_x^+$ slow peak with two Gaussian functions in the form of $A \cdot f(E) + B \cdot g(E)$, that is, the contribution from CHD^{++} is constrained to have the same distribution as that of CHD^+. Then the amplitude A gives us an estimate of how much of the slow peak in $C_3H_x^+$ is CHD^{++}. Now we can define and calculate the dissociation ratio R_{diss} and double ionization ratio

R_{double} :

$$
\begin{aligned}
R_{\text{diss}} =& \frac{\text{CHD}^{++}_{\text{diss}}}{\text{CHD}^{++}_{\text{non-diss}} + \text{CHD}^{++}_{\text{diss}}} && (5.1)\\
=& \frac{\frac{1}{2}f_{C3} + f_{C4} + f_{C5}}{s_{C3} + \frac{1}{2}f_{C3} + f_{C4} + f_{C5}} && (5.2)\\
R_{\text{double}} =& \frac{\text{CHD}^{++}}{\text{CHD}^{+} + \text{CHD}^{++}} && (5.3)\\
=& \frac{s_{C3} + \frac{1}{2}f_{C3} + f_{C4} + f_{C5}}{\text{all peaks} - \frac{1}{2}f_{C3} - f_{C4} - f_{C5}} && (5.4)
\end{aligned}
$$

where f_{C3} and s_{C3} denote the integrated yield of $C_3H_x^+$ fast and slow peaks, respectively, Since one double ionization event produces a pair of ions, we only consider the yield for one of the fragment ions, say, either f_{C2} or f_{C4}, but not both. For this reason, we place a factor of $\frac{1}{2}$ in front of f_{C3}. Then the total number of double ionization events is given by: $s_{C3} + \frac{1}{2}f_{C3} + f_{C4} + f_{C5}$. Now if we integrate over all peaks in the spectra, we would have doubly summed the contribution of dissociative CHD^{++}. So subtracting this gives us the actual number of ionization events, $\text{CHD}^{+} + \text{CHD}^{++}$. All yields are corrected for the mass-dependent efficiency of the MCPs [100].

5.2 Enhanced DI in Conjugated Molecules

The position of the high KER peak indicates that the DI process leaves the doubly charged parent ion in a highly excited state, with more than 4 eV of energy above the dissociation barrier. In addition, the DI yields in certain fragments are comparable to the SI yields. This is surprising given that this experiment is carried out at relatively low intensities (~ 20 TW/cm^2) – well below the saturation intensity (~ 80 TW/cm^2 [101]). Measurements on rare gas atoms at these intensities show roughly 2 orders of magnitude difference in the ratio of double to SI yield.[84]

In search of the underlying mechanism of enhanced DI yield and higher KER, we carry our similar non-coincidence measurements on other molecules. Figure 5.5 shows the results for 4 different molecules: 1,3-Cyclohexadiene, 1,3-Butadiene, Cyclohexane and Cyclopentane. As before, these show the normalized yield as a function of total KER, calculated from the measured

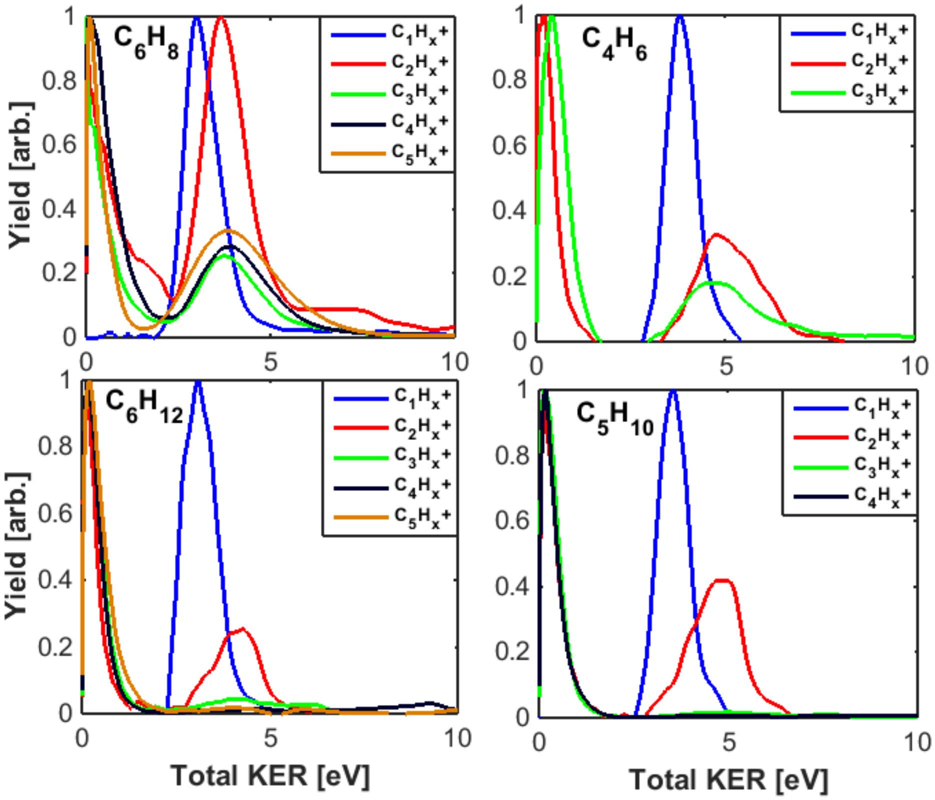

Figure 5.5: Fragment ion yields as a function of total KER (assuming two-body breakup) for 1,3-Cyclohexadiene, 1,3-Butadiene, Cyclohexane and Cyclopentane with 10 fs pulse.

KER assuming two-body breakup. The data is smoothed by applying a low-pass Fourier filter to eliminate high-frequency noise which is exacerbated by the inverse Abel transform. We focus on the fast peaks. These molecules were chosen to highlight possible systematic trends: 1,3-Cyclohexadiene and Butadiene are conjugated molecules, with alternating single and double bonds. Cyclohexane and Cyclopentane are unconjugated molecules, with only single bonds and no π orbitals. Further, Butadiene is linear while the other molecules are cyclic (i.e., having a ring structure).

The upper left panel contains all fragment ions of C_6H_8 which we know for certain undergoes DI. In fact, all fast peaks have roughly the same total KER, with the exception of $C_1H_x^+$. We see similar behavior in C_4H_6 but not

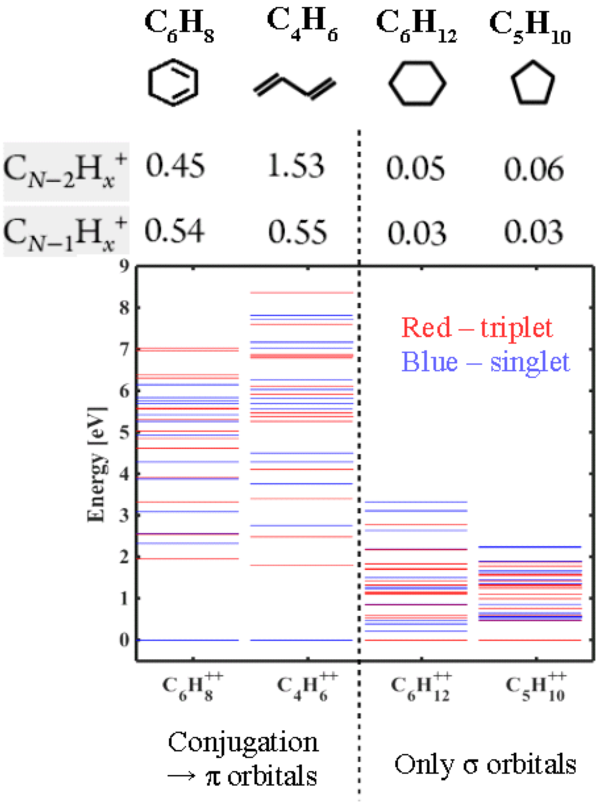

Figure 5.6: Ratios of fast and slow peak yield for the two heaviest fragments for all 4 molecules. Together with energies of the first 15 singlet (blue) and triplet (red) states of the dications, from Table 5.1 and Table ??

C_6H_{12} or C_5H_{10}. In the latter two cases, there are fast peaks in the spectra for the $C_1H_x^+$ and $C_2H_x^+$ fragments, but not for their two-body breakup partners. This could be due to mutil-body breakup, in contrast to two-body breakup, as well as background signals (eg., ionization of the pump oil followed by dissociation). We calculate the ratios of fast and slow peak yields for the two heaviest fragment ions, listed in the table in Fig.5.6. Note there is more than an order of magnitude difference in the ratios between the conjugated and unconjugated molecules. These observations lead us to believe that this enhanced DI takes place in both C_6H_8 and C_4H_6, but not in C_6H_{12} or C_5H_{10}. Before turning to electronic structure calculations, we present the results of two further measurements.

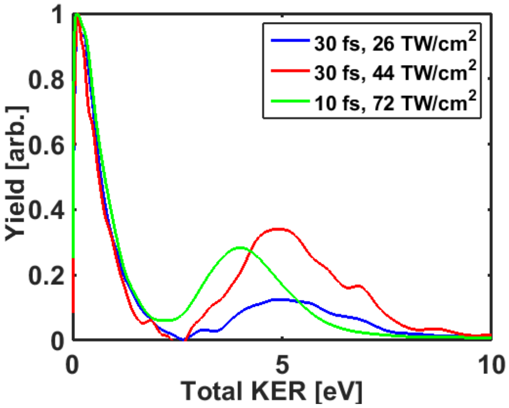

Figure 5.7: $C_4H_x^+$ yield from 1,3-Cyclohexadiene as a function of total KER, for two different intensities and pulse durations.

Fig. 5.7 shows the 1,3-Cyclohexadiene fragment $C_4H_x^+$ yield vs. total KER for two different intensities and pulse durations. Comparing the two measurements taken with 30 fs pulses, DI contributes more with increasing peak intensity. It also appears that the enhanced DI is not particularly sensitive to the pulse duration and is still significant in the impulsive limit - for pulse durations shorter than the fastest vibrational period in the molecule, where vibrational dynamics are essentially 'frozen'. This suggests that nuclear dynamics do not play an important role in the enhanced DI.

In order to investigate the possibility of re-scattering induced DI, we performed measurements of the DI yield as a function of ellipticity. The ellipticity ϵ is defined such that the field can be written as $E(t)[cos(\omega t)\hat{x} + \epsilon sin(\omega t)\hat{y}]$, assuming z-axis as the direction of propagation, with $E(t)$ and ω being the temporal envelope and carrier frequency, respectively. Given this definition, linearly polarized light has $\epsilon = 0$ and circularly polarized light has $\epsilon = 1$. Varying the ellipticity of the pulse with a fixed pulse energy leads to a change in the peak intensity. Thus, one must choose between performing the ellipticity measurements with a fixed pulse energy or fixed peak intensity. For simplicity, we performed the measurements for fixed pulse energy and calculated the ratio of the SI to DI yield in order to account for intensity dependent variation of the DI yield.

In the case of noble gas atoms, measurements of the ionization yield as a function of ellipticity have been used to test for re-scattering since the returning electron is less likely to recollide with the core for increas-

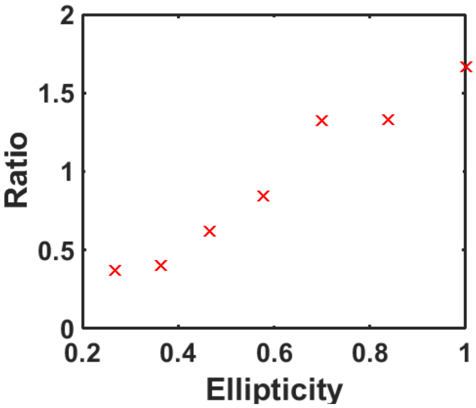

Figure 5.8: Ellipticity dependence of DI for C_4H_x+ fragment of 1,3-Cyclohexadiene. The ratio between the fast peak (outer ring) and slow peak (central patch) is plotted as a function of ellipticity. The ellipticity ϵ is defined in the text, with $\epsilon = 0$ corresponding to linearly polarized light and $\epsilon = 1$ corresponding to circularly polarized light.

ing ellipticity[102, 103]. However, in the case of polyatomic molecules and some atoms, the situation is more complicated, and the ellipticity dependence of re-scattering is not as straightforward as in the case of atomic ionization[104, 105]. Our measured ellipticity dependence in Fig. 5.8 shows that the double to SI yield ratio increases with ellipticity, suggesting that the DI is not driven by re-scattering. This is consistent with the high DI yield, since one would expect a relatively small recollision cross section given the lateral spread of the electron in the continuum during a half cycle of the pulse.

5.3 Electronic Structure Calculations

Here we try to connect the ionization dynamics to molecular structure and see from which orbitals electrons are removed during double ionization. The computational results (Table 5.1 and Table ??) shown here are obtained from Spiridoula Matsika [1]. Singlet and triplet electronic states of the dication were obtained using 2^{nd} order multiconfiguration quasi-degenerate perturbation theory (MCQDPT2)[106] as implemented in the GAMESS[107, 108]. IPs

---

[1] Department of Chemistry, Temple University, Philadelphia PA 19122

are calculated using equation-of-motion coupled-cluster singles and double (EOM-CCSD) technique implemented in Q-Chem[109]. EOM-CCSD predicts absolute IPs very accurately while the multireference methods can describe states that cannot be described by EOM-CCSD.

Tables 5.1 and ?? show the energies and configurations for the first N states of the dications. The first 15 singlet and triplet states are included. Fig. 5.6 compares the energy level structures for the four molecules we studied, illustrating how the electronic structure of the dications differs significantly for the conjugated vs unconjugated systems. Two things become clear from the figure and tables. One is that the four molecules we've studied fall into two groups: unconjugated systems whose dicationic ground state is a triplet and where there is a small energy gap between the ground and excited states, and conjugated systems whose ground state is a singlet, and excited states are about 2 eV above the ground state. Comparing Butadiene and 1,3-Cyclohexadiene, we note that the enhanced double ionization occurs regardless whether the molecule is cyclic or not. Conjugation, with its associated electronic structure seems to be the determining factor in whether or not the enhanced double ionization is observed. The difference in the pattern of excited states in the two groups of systems comes from the fact that the HOMO in the conjugated systems is a π orbital well separated from the lower energy σ orbitals. This leads to a closed shell ground state of the dication where the 2 electrons have been removed from the same orbital. Excited states are created by removing electrons from the lower energy σ orbitals which require more energy. On the contrary, in the unconjugated systems, the HOMO is a σ orbital with energy similar to many other σ orbitals. This leads to the ground state of the dication being a triplet state with the two electrons being removed from different orbitals. Many states with similar energy can be created by removing electrons from nearby orbitals.

The second interesting point that the figure and tables make clear is that states with sufficient energy to produce fragment ions having a total KER of 4$\sim$5 eV involve removing electrons from deeply bound orbitals - either both electrons come from inner valance orbitals, or one of them comes from HOMO and the other from HOMO-6 or deeper. This makes it clear that the double ionization we observe is not simply a sequential process involving the removal of the most weakly bound electrons.

So far, we've shown that there is a surprisingly high DI yield in conjugated organic molecules, which is not present in unconjugated systems. The high KER suggests ionization to states of the dication well above the second ionization potential, corresponding to the removal of deeply bound electrons. Given that this enhancement takes place at relatively low laser intensities and persists with short pulses, we believe that the enhanced DI we observe here is non-sequential. The fact that the yield increases with ellipticity of the light suggests it's not due to re-scattering, but direct electron-electron correlation. The next step is to study the behavior of the electrons coming from DI.

5.4 Quadruple Coincidence Measurement of DI Using TimepixCam

Here we present a proof-of-principle experiment where we measure all 4 charged particles from an DI event utilizing the TimepixCam. Though this new setup is still in test phase, this preliminary results show encouraging momentum correlations between two electrons coming from DI.

For testing purpose, we've used CH_2IBr in this experiment. The coincidence detection works as follows: we only consider laser shots where we see exactly two electrons and two ions. From the TOF information, we check if the two ions form a valid pair, that is, they add up to the whole molecule, say, CH_2Br+ and I+. We then check if the sum of their momenta is approximately zero. If so, we record the momenta of all 4 particles and make a correlation plot like Fig.5.9. Here, "px" denotes the momentum projected along the x-axis, which is chosen to be the laser polarization axis direction. Similarly for "py".

Let's first look at the bottom two ion-ion correlation plots. The anti-correlation is consistent with DI since two ions fragments should have the same momentum magnitude but opposite signs. It's interesting to notice that the px-px correlation has most yield on two ends while the py-py one has a bright central part. This implies that most ions coming from DI fly apart along the laser polarization direction. If we think of the dication right before the Coulomb explosion as a structure holding 2 electron holes, then these holes are aligned with the laser polarization. The top two panels show the e-e correlations. We can see a weak diagonal line in both plots, which represent a positive correlation of the electrons' momenta, that is, both electrons in some weak channel have a tendency of coming out in the same direction.

This result is encouraging not only because it shows the full coincidence

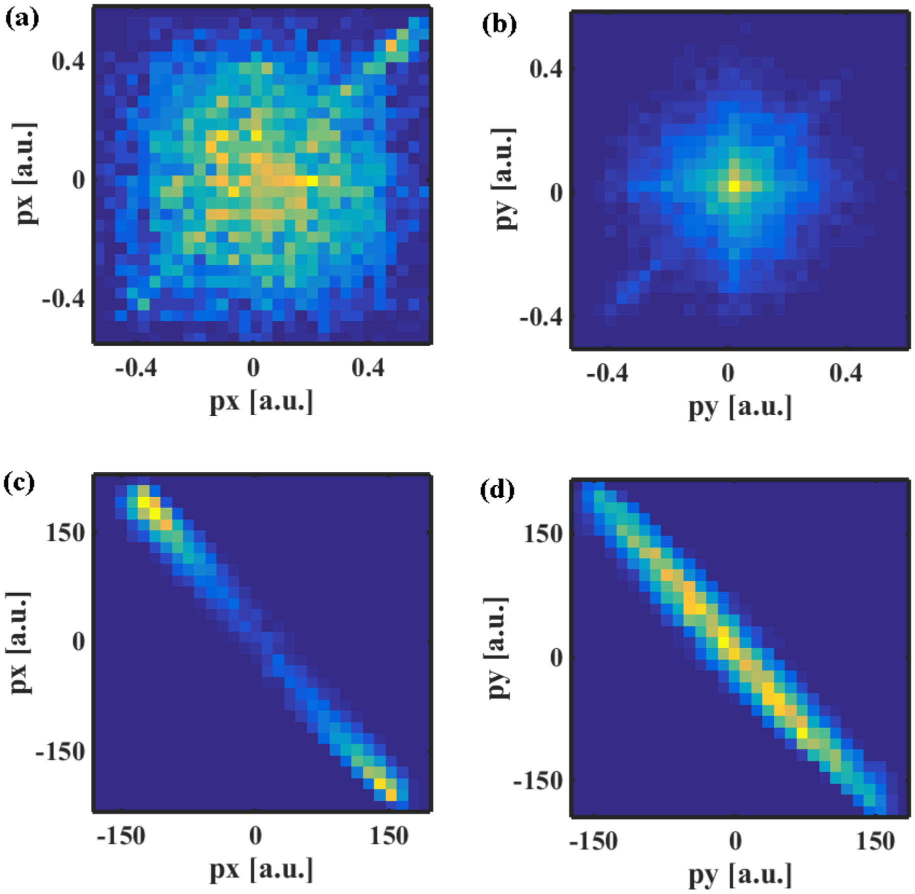

Figure 5.9: Momenta correlation plots for e-e (top) and ion-ion (bottom) pairs from DI. Each data point represents a pair of particles detected in coincidence, coming from a DI event. Top two panels are for electrons and bottom ones for ions. px is along laser polarization direction and py is perpendicular to it.

VMI detection using the TimepixCam works as expected, but also because it provides new information on the molecular dynamics of DI. The next step is to obtain better statistics and try to understand what the momentum correlation can tell us about the relationship between molecular conjugation and enhanced DI.

C_6H_8				C_4H_6			
`Energy[eV]`	`Conf.`	`Coef.`	`Spin`	`Energy[eV]`	`Conf.`	`Coef.`	`Spin`
0.00	222222220	0.96	S	0.00	22222200	0.98	S
1.95	2222222++	0.99	T	1.79	22222++0	1.00	T
1.96	222222+2+	0.97	T	2.48	2222+2+0	0.95	T
2.33	222222+2-	0.96	S	2.77	2222+2-0	0.95	S
2.55	22222+22+	0.96	T	3.41	222+22+0	0.90	T
2.56	2222222+-	0.85	S	3.76	222+22-0	0.87	S
3.10	22222+22-	0.88	S	4.11	22+222+0	0.93	T
3.32	2222+222+	0.91	T	4.28	22222+-0	0.94	S
3.88	2222+222-	0.80	S	4.50	22+222-0	0.90	S
3.91	222+2222+	0.89	T	5.27	2222++20	0.79	T
4.28	222+2222-	0.84	S	5.38	2+2222+0	0.87	T
4.62	222222++2	0.64	T	5.47	+22222+0	0.83	T
4.86	222222++2	0.62	T	5.56	+22222-0	0.67	S
4.93	222222022	0.83	S	5.69	2+2222-0	0.72	S
5.03	2+222222+	0.91	T	5.81	22220220	0.77	S
5.27	2+222222-	0.73	S	5.92	222++220	0.95	T
5.31	222222+-2	0.74	S	6.02	2222+-20	0.59	S
5.31	22222++22	0.80	T	6.12	222+2+20	0.80	T
5.43	22222+-22	0.74	S	6.27	22222020	0.77	S
5.57	22222+2+2	0.87	T	6.79	22+2+220	0.90	T
5.59	+2222222+	0.86	T	6.83	22222+0+	1.00	T
5.70	2222+22-2	0.68	S	6.88	22+22+20	0.72	T
5.76	222222202	0.74	S	7.03	222+2-20	0.58	S
5.84	22+22222-	0.54	S	7.17	22+2-220	0.80	S
6.15	222220222	0.81	S	7.60	22++2220	0.81	T
6.30	2222+22+2	0.98	T	7.71	222+-220	0.76	S
6.39	2222+2+22	0.64	T	7.81	22+2220-	0.67	S
6.97	222+22+22	0.63	T	8.37	2222+-++	0.80	T

Table 5.1: Energies, configurations, maximal coefficients and spins ('S' for singlet and 'T' for triplet) for dicationic states of 1,3-Cyclohexadiene (C_6H_8) and 1,3-butadiene (C_4H_6). The configuration corresponding to the maximum coefficient in the expansion is given. The occupation of orbitals in the active space is shown. 2 implies doubly occupied orbital, while a + and - implies one electron with spin up or down, respectively. The first row is the ground state of the dication.

C_6H_{12}				C_5H_{10}			
Energy[eV]	Conf.	Coef.	Spin	Energy[eV]	Conf.	Coef.	Spin
0.00	2222222++	0.95	T	0.00	2222222++	0.96	T
0.21	222222220	0.78	S	0.48	222222+2+	0.84	T
0.38	2222222+-	0.87	S	0.49	222222220	0.67	S
0.48	222222202	0.63	S	0.52	222222+2-	0.84	S
0.53	222222+2+	0.90	T	0.56	2222222+-	0.72	S
0.59	222222++2	0.91	T	0.58	2222+222+	0.57	T
0.59	222222+2-	0.85	S	0.64	222+2222-	0.58	S
0.85	2222+222+	0.70	T	0.77	222+2222+	0.53	T
0.85	222222+-2	0.66	S	0.86	22222+2-2	0.78	S
1.09	22222+22+	0.77	T	1.00	22222++22	0.58	T
1.13	222222022	0.75	S	1.09	222+2222+	0.58	T
1.13	2222+22+2	0.63	T	1.26	22222++22	0.52	T
1.15	2222+222+	0.51	T	1.30	2222+22+2	0.53	T
1.24	2222+222-	0.82	S	1.32	22222+-22	0.37	S
1.27	22222+22-	0.90	S	1.33	222222++2	0.54	T
1.33	22222+2-2	0.81	S	1.36	22222+-22	0.57	S
1.33	2222+2+22	0.90	T	1.43	222222022	0.41	S
1.44	22222++22	0.83	T	1.44	2222+2+22	0.58	T
1.51	2222+22-2	0.83	S	1.45	22222+-22	0.53	S
1.70	2+222222+	0.79	T	1.54	2222++222	0.85	T
1.72	222+2222+	0.81	T	1.59	2222+2+22	0.50	T
1.84	222+222+2	0.83	T	1.62	222+2-222	0.56	S
2.17	22+22222+	0.74	T	1.66	22222+22-	0.57	S
2.20	222+2222-	0.65	S	1.79	222+22+22	0.46	T
2.65	2222+-222	0.83	S	1.89	222++2222	0.70	T
2.78	2222++222	0.77	T	1.89	222222+-2	0.57	S
3.12	+2222222-	0.62	S	2.24	222+-2222	0.70	S
3.32	222+-2222	0.67	S	2.25	222022222	0.56	S

Table 5.2: Energies, configurations, maximal coefficients and spins (‘S’ for singlet and ‘T’ for triplet) for dicationic states of cyclohexane (C_6H_{12}) and cyclopentane (C_5H_{10}).The configuration corresponding to the maximum coefficient in the expansion is given. The occupation of orbitals in the active space is shown. 2 implies doubly occupied orbital, while a + and - implies one electron with spin up or down, respectively. The first row is the ground state of the dication.

Chapter 6

Conclusion and Prospects

This thesis covered two topics in molecular strong field ionization (SFI): post-ionization dynamics in single ionization (SI) and enhanced double ionization (DI) yield in conjugated molecular systems.

For the former, we developed a coincidence velocity map imaging (VMI) detector and measured the photoelectron spectra in coincidence with photoions. With the help of *ab initio* electron structure calculations and our own simulation results, we were able to assign peaks in the photonelectron spectra to the appropriate ionic states. There we showed the direct removal of inner orbital electrons and distinguished two ionization pathways – direct and indirect ionization. A survey on a series of molecules suggested the dependence of fragmentation and indirect ionization yield on gap energy, which was the energy difference between dissociative and non-dissociative ionic states. We then studied in detail the mechanism underlying indirect ionization and confirmed the importance of resonances. We also found that with an intense field, the non-adiabaticity due to varying field coupling can lead to significant population transfer among ionic states.

For the DI experiments, we found a surprising high yield of DI at relatively low intensities with 10 fs pulses. This suggested the DI we observed is not sequential ionization or the typical enhancement due to nuclear motion. The ellipticity dependence further suggested that this enhancement is unlikely due to field-driven re-scattering. The comparison among 4 different molecules indicated a connection between the enhanced DI yield and the electronic structure. We also showed some testing results of a novel fast camera that had both spatial and temporal resolution, which made it particularly suitable for DI experiments.

For the next step, we would like to better understand how the enhanced DI is related electronic structure. So far, we've observed this enhancement in conjugated molecules with two double bonds, but not in molecules with only single bonds. There are two conjectures on what enhances the DI: (1) the conjugated molecular bond structure; or (2) the low density of states in the dication, which *happens to* be present in the conjugated molecules we've tested. To test this, we need to look at conjugated molecules with different spectra. For instance, increasing the number of double bonds leads to an increased number of low energy orbitals, and hence a high density of ionic states. If enhanced DI is still observed then the double bonds are likely to be the contributing factor. If, however, DI is suppressed then the density of electronic states is likely more important. In addition, with the TimepixCam being successfully integrated into our coincidence VMI detector, we can start measuring electron-electron correlations in DI, which could offer important insight on the underlying mechanism of strong field molecule DI.

Appendix A

Additional Photoelectron Spectra

$D_i^{(j)}$ denotes the i^{th} ionic state at the j^{th} photon order, with $i = 0$ corresponding to the ground state. CH_2IBr, C_6H_5I and CF_3I all contribute two data points each in the ratio figures. When the relevant peaks overlap, we try to fit multiple Gaussians to them to have a better discrimination. However, a comparison between integrating over a Gaussian fit and a straight-cut region in the case of CH_2IBr shows little discrepancy in the resultant ratios, that is, it doesn't affect the trend observed in the ratio plots. So we only carry out a Gaussian fit when it's necessary. For Figure A.4 and A.5, the spectra in coincidence with the fragments are rather flat and have very low yields, which is something we don't quite understand yet. In these cases, the assignment of the ionic states and the choice of the integration regions are based on both the ionic state energies and the comparison with the spectra in coincidence with the parent. More specifically, in Figure A.4 and A.5, the light green and dark blue regions of the spectra in coincidence with the fragment ions have similar yields while the spectra in coincidence with the parent ions vary by a lot. Hence we believe the green regions are direct ionization to dissociative states.

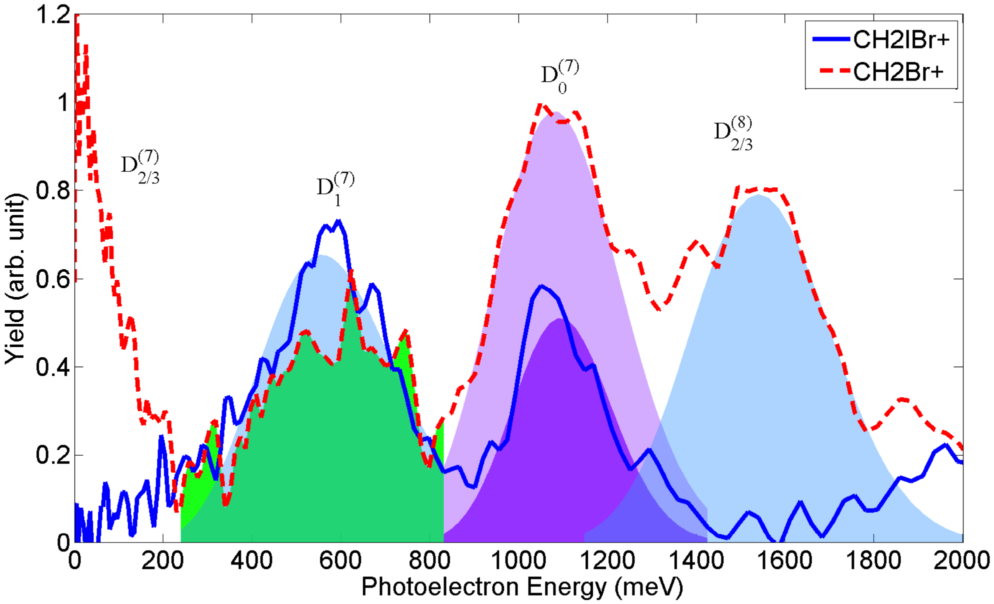

Figure A.1: Photoelectron spectrum of CH_2IBr.
A multi-Gaussian fit is carried out and the ratio calculations are based on the shaded areas indicated in the figure because there are significant overlaps between the peaks in the photoelectron spectrum.
We note that in an earlier study of the molecule CH_2IBr [2], we found negligible indirect ionization yield to D_2/D_3 at low laser intensity based on an indirect pump-probe analysis and theoretical calculations. We feel that our current results, which find significant indirect ionization to D_2/D_3, provide an improved measurement since the photoelectron spectrum gives a more direct indication of the state resolved ionization yields.

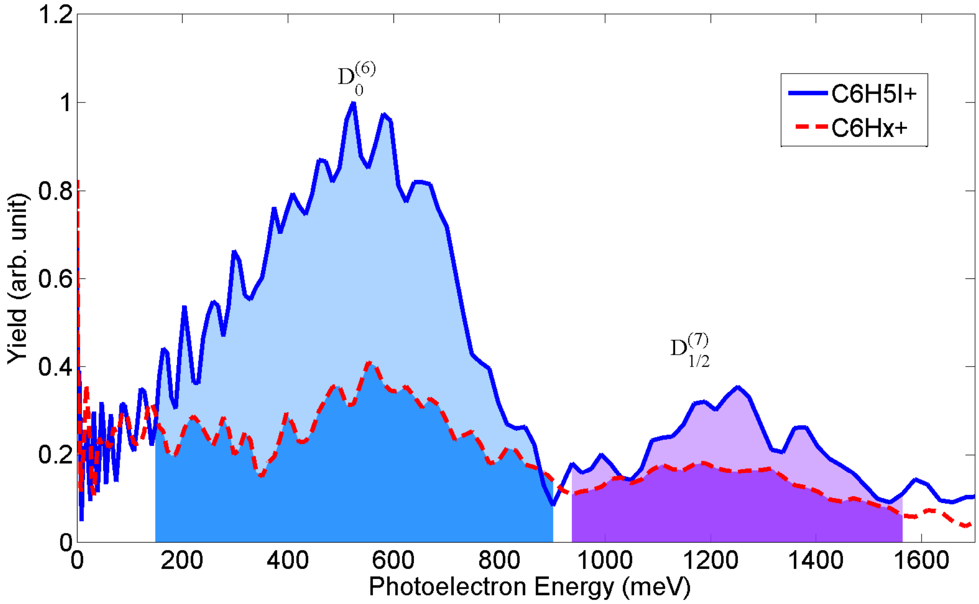

Figure A.2: Photoelectron spectrum of C_6H_5I.
No direct ionization to dissociative states is observed.

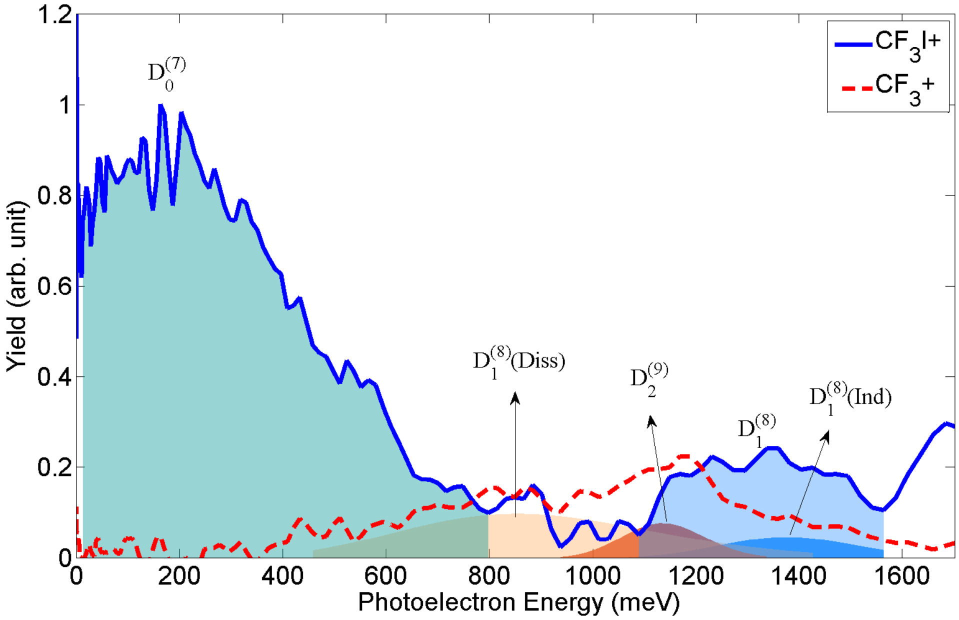

Figure A.3: Photoelectron spectrum of CF_3I.

Although state D_1 itself is non-dissociative, it is possible to ionise the molecule to a vibrationally excited D_1 which may dissociate due the extra energy available from vibrational degrees of freedom. We label this feature as $D_1^{(8)}$(Diss). This is also observed in [110]. It is also worth noting that there is no post-ionization excitation from the state D_0, in contrast to all other molecules. We believe this is due to a negligible coupling strength and a large energy gap between D_0 and excited ionic states. A Gaussian fit is applied to discriminate various features in the spectra. First, we fit a Gaussian curve to $D_1^{(8)}$(Ind), shaded in dark blue, such that its shape resemble that of $D_1^{(8)}$, shaded in light blue, and it's below the red spectrum. Then we subtract this Gaussian from the red spectrum and fit the resultant spectrum with two Gaussian curves, which are labelled $D_1^{(8)}$(Diss) and $D_2^{(9)}$. The assignment of these peaks are base on the ionic state energies and the discussion in [110].

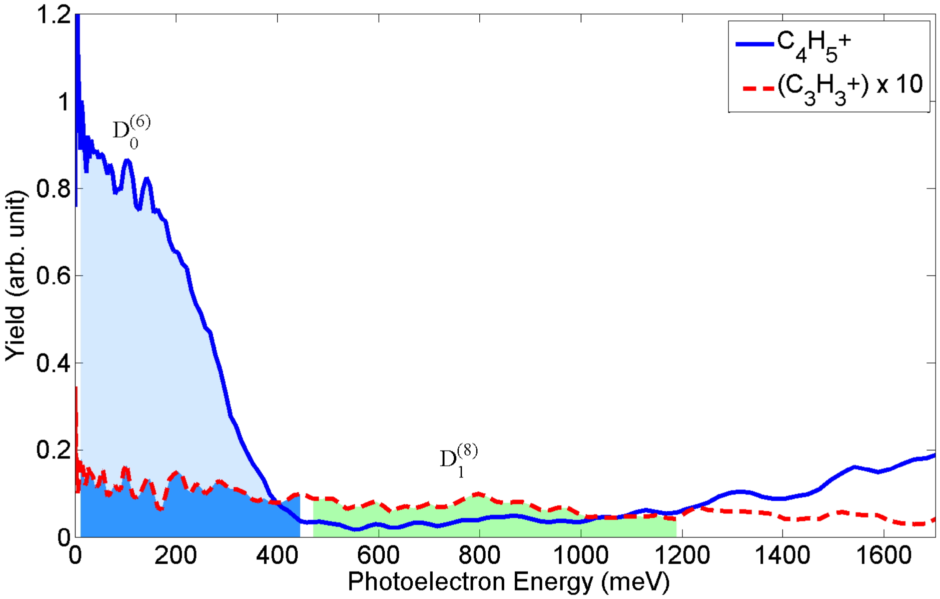

Figure A.4: Photoelectron spectrum of C_4H_6.
The spectrum in coincidence with the fragment ion is multiplied by 10 for better viewing.

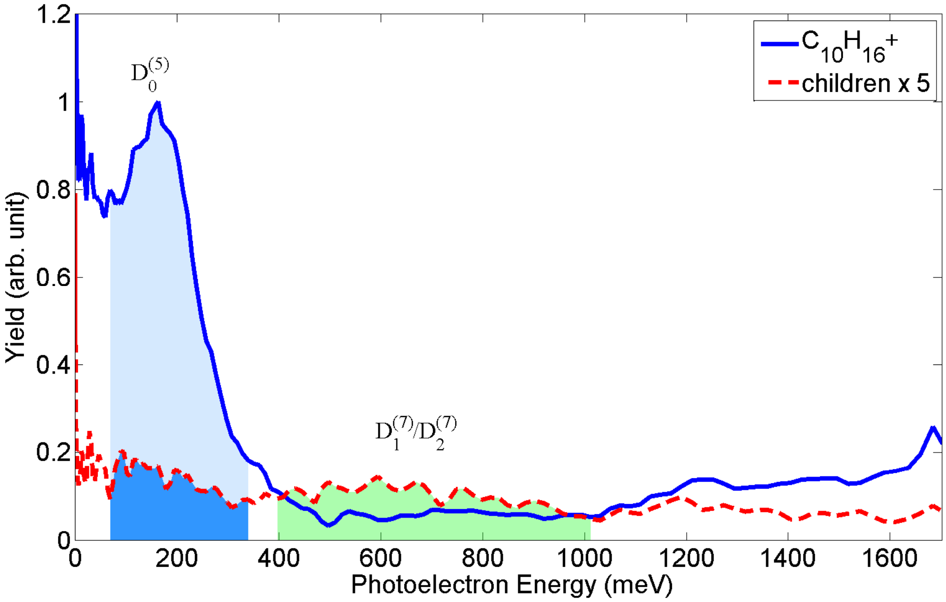

Figure A.5: Photoelectron spectrum of $C_{10}H_{16}$.
The spectrum in coincidence with the fragment ions is multiplied by 5 for better viewing.

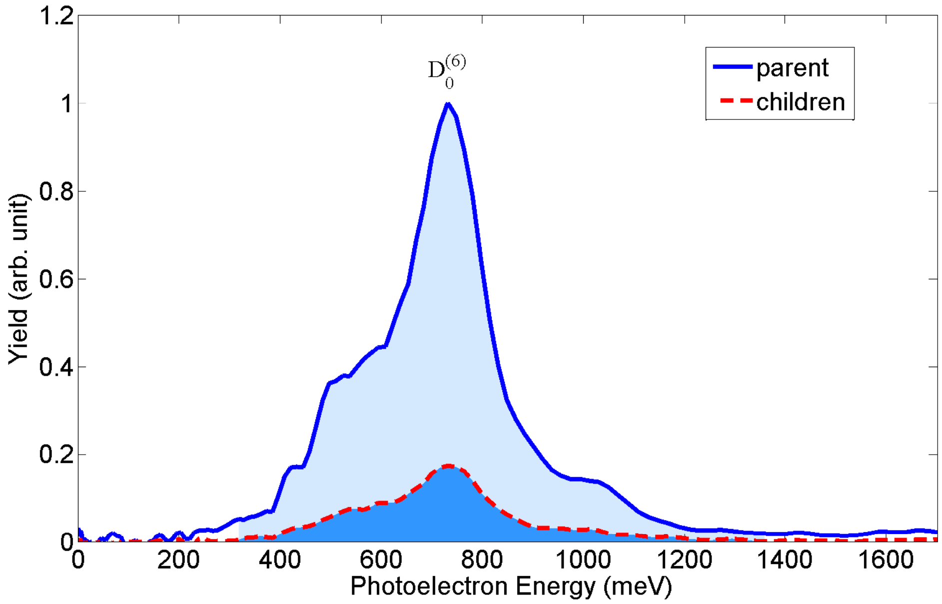

Figure A.6: Photoelectron spectrum of C_6H_8.
No direct ionization to dissociative states is observed.

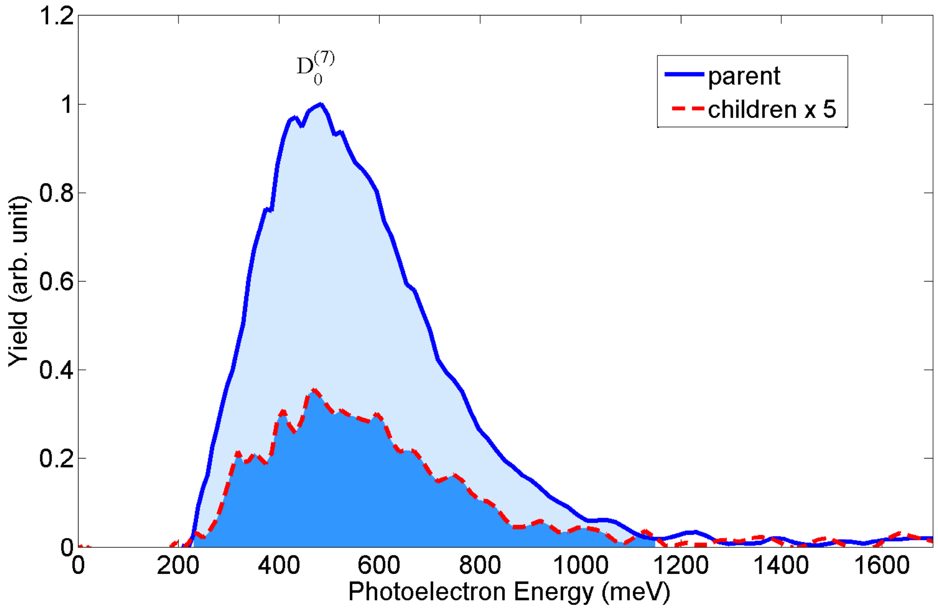

Figure A.7: Photoelectron spectrum of CS_2.
No direct ionization to dissociative states is observed. The spectrum in coincidence with the fragment ions is multiplied by 5 for better viewing.

Appendix B

Coincidence Rates and False Coincidences

Here we provide a detailed assessment of true vs false coincidence rates given the finite detection efficiency of our detector. For single ionization VMI coincidence experiment, ideally, we should detect exactly one electron and one ion, which originate from the same molecule. However, due to limited (< 1) detection efficiency, it is possible that two particles measured in coincidence indeed come from different molecules. We distinguish two cases:

(1) *Valid coincidence*: this includes *true coincidence* - the electron and ion come from the same molecule, and *cross coincidence* the electron and ion come from two different molecules which, however, result in the same ionic state. A *cross coincidence* is a valid data point because the underlying physics is the same.

(2) *False coincidence*: the electron and ion come from two separate molecules which end up in different ionic states. This effects our interpretation of the measurement, hence a false event.

To calculate the occurrence of each case and compare them, we assume the ionization rate follows a Poisson distribution $\frac{\lambda^k e^{-\lambda}}{k!}$, with λ being the expected ionization occurrence per laser shot (≈ 0.5 in our experiment). Most of our measurements show one dominant fragment ion production along with the parent ion. In light of this and to simplify the derivation, we denote by b_p and b_c the branching ratios of the parent and fragment ion, respectively, with $b_p + b_c = 1$. We also denote by η_p and η_c the detection efficiencies for the parent and fragment ion, respectively, and by η_e the detection efficiency for photoelectrons.

Probability of Valid Coincidence

$$\begin{aligned} & V(\lambda, b_p, \eta_p, \eta_c, \eta_e) \\ = \quad & \sum_{k=1}^{\infty} \frac{\lambda^k e^{-\lambda}}{k!} \sum_{j=1}^{k} \binom{k}{j} b_p^j (1-b_p)^{k-j} (1-(1-\eta_p)^j)(1-\eta_c)^{k-j} j \eta_e (1-\eta_e)^{k-1} \\ = \quad & e^{-\lambda} \lambda b_p \eta_e [e^{\lambda(1-\eta_e)(1-\eta_c+b_p\eta_c)} - (1-\eta_p) e^{\lambda(1-\eta_e)(1-\eta_c+b_p\eta_c-b_p\eta_p)}] \qquad \text{(B.1)} \end{aligned}$$

This result can be readily generalized for multiple fragment ion species with various branching ratios and detection efficiencies. However, this is much more complex and not necessary. To deal with multiple species, it's easier to treat them as two species first - the spectrum of one species and the collection of the spectra of the rest. The detection efficiency can be renormalized using the branching ratio, ie, a weighted average. Then one can iterate the procedure on the collection of the species, if necessary.

Probability of False Coincidence

Now we consider the case that the detected ion-electron pair come from two molecules which produce different ion fragments. The probability of false coincidence in the parent due to the fragment (i.e. the electron comes from a molecule that fragments, but is measured in coincidence with a parent ion from a different molecule) is given by:

$$\begin{aligned} & F(\lambda, b_p, \eta_p, \eta_c, \eta_e) \\ = \quad & \sum_{k=1}^{\infty} \frac{\lambda^k e^{-\lambda}}{k!} \sum_{j=1}^{k} \binom{k}{j} b_p^j (1-b_p)^{k-j} (1-(1-\eta_p)^j)(1-\eta_c)^{k-j} (k-j) \eta_e (1-\eta_e)^{k-1} \\ = \quad & e^{-\lambda} \eta_e \lambda (1-b_p)(1-\eta_c)[e^{\lambda(1-\eta_c+b_p\eta_c)} - e^{\lambda(1-\eta_c+b_p\eta_c-b_p\eta_p)}] \qquad \text{(B.2)} \end{aligned}$$

Given the detection efficiencies and the expected ionization rate, one can calculate the fraction of the coincidence detected that is valid. As a simple example, let's assume there is only one kind of ion with detection efficiency $\eta_i = 0.25$, and that the electron detection efficiency is $\eta_e = 0.5$. Then $\lambda \approx 0.5$ implies that 83% of our data is valid coincidence. In fact, it's possible to make correction to the photoelectron spectra as we will discuss now.

Correction to Systematic Error

False coincidences introduce a systematic error in the photoelectron spectrum. Here we try to make a first-order correction. We write the spectra as follows:

$$\begin{cases} m_p(E) = V_p(\lambda, b_p)p(E) + F_p(\lambda, b_p, b_c)c(E) \\ m_c(E) = V_c(\lambda, b_c)c(E) + F_c(\lambda, b_c, b_p)p(E) \end{cases} \tag{B.3}$$

where $m_p(E), m_c(E)$ are the measured photoelectron spectra for the parent and fragment ions, respectively, E denotes the photoelectron energy, and $p(E), c(E)$ are the real photoelectron spectra for the parent and fragment, respectively. Both are normalized such that $\int p(E)dE = \int c(E)dE = 1$. V_p, V_c are the probabilities of a valid coincidence for the parent and fragment, respectively. F_p, F_c are the probabilities of false coincidence for the parent and fragment, respectively. b_p is calculated from the measured spectra:

$$b_p = \frac{\int m_p dE}{\int (m_p + m_c)dE}, \qquad b_c = 1 - b_p \tag{B.4}$$

Solving the system of equations B.3 above, we get

$$p(E) = \frac{m_p V_c - m_c F_p}{V_p V_c - F_p F_c} \qquad c(E) = \frac{m_c V_p - m_p F_c}{V_c V_p - F_c F_p} \tag{B.5}$$

This is not the complete correction since b_p is obtained from the measured spectra, not the real ones. Taking into account the branching ratios, the final photoelectron spectra are : $p(E)b_p$ and $c(E)b_c$. One can iterate this process by re-calculating b_p using the resultant spectra to get a better correction.

Numerical Results

Here we give the numerical values for $\frac{V_p}{V_p+F_p}$ and $\frac{V_c}{V_c+F_c}$, i.e., the fraction of valid coincidences, for all molecules presented in Sec.3.3. The first number in the table is obtained from B.1 and B.2 while the second number is obtained from a separate Monte Carlo simulation. The two approaches yield consistent results.

Table B.1: Fraction of valid coincidences

Species	CS_2	C_6H_8	$C_{10}H_{16}$	C_4H_6	C_6H_5I	CF_3I	CH_2BrCl	CH_2IBr
$\frac{V_p}{V_p+F_p}$	0.99 0.99	0.98 0.98	0.99 0.99	0.99 0.99	0.93 0.94	0.95 0.96	0.89 0.87	0.89 0.89
$\frac{V_c}{V_c+F_c}$	0.86 0.89	0.87 0.88	0.85 0.87	0.87 0.89	0.91 0.92	0.89 0.90	0.96 0.96	0.97 0.98

Determining λ in Experiments

As mentioned earlier, in a coincidence experiment, the average ionization rate should be kept at less than one ionization per laser shot. This is achieved experimentally by adjusting the sample pressure such that $N(0 < N \leq 1)$ fraction of the TOF traces contain *at least* an electron peak. We use "*at least*" because it's difficult to quantize the number of electrons detected in the TOFMS. The fraction N is determined from the expected ionization rate λ as follows:

$$\begin{aligned} N(\lambda) &= 1-\sum_{k=0}^{\infty}\frac{\lambda^k e^{-\lambda}}{k!}(1-\eta_e)^k \\ &= 1-e^{-\lambda\eta_e} \qquad \text{(B.6)} \\ & \qquad \text{(B.7)} \end{aligned}$$

Given the electron detection efficiency and the target λ value, this gives us a quantity that can be easily measured experimentally – simply counting how ofter the TOF trace shows an electron peak. For instance, for $\lambda = 0.5$ and $\eta_e = 0.5$, $N(\lambda) = 0.221$, which means we should adjust the sample pressure such that we see electron peaks in $\sim$ 220 TOF trace per second (1 kHz laser rep rate).

Appendix C

Simulation and Analysis Codes

Here we document three important program codes used in the experiments. The algorithms in the first two simulation codes are similar. Both codes solve the TDSE, one estimating the AC Stark shift in SFI for the purpose of peak assignment in Sec. 3.1, while the other one calculating the non-adiabatic transition among ionic states in Sec.4.3 and Sec.4.4. The last code is used to perform the Abel inversion, discussed in Sec. 2.5. We provide the core parts of each code. The complete versions, which contain more features, can be found on the group site.

Dynamic Stark Shift

In order to estimate the AC Stark shift of each ionic state, E_S^i (see Eq. 1.2), we perform a numerical integration of the TDSE including the molecular ground state and the five lowest ionic states of the CH_2BrCl molecule. A numerical approach is necessary because given the various detunings between the low lying ionic states and the laser, neither the rotating wave approximation (RWA) or adiabatic elimination is valid. The RWA requires the detunings to be much smaller than the laser frequency and adiabatic elimination requires that the detunings be larger compared to the Rabi frequency. To model the real laser field used in the experiment, which are responsible for both the Stark shift and multiphoton ionization, we define two fields in the calculation: a strong IR laser field inducing the Stark shift and a weak VUV field ionizing the ground state. The idea is to 'probe' the ionic states' Stark shifts by looking for population transfer from the ground state as a function of VUV laser frequency. The transition dipole moments (TDMs) between ionic states, state energies and spin-orbit couplings for the ions are borrowed from the *ab initio* electronic structure calculations perform by Tamás Rozgonyi [1]. The TDMs between the neutral and ionic states are chosen to be 0.1 a.u. which allows for VUV coupling but doesn't deplete the ground state. Only five ionic states are considered because there is a substantial energy gap to the next lowest ionic states.

The total electronic Hamiltonian (nuclear dynamics is not considered here) consists of 3 parts, the bare Hamiltonian H_0 (not including spin-orbit coupling), spin-orbit coupling H_{SO}, and the molecule-field dipole-coupling H_{MF}:

$$\begin{aligned} H &= H_0 + H_{SO} + H_{MF} && \text{(C.1)} \\ H_{MF} &= -\vec{\mu}\cdot\vec{E} && \text{(C.2)} \\ (H_0 + H_{SO})\,|\phi_i\rangle &= \hbar\omega_i\,|\phi_i\rangle && \text{(C.3)} \end{aligned}$$

where $E = E_{IR} + E_{VUV}$ is the laser field.

$$\begin{aligned} E_{IR} &= \mathcal{E}_{IR}(t)\frac{(e^{i\omega_{IR}t} + c.c.)}{2} && \text{(C.4)} \\ E_{VUV} &= \mathcal{E}_{VUV}(t)\frac{(e^{i\omega_{VUV}t} + c.c.)}{2} && \text{(C.5)} \end{aligned}$$

$\mathcal{E}(t) = \mathcal{E}e^{-\frac{t^2}{2T^2}}$ is a Gaussian temporal envelope with intensity FWHM $= 2\sqrt{ln2}\ T$, which is set to 30 fs in the this case. The calculation is carried out in the eigenspace of $H_0 + H_{SO}$ (i.e. in the spin-orbit basis). The wave function is written in terms of the eigenstates:

$$|\psi(t)\rangle = \tilde{a_0}(t)\,|\phi_0\rangle + \sum_{i\neq 0}\tilde{a_i}(t)\,|\phi_i\rangle \qquad \text{(C.6)}$$

Substituting (C.9) and (C.6) into the TDSE $i\hbar\frac{\partial}{\partial t}\,|\psi\rangle = H\,|\psi\rangle$ and transforming to the rotating frame $\tilde{a}_i(t) = a_i(t)e^{-i\omega_i t}$, we arrive at :

---

[1] Institute of Materials and Environmental Chemistry, Research Centre for Natural Sciences, Hungarian Academy of Sciences, Budapest 1117, Magyar tudósok körútja 2, Hungary

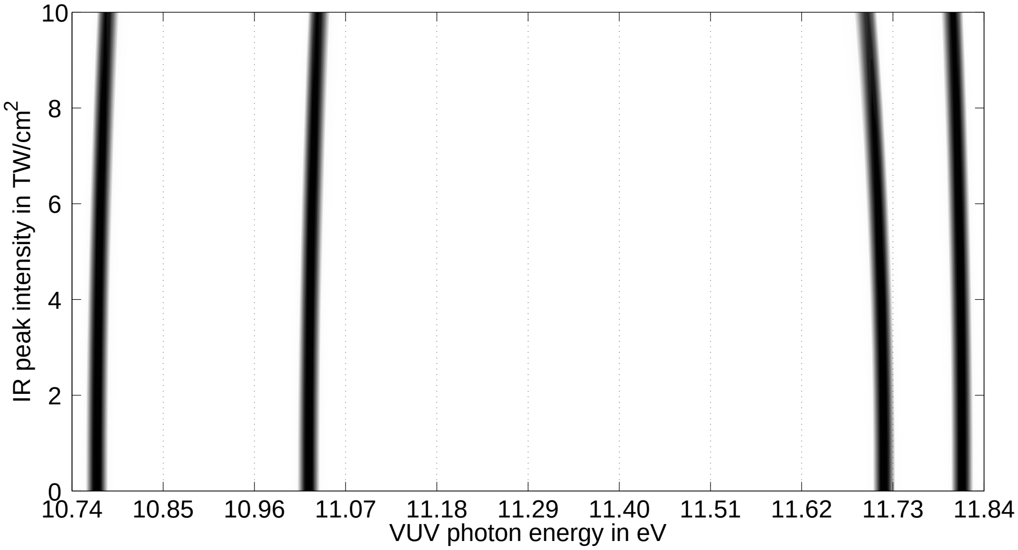

Figure C.1: Calculations aimed at estimating dynamic Stark shifts for ionic states of CH_2BrCl in a strong field IR laser pulse. The graph shows population of the first five ionic states as a function of IR field strength and VUV photon energy. On the horizontal axis the frequency of the VUV radiation is plotted, while on the vertical, it is the peak intensity of the IR pulse.

$$\dot{a}_0(t) = \frac{i}{\hbar}\sum_{i\neq 0}\mu_{0i}[\mathcal{E}_{VUV}(t)e^{i\omega_{VUV}t} + \mathcal{E}_{IR}(t)(e^{-i\omega_{IR}t} + e^{i\omega_{IR}t})]a_i(t)e^{-i\omega_{i0}t} \tag{C.7}$$

$$\begin{aligned}\dot{a}_{i\neq 0} = {} & \frac{i}{\hbar}\mu_{i0}[\mathcal{E}_{VUV}(t)e^{-i\omega_{VUV}t} + \mathcal{E}_{IR}(t)(e^{-i\omega_{IR}t} + e^{i\omega_{IR}t})]a_0(t)e^{-i\omega_{0i}t} \\ & + \frac{i}{\hbar}\sum_{j\neq i}\mu_{ij}\mathcal{E}_{IR}(t)(e^{-i\omega_{IR}t} + e^{i\omega_{IR}t})a_j(t)e^{-i\omega_{ji}t}\end{aligned} \tag{C.8}$$

We have omitted the rapidly rotating terms, $\mathcal{E}(t)e^{\pm i(\omega_{VUV}+\omega_{io})t}$, for $\omega_{VUV}+\omega_{io} >> |\omega_{VUV}-\omega_{io}|$, invoking the rotating wave approximation only for the VUV field, but not for the IR. By calculating the ionic states' population as a function of IR field strength and VUV photon energy, we can map out the Stark shift of each ionic state as a function of IR field strength, as shown in Fig.C.1.The two-dimensional plot shows the total ionic population for a range of VUV photon energies (horizontal axis) and IR peak intensities (vertical axis). The calculation shows that population can be transferred to the lowest four ionic states when the VUV pulse is resonant with the energy difference between the neutral ground state and each of the ionic states. As the IR field strength increases, it couples the ionic states, leading to dynamic Stark shifts, as seen in shifts of the absorption peaks on the graph. We note that simulations were performed with the IR electric field polarized along the C-Br bond. It is along this direction that the molecule-field coupling is the largest. Nevertheless, the shifts of the absorption peaks stay below 100 meV for the intensities used in the measurements. Similar calculations for CH_2IBr show similar amount of Stark shift. Since the other terms in Eq. 1.2 are significantly larger, we argue that neglecting E_S is a good approximation for the purpose of peak assignment.

Non-adiabatic Transition

This is similar to the model in the previous section but we drop the ionization part of the coupling (no E_{VUV}) as well as the ground ionic state, and focus on how the IR field couples the ionic states. The total electronic Hamiltonian consists of the free Hamiltonian H_0 and the molecule-field dipole-coupling H_{MF}:

$$\begin{aligned} H &= H_0 + H_{SO} + H_{MF} && \text{(C.9)} \\ H_{MF} &= -\vec{\mu} \cdot \vec{E} && \text{(C.10)} \\ H_0 \left|\phi_i\right\rangle &= \hbar\omega_i \left|\phi_i\right\rangle && \text{(C.11)} \\ \left|\psi(t)\right\rangle &= \sum_i \tilde{a}_i(t) \left|\phi_i\right\rangle && \text{(C.12)} \end{aligned}$$

Solving the TDSE:

$$\begin{aligned} \dot{a}_i &= \frac{i}{\hbar} \sum_{j \neq i} \mu_{ij} 2\mathcal{E}_{IR}(t) cos(\omega_{IR} t) a_j(t) e^{-i\omega_{ji} t} && \text{(C.13)} \\ \omega_{ij} &= \omega_i - \omega_j \end{aligned}$$

Since there is no ionization, the initial condition is manually set. One can choose to solve the TDSE in either the adiabatic or diabatic basis. If one is only interested in the population at the end of the pulse, such as in

Fig. 4.4, then it's easier to work in the diabatic basis since the adiabatic basis requires diagonalization at each time step. The diabatic formulation is that of Eq. C.13. However, all the population should start in the adiabatic ground ionic state, $\tilde{a_1}'(0)$. Consider a 2-level system. Let $U(t)$ be the unitary transformation that diagonalizes the instantaneous Hamiltonian $H(t)$:

$$U^{-1}(t)H(t)U(t) = D(t) \tag{C.14}$$

$$D(t) = \begin{pmatrix} E'_a & 0 \\ 0 & E'_b \end{pmatrix} \tag{C.15}$$

$$\tilde{\psi}' = U^{-1}\tilde{\psi} = \begin{pmatrix} \tilde{a}'(t) \\ \tilde{b}'(t) \end{pmatrix} \tag{C.16}$$

Then the initial amplitudes of the diabatic states are given by $U(0)\psi'(0)$. On the other hand, if one is interested in following the population dynamics, such as in Fig. 4.5, then both bases require roughly the same amount of calculation, because the states' amplitudes obtained in the diabatic basis need to be transformed into the adiabatic basis at each time step.

Here we include the core of the code implemented in MATLAB (R2014b)

```
function [w, mu, t, yE, Pop, Pop_c, U, H_ad] = IwPE

%% load potentials, TDMs. Set field amplitudes, carrier
    frequencies, pulse duration

global w mu EX EIR omegaX omegaIR tIR tX NStates a0
% w - potentials
% mu - TDMs
% EX and EIR - VUV and IR amplitude
% omegaX and omegaIR - VUV and IR frequency
% tX and tIR - characteristic time pulse durations,
    depending on the envelope shape
% exp(-1*(t.^2)/2/tX^2) --> FWHM_field=2*sqrt(2*log(2))
    *tX=2.35482*tX, FWHM_int=2sqrt(ln2)tX=1.6651*tX [ps
    ];
```

```
% (cos(pi*t/tX))^2.*(t>-tX/2 & t<tX/2) -->FWHM_field=0.5*tX,FWHM_int=2*acos(0.5^0.25)/pi*tX=0.364*tX [ps]

% main simulation

H_di0 =  w*hbar-EIR*mu; % diabatic Hamiltonian
[U0, H_ad0] = eig(H_di0); %diagonalization

%initialize eigenstate amplitudes
% NState - number of states, including neutrals
c0 = zeros(NStates,1);  %adiabatic states at t=0
a0 = zeros(NStates,1);  %diabatic states at t=0
c0(1) = 1; % all population starts in the ground state
a0 = U0*c0; % diabatic states amplitude

[t,a] = SolveTDSE_IwPE(); %solve TDSE with Matlab ode solver

%transfer to schroedinger picture from interaction pic
aTilde = zeros(size(a));
for j=1:size(a,2);
        aTilde(:,j) = a(:,j).*exp(-1i*w(j,j)*t);
end

Pop = abs(aTilde).^2;    % diabatic population

yE = EIR*exp(-1*(t.^2)/2/tIR^2).*cos(omegaIR*t) + EX*exp(-1*(t.^2)/2/tX^2).*cos(omegaX*t); %field
for j =1:length(yE)
        H_di(:,:,j) = w*hbar-yE(j)*mu; % diabatic Hamiltonian at all times
        [U(:,:,j), H_ad(:,:,j)]=eig(H_di(:,:,j)); % Transformation matrix U at all times
        c(:,j) = U(:,:,j)\aTilde(j,:).'; % transforming to adiabitic basis, note to use .' instead of '
end
```

```
Pop_c = (abs(c).^2).'; adiabatic population

function [t,a] = SolveTDSE_IwPE()
        global  tIR tX NStates w mu a0
        options = odeset('RelTol',1e-6,'AbsTol',1e-7);
           % ode solving accuracy
        [t,a] = ode23(@TDSE_IwPE,[-4*tIR, 4*tIR],a0,
           options); % set solver, time interval,
           initial condition.
end

function da = TDSE_IwPE(t, a)
global hbar w mu EX EIR omegaX omegaIR tIR tX Basis
   NStates

% construct the matrix in Eq. (C.7) and (C.8)

MU = zeros(NStates);
for j=1:NStates % matrix in Eq. (C.7)
%      Gaussian envelope
MU(1,j) = 1/2/hbar*mu(1,j)*(EX*exp(-1*(t.^2)/2/tX^2)*
   exp(+1i*omegaX*t)+EIR*exp(-1*(t.^2)/2/tIR^2)*2*cos(
   omegaIR*t))*exp(-1i*(w(j,j)-w(1,1))*t);
MU(j,1) = 1/2/hbar*mu(j,1)*(EX*exp(-1*(t.^2)/2/tX^2)*
   exp(-1i*omegaX*t)+EIR*exp(-1*(t.^2)/2/tIR^2)*2*cos(
   omegaIR*t))*exp(-1i*(w(1,1)-w(j,j))*t);

end

% two cases for Eq. (C.8)
% (1) with spin-orbit coupling Hamiltonian
for k=2:NStates
for j =2:NStates
if j~=k
% Gaussian
MU(k,j) = 1/hbar*mu(k,j)*EIR*exp(-1*(t.^2)/2/tIR^2)*cos
   (omegaIR*t)*exp(-1i*(w(j,j)-w(k,k))*t) - w(k,j)*exp
   (-1i*(w(j,j)-w(k,k))*t);
```

```
end
end
end

(2) no spin−orbit coupling Hamiltonian
for k=2:NStates
for j =2:NStates
if j~=k
% Gaussian
MU(k,j) = 1/hbar*mu(k,j)*EIR*exp(−1*(t.^2)/2/tIR^2)*cos
    (omegaIR*t)*exp(−1i*(w(j,j)−w(k,k))*t);
end
end
end

end

da = 1i*MU*a; % this is Eq. (C.7) and (C.8)
```

Abel Inversion

The algorithm has been described in detail in Sec.2.5. Here we provide the core part of the Matlab code. The code automatically determines the size of the image and construct the inversion matrix. That construction part only need to run once. So to process large number of images, that part can be set outside the function. Additional options include using a lattice center instead of a pixel center and processing coordinates instead of images. These can be found in the full version of the code here

---

```
%input an image and its center
%output the 3D distribution in panel (a) Fig.2.8,
    variable Ring, and the 2D distribution after
    integration over the axis of symmetry in panel (c)
    Fig.2.8, variable AngIntegrated.
```

```
function [Ring, AngIntegrated] = Inv_Abel_Linear(Centre
    , Image)

%round center to integer
CentralRow = Centre(1);
CentralColoum = Centre(2);
yc = round(CentralRow);
xc = round(CentralColoum);

%check image size to prepare the inversion matrix, and
    fold images to one quadrant

ImageOrig = Image;
DimOrig = size(Image);
RadiusMax = min(yc-1, DimOrig(1)-yc);    % max y < Dim/2
XRange = min(xc-1,DimOrig(2)-xc);    %< max y, cut edge

for x=1:XRange %quadrant size used
for y = 1:RadiusMax
Image(yc+y,xc+x) = (Image(yc+y,xc+x)+Image(yc-y,xc+x)+
    Image(yc+y,xc-x)+Image(yc-y,xc-x))/4;   Image(yc,xc+x
    ) = (Image(yc,xc+x)+Image(yc,xc-x))/2;
Image(yc+y,xc) = (Image(yc+y,xc)+Image(yc-y,xc))/2;
end

%first calculate the projection matrix, then invert it
for NumRing = 1:Size
Distr(NumRing).Area = zeros(NumRing,NumRing); %
    projection matrix
Distr(NumRing).Weight = zeros(NumRing,NumRing); %
    inversion matrix
for y = 1:NumRing
Sum = 0;
for k = y:NumRing
Distr(NumRing).Area(y,k) = (k-.5)^2*(acos((y-1.5)/(k
    -.5))-acos((y-.5)/(k-.5)))+(y-.5)*((k-.5)^2-(y-.5)
    ^2)^.5-(y-1.5)*((k-.5)^2-(y-1.5)^2)^.5-Sum;
Sum = Sum + Distr(NumRing).Area(y,k);
```

```
end
end
Distr(NumRing).Weight = inv(Distr(NumRing).Area);
end

Ring = zeros(DimOrig(1),DimOrig(2));
AngIntegrated = zeros(DimOrig(1),DimOrig(2));

%inversion
for x = 0:XRange %x and y are distance here
NumRing = RadiusMax - 1;

Ring(yc:(yc+NumRing-1),x+xc) = Distr(NumRing).Weight *
   Image(yc:(yc+NumRing-1),x+xc); % THIS LINE INVERTS

% integration and unfolding
AngIntegrated(yc,x+xc) = Ring(yc,x+xc)*pi*.5^2;
AngIntegrated(yc,-x+xc) = AngIntegrated(yc,x+xc);
Ring(yc,-x+xc) = Ring(yc,x+xc);
for y = 1:NumRing
AngIntegrated(y+yc,x+xc) = Ring(y+yc,x+xc)*pi/2*((y+.5)
   ^2-(y-.5)^2);
AngIntegrated(-y+yc,x+xc) = AngIntegrated(y+yc,x+xc);
AngIntegrated(y+yc,-x+xc) = AngIntegrated(y+yc,x+xc);
AngIntegrated(-y+yc,-x+xc) = AngIntegrated(y+yc,x+xc);

Ring(-y+yc,x+xc) = Ring(y+yc,x+xc);
Ring(y+yc,-x+xc) = Ring(y+yc,x+xc);
Ring(-y+yc,-x+xc) = Ring(y+yc,x+xc);
end
end
```

Bibliography

[1] Tamás Rozgonyi, Thomas Feurer, and Leticia González. A ms-caspt2 study of the low-lying electronic excited states of ch 2 brcl. *Chemical physics letters*, 350(1):155–164, 2001.

[2] Dominik Geißler, Tamás Rozgonyi, Jesús González-Vázquez, Leticia González, Philipp Marquetand, and Thomas C Weinacht. Pulse-shape-dependent strong-field ionization viewed with velocity-map imaging. *Physical Review A*, 84(5):053422, 2011.

[3] Thomas Brabec and Ferenc Krausz. Intense few-cycle laser fields: Frontiers of nonlinear optics. *Reviews of Modern Physics*, 72(2):545, 2000.

[4] Hanieh Fattahi, Helena G Barros, Martin Gorjan, Thomas Nubbemeyer, Bidoor Alsaif, Catherine Y Teisset, Marcel Schultze, Stephan Prinz, Matthias Haefner, Moritz Ueffing, et al. Third-generation femtosecond technology. *Optica*, 1(1):45–63, 2014.

[5] T Baumert, V Engel, Ch Meier, and G Gerber. High laser field effects in multiphoton ionization of na2. experiment and quantum calculations. *Chemical physics letters*, 200(5):488–494, 1992.

[6] M Protopapas, Christoph H Keitel, and Peter L Knight. Atomic physics with super-high intensity lasers. *Reports on Progress in Physics*, 60(4):389, 1997.

[7] Alexander Pukhov. Strong field interaction of laser radiation. *Reports on progress in Physics*, 66(1):47, 2002.

[8] Ahmed H Zewail. Femtochemistry: Recent progress in studies of dynamics and control of reactions and their transition states. *The Journal of Physical Chemistry*, 100(31):12701–12724, 1996.

[9] MF Kling, Ch Siedschlag, Aart J Verhoef, JI Khan, Martin Schultze, Th Uphues, Yicheng Ni, Matthias Uiberacker, M Drescher, Ferenc Krausz, et al. Control of electron localization in molecular dissociation. *Science*, 312(5771):246–248, 2006.

[10] Wen Li, Agnieszka A Jaroń-Becker, Craig W Hogle, Vandana Sharma, Xibin Zhou, Andreas Becker, Henry C Kapteyn, and Margaret M Murnane. Visualizing electron rearrangement in space and time during the transition from a molecule to atoms. *Proceedings of the National Academy of Sciences*, 107(47):20219–20222, 2010.

[11] Moritz Meckel, D Comtois, D Zeidler, Andre Staudte, D Pavičić, HC Bandulet, H Pépin, JC Kieffer, R Dörner, DM Villeneuve, et al. Laser-induced electron tunneling and diffraction. *Science*, 320(5882):1478–1482, 2008.

[12] T Tajima and JM Dawson. Laser electron accelerator. *Physical Review Letters*, 43(4):267, 1979.

[13] F Albert, AGR Thomas, SPD Mangles, S Banerjee, Sébastien Corde, Alessandro Flacco, M Litos, D Neely, J Vieira, Z Najmudin, et al. Laser wakefield accelerator based light sources: potential applications and requirements. *Plasma Physics and Controlled Fusion*, 56(8):084015, 2014.

[14] Pierre Agostini and Louis F DiMauro. The physics of attosecond light pulses. *Reports on progress in physics*, 67(6):813, 2004.

[15] Ferenc Krausz and Misha Ivanov. Attosecond physics. *Reviews of Modern Physics*, 81(1):163, 2009.

[16] P áB Corkum and Ferenc Krausz. Attosecond science. *Nature Physics*, 3(6):381–387, 2007.

[17] Pierre Agostini, F Fabre, Gérard Mainfray, Guillaume Petite, and N Ko Rahman. Free-free transitions following six-photon ionization of xenon atoms. *Physical Review Letters*, 42(17):1127, 1979.

[18] M Bashkansky, PH Bucksbaum, and DW Schumacher. Asymmetries in above-threshold ionization. *Physical review letters*, 60(24):2458, 1988.

[19] RR Freeman, PH Bucksbaum, H Milchberg, S Darack, D Schumacher, and ME Geusic. Above-threshold ionization with subpicosecond laser pulses. *Physical review letters*, 59(10):1092, 1987.

[20] RR Freeman and PH Bucksbaum. Investigations of above-threshold ionization using subpicosecond laser pulses. *Journal of Physics B: Atomic, Molecular and Optical Physics*, 24(2):325, 1991.

[21] P Agostini, P Breger, A Lhuillier, HG Muller, G Petite, A Antonetti, and A Migus. Giant stark shifts in multiphoton ionization. *Physical review letters*, 63(20):2208, 1989.

[22] P Agostini, A Antonetti, P Breger, M Crance, A Migus, HG Muller, and G Petite. Resonant multiphoton ionisation of xenon with high-intensity femtosecond pulses. *Journal of Physics B: Atomic, Molecular and Optical Physics*, 22(12):1971, 1989.

[23] P Kruit, J Kimman, Harm G Muller, and MJ Van der Wiel. Electron spectra from multiphoton ionization of xenon at 1064, 532, and 355 nm. *Physical Review A*, 28(1):248, 1983.

[24] François Yergeau, Guillaume Petite, and Pierre Agostini. Above-threshold ionisation without space charge. *Journal of Physics B: Atomic and Molecular Physics*, 19(19):L663, 1986.

[25] LV Keldysh et al. Ionization in the field of a strong electromagnetic wave. *Sov. Phys. JETP*, 20(5):1307–1314, 1965.

[26] Farhad HM Faisal. Multiple absorption of laser photons by atoms. *Journal of Physics B: Atomic and Molecular Physics*, 6(4):L89, 1973.

[27] Howard R Reiss. Effect of an intense electromagnetic field on a weakly bound system. *Physical Review A*, 22(5):1786, 1980.

[28] MV Ammosov, NB Delone, V Krainov, A Perelomov, V Popov, M Terentev, Gennady L Yudin, and Misha Yu Ivanov. Tunnel ionization of complex atoms and of atomic ions in an alternating electric field. *Sov. Phys. JETP*, 64:1191, 1986.

[29] AM Perelomov, VS Popov, and MV Terentev. Ionization of atoms in an alternating electric field. *Sov. Phys. JETP*, 23(5):924–934, 1966.

[30] Michael Spanner, Serguei Patchkovskii, Congyi Zhou, Spiridoula Matsika, Marija Kotur, and Thomas C Weinacht. Dyson norms in xuv and strong-field ionization of polyatomics: Cytosine and uracil. *Physical Review A*, 86(5):053406, 2012.

[31] G Steinmeyer, DH Sutter, L Gallmann, N Matuschek, and U Keller. Frontiers in ultrashort pulse generation: pushing the limits in linear and nonlinear optics. *Science*, 286(5444):1507–1512, 1999.

[32] L Bergé, S Skupin, R Nuter, Jérôme Kasparian, and Jean-Pierre Wolf. Ultrashort filaments of light in weakly ionized, optically transparent media. *Reports on progress in physics*, 70(10):1633, 2007.

[33] Patrick Nurnberger. Desing and construction of an apparatus for the neutral dissociation and ionization of molecules in an intense laser field. *Master's Thesis*, 2003.

[34] Carlos Trallero. Strong field coherent control. *PhD Thesis*, 2007.

[35] Peter Sandor. Molecular strong field viewed with photoelectron velocity map imaging. *PhD Thesis*, 2016.

[36] David W Chandler and Paul L Houston. Two-dimensional imaging of state-selected photodissociation products detected by multiphoton ionization. *The Journal of chemical physics*, 87(2):1445–1447, 1987.

[37] André TJB Eppink and David H Parker. Velocity map imaging of ions and electrons using electrostatic lenses: Application in photoelectron and photofragment ion imaging of molecular oxygen. *Review of Scientific Instruments*, 68(9):3477–3484, 1997.

[38] GW Fraser. The ion detection efficiency of microchannel plates (mcps). *International Journal of Mass Spectrometry*, 215(1):13–30, 2002.

[39] N Takahashi, Y Adachi, M Saito, and Y Haruyama. Absolute detection efficiencies for kev energy atoms incident on a microchannel plate detector. *Nuclear Instruments and Methods in Physics Research Section B: Beam Interactions with Materials and Atoms*, 315:51–54, 2013.

[40] Joseph Ladislas Wiza. Microchannel plate detectors. *Nuclear Instruments and Methods*, 162(1-3):587–601, 1979.

[41] Joachim Ullrich, Robert Moshammer, Alexander Dorn, Reinhard Dörner, L Ph H Schmidt, and H Schmidt-Böcking. Recoil-ion and electron momentum spectroscopy: reaction-microscopes. *Reports on Progress in Physics*, 66(9):1463, 2003.

[42] Arno Vredenborg, Wim G Roeterdink, and Maurice HM Janssen. A photoelectron-photoion coincidence imaging apparatus for femtosecond time-resolved molecular dynamics with electron time-of-flight resolution of σ= 18 ps and energy resolution δ e/ e= 3.5%. *Review of Scientific Instruments*, 79(6):063108, 2008.

[43] T Poikela, J Plosila, T Westerlund, M Campbell, M De Gaspari, X Llopart, V Gromov, R Kluit, M van Beuzekom, F Zappon, et al. Timepix3: a 65k channel hybrid pixel readout chip with simultaneous toa/tot and sparse readout. *Journal of instrumentation*, 9(05):C05013, 2014.

[44] Andrei Nomerotski, I Chakaberia, M Fisher-Levine, Z Janoska, P Takacs, and T Tsang. Characterization of timepixcam, a fast imager for the time-stamping of optical photons. *Journal of Instrumentation*, 12(01):C01017, 2017.

[45] Lutz Fechner, Nicolas Camus, Andreas Krupp, Joachim Ullrich, Thomas Pfeifer, and Robert Moshammer. Creation and survival of autoionizing states in strong laser fields. *Physical Review A*, 92(5):051403, 2015.

[46] B van der Heijden, J Visser, M van Beuzekom, H Boterenbrood, S Kulis, B Munneke, and F Schreuder. Spidr, a general-purpose readout system for pixel asics. *Journal of Instrumentation*, 12(02):C02040, 2017.

[47] Xavier Llopart, Rafael Ballabriga, Michael Campbell, Lukas Tlustos, and Winnie Wong. Timepix, a 65k programmable pixel readout chip for arrival time, energy and/or photon counting measurements. *Nuclear Instruments and Methods in Physics Research Section A: Accelerators, Spectrometers, Detectors and Associated Equipment*, 581(1):485–494, 2007.

[48] Vladimir Dribinski, Alexei Ossadtchi, Vladimir A Mandelshtam, and Hanna Reisler. Reconstruction of abel-transformable images: The gaussian basis-set expansion abel transform method. *Review of Scientific Instruments*, 73(7):2634–2642, 2002.

[49] Gustavo A Garcia, Laurent Nahon, and Ivan Powis. Two-dimensional charged particle image inversion using a polar basis function expansion. *Review of Scientific Instruments*, 75(11):4989–4996, 2004.

[50] G. N. Gibson, R. R. Freeman, and T. J. McIlrath. Dynamics of the high-intensity multiphoton ionization of n2. *Phys. Rev. Lett.*, 67:1230–1233, Sep 1991.

[51] H. Akagi, T. Otobe, A. Staudte, A. Shiner, F. Turner, R. Drner, D. M. Villeneuve, and P. B. Corkum. Laser tunnel ionization from multiple orbitals in hcl. *Science*, 325(5946):1364–1367, 2009.

[52] Andrey E. Boguslavskiy, Jochen Mikosch, Arjan Gijsbertsen, Michael Spanner, Serguei Patchkovskii, Niklas Gador, Marc J. J. Vrakking, and Albert Stolow. The multielectron ionization dynamics underlying attosecond strong-field spectroscopies. *Science*, 335(6074):1336–1340, 2012.

[53] Marija Kotur, Congyi Zhou, Spiridoula Matsika, Serguei Patchkovskii, Michael Spanner, and Thomas C. Weinacht. Neutral-ionic state correlations in strong-field molecular ionization. *Phys. Rev. Lett.*, 109:203007, Nov 2012.

[54] Wen Li, Xibin Zhou, Robynne Lock, Serguei Patchkovskii, Albert Stolow, Henry C. Kapteyn, and Margaret M. Murnane. Time-resolved dynamics in n2o4 probed using high harmonic generation. *Science*, 322(5905):1207–1211, 2008.

[55] Hong Liu, Song-Feng Zhao, Min Li, Yongkai Deng, Chengyin Wu, Xiao-Xin Zhou, Qihuang Gong, and Yunquan Liu. Molecular-frame photoelectron angular distributions of strong-field tunneling from inner orbitals. *Phys. Rev. A*, 88:061401, Dec 2013.

[56] Brian K. McFarland, Joseph P. Farrell, Philip H. Bucksbaum, and Markus Ghr. High harmonic generation from multiple orbitals in n2. *Science*, 322(5905):1232–1235, 2008.

[57] Michael Spanner, Serguei Patchkovskii, Congyi Zhou, Spiridoula Matsika, Marija Kotur, and Thomas C. Weinacht. Dyson norms in xuv and strong-field ionization of polyatomics: Cytosine and uracil. *Phys. Rev. A*, 86:053406, Nov 2012.

[58] I. Znakovskaya, P. von den Hoff, S. Zherebtsov, A. Wirth, O. Herrwerth, M. J. J. Vrakking, R. de Vivie-Riedle, and M. F. Kling. Attosecond control of electron dynamics in carbon monoxide. *Phys. Rev. Lett.*, 103:103002, Sep 2009.

[59] I. Znakovskaya, P. von den Hoff, N. Schirmel, G. Urbasch, S. Zherebtsov, B. Bergues, R. de Vivie-Riedle, K.-M. Weitzel, and M. F. Kling. Waveform control of orientation-dependent ionization of dcl in few-cycle laser fields. *Phys. Chem. Chem. Phys.*, 13:8653–8658, 2011.

[60] Arthur Zhao, Péter Sándor, Tamás Rozgonyi, and Thomas Weinacht. Removing electrons from more than one orbital: direct and indirect pathways to excited states of molecular cations. *Journal of Physics B: Atomic, Molecular and Optical Physics*, 47(20):204023, 2014.

[61] AF Lago, James P Kercher, András Bödi, Bálint Sztáray, B Miller, D Wurzelmann, and Tomas Baer. Dissociative photoionization and thermochemistry of dihalomethane compounds studied by threshold photoelectron photoion coincidence spectroscopy. *The Journal of Physical Chemistry A*, 109(9):1802–1809, 2005.

[62] Jesús González-Vázquez, Leticia González, Sarah R Nichols, Thomas C Weinacht, and Tamás Rozgonyi. Exploring wavepacket dynamics behind strong-field momentum-dependent photodissociation in ch 2 bri+. *Physical Chemistry Chemical Physics*, 12(42):14203–14216, 2010.

[63] Péter Sándor, Arthur Zhao, Tamás Rozgonyi, and Thomas Weinacht. Strong field molecular ionization to multiple ionic states: direct versus indirect pathways. *Journal of Physics B: Atomic, Molecular and Optical Physics*, 47(12):124021, 2014.

[64] Tomislav Cvitas, Hans Gusten, and Leo Klasinc. Photoelectron spectra of lodobenzenes. *J. Chem. Soc., Perkin Trans. 2*, pages 962–965, 1977.

[65] N. A. Macleod, S. Wang, J. Hennessy, T. Ridley, K. P. Lawley, and R. J. Donovan. Ionic and rydberg states of cf3i studied by high resolution photoelectron (zeke-pfi) and resonance-enhanced multiphoton ionisation spectroscopy. *J. Chem. Soc., Faraday Trans.*, 94:2689–2694, 1998.

[66] Leslie D. Waits, Ronald J. Horwitz, Robert G. Daniel, Joyce A. Guest, and Jeffrey R. Appling. Photofragmentation of cf3i+ produced by resonant multiphoton ionization. *The Journal of Chemical Physics*, 97(10), 1992.

[67] F Aguirre and ST Pratt. Velocity map imaging of the photodissociation of cf 3 i+ in the ã x band. *The Journal of chemical physics*, 119(18):9476–9485, 2003.

[68] Wenzheng Fang, Lei Gong, Qiang Zhang, Xiaobin Shan, Fuyi Liu, Zhenya Wang, and Liusi Sheng. Dissociative photoionization of 1,3-butadiene: Experimental and theoretical insights. *The Journal of Chemical Physics*, 134(17):–, 2011.

[69] XiaoPeng Wang, ShengRui Tong, MaoFa Ge, WeiGang Wang, and DianXun Wang. Photoelectron spectroscopy of terpenoids and prediction of their rate. *Chinese Science Bulletin*, 55(35), 2010.

[70] T. S. Zyubina, A. M. Mebel, M. Hayashi, and S. H. Lin. Theoretical study of multiphoton ionization of cyclohexadienes and unimolecular decomposition of their mono- and dications. *Phys. Chem. Chem. Phys.*, 10:2321–2331, 2008.

[71] A W Potts and G H Fattahallah. High-resolution ultraviolet photoelectron spectroscopy of co 2 , cos and cs 2. *Journal of Physics B: Atomic and Molecular Physics*, 13(13):2545, 1980.

[72] W. Fu, W. E. Schmid, and S. A. Trushin. Time-resolved dissociative intense-laser field ionization for probing dynamics: Femtosecond photochemical ring opening of 1,3-cyclohexadiene. *The Journal of Chemical Physics*, 112(19):8347–8362, 2000.

[73] Ryuji Itakura, Jun Watanabe, Akiyoshi Hishikawa, and Kaoru Yamanouchi. Ionization and fragmentation dynamics of benzene in in-

tense laser fields by tandem mass spectroscopy. *The Journal of Chemical Physics*, 114(13):5598–5606, 2001.

[74] Hideo Harada, Seiji Shimizu, Tomoyuki Yatsuhashi, Shuji Sakabe, Yasukazu Izawa, and Nobuaki Nakashima. A key factor in parent and fragment ion formation on irradiation with an intense femtosecond laser pulse. *Chemical Physics Letters*, 342(56):563 – 570, 2001.

[75] Timothy Bohinski, Katharine Moore Tibbetts, Maryam Tarazkar, Dmitri Romanov, Spiridoula Matsika, and Robert J. Levis. Measurement of an electronic resonance in a ground-state, gas-phase acetophenone cation via strong-field mass spectrometry. *The Journal of Physical Chemistry Letters*, 4(10):1587–1591, 2013.

[76] Brett J. Pearson, Sarah R. Nichols, and Thomas C. Weinacht. Molecular fragmentation driven by ultrafast dynamic ionic resonances. *Journal of Chemical Physics*, 127:131101, 2007.

[77] Péter Sándor, Vincent Tagliamonti, Arthur Zhao, Tamás Rozgonyi, Matthias Ruckenbauer, Philipp Marquetand, and Thomas Weinacht. Strong field molecular ionization in the impulsive limit: Freezing vibrations with short pulses. *Physical Review Letters*, 116(6):063002, 2016.

[78] William DM Lunden, Dominik Geißler, Péter Sándor, Thomas C Weinacht, and Tamás Rozgonyi. Discrimination between strong-field molecular ionization pathways using ultrafast pulse shaping. *Physical Review A*, 89(5):053404, 2014.

[79] R Dorner, Thorsten Weber, Matthias Weckenbrock, Andre Staudte, Mirko Hattass, Robert Moshammer, Joachim Ullrich, and H Schmidt-Bocking. Multiple ionization in strong laser fields. *Advances in Atomic Molecular and Optical Physics*, 48:1–35, 2002.

[80] W Becker and H Rottke. Many-electron strong-field physics. *Contemporary Physics*, 49(3):199–223, 2008.

[81] A l'Huillier, LA Lompre, G Mainfray, and C Manus. Multiply charged ions formed by multiphoton absorption processes in the continuum. *Physical Review Letters*, 48(26):1814, 1982.

[82] D Feldmann, J Krautwald, SL Chin, A Von Hellfeld, and KH Welge. Multiphoton ionisation of strontium creating sr+ and sr2+. *Journal of Physics B: Atomic and Molecular Physics*, 15(11):1663, 1982.

[83] Abdossamad Talebpour, Simon Larochelle, and See-Leang Chin. Non-sequential and sequential double ionization of no in an intense femtosecond ti: sapphire laser pulse. *Journal of Physics B: Atomic, Molecular and Optical Physics*, 30(7):L245–L250, 1997.

[84] Barry Walker, Brian Sheehy, Louis F DiMauro, Pierre Agostini, Kenneth J Schafer, and Kenneth C Kulander. Precision measurement of strong field double ionization of helium. *Physical review letters*, 73(9):1227, 1994.

[85] Paul B Corkum. Plasma perspective on strong field multiphoton ionization. *Physical Review Letters*, 71(13):1994, 1993.

[86] Michael Yu Kuchiev. Atomic antenna. *JETP Lett*, 45(7):404–406, 1987.

[87] VL Bastos de Jesus, Bernold Feuerstein, Karl Zrost, Daniel Fischer, Artem Rudenko, Feras Afaneh, Claus D Schröter, Robert Moshammer, and Joachim Ullrich. Atomic structure dependence of nonsequential double ionization of he, ne and ar in strong laser pulses. *Journal of Physics B: Atomic, Molecular and Optical Physics*, 37(8):L161, 2004.

[88] Robert Moshammer, Bernold Feuerstein, Wolfgang Schmitt, Alexander Dorn, Claus D Schröter, Joachim Ullrich, Horst Rottke, Christoph Trump, Michael Wittmann, Georg Korn, et al. Momentum distributions of ne n+ ions created by an intense ultrashort laser pulse. *Physical review letters*, 84(3):447, 2000.

[89] Th Weber, Harald Giessen, Matthias Weckenbrock, Gunter Urbasch, Andre Staudte, Lutz Spielberger, Ottmar Jagutzki, Volker Mergel, Martin Vollmer, and Reinhard Dörner. Correlated electron emission in multiphoton double ionization. *Nature*, 405(6787):658–661, 2000.

[90] David N Fittinghoff, Paul R Bolton, Britton Chang, and Kenneth C Kulander. Observation of nonsequential double ionization of helium with optical tunneling. *Physical review letters*, 69(18):2642, 1992.

[91] Adrian N Pfeiffer, Claudio Cirelli, Mathias Smolarski, Reinhard Dörner, and Ursula Keller. Timing the release in sequential double ionization. *Nature Physics*, 7(5):428–433, 2011.

[92] Boris Bergues, Matthias Kubel-Schwarz, Nora Kling, Christian Jendrzejewski, and Matthias Kling. Single-cycle non-sequential double ionization. 2015.

[93] Simon Larochelle, Abdossamad Talebpour, and See-Leang Chin. Non-sequential multiple ionization of rare gas atoms in a ti: Sapphire laser field. *Journal of Physics B: Atomic, Molecular and Optical Physics*, 31(6):1201, 1998.

[94] VR Bhardwaj, DM Rayner, DM Villeneuve, and PB Corkum. Quantum interference in double ionization and fragmentation of c 6 h 6 in intense laser fields. *Physical review letters*, 87(25):253003, 2001.

[95] Chunlei Guo, Ming Li, JP Nibarger, and George N Gibson. Single and double ionization of diatomic molecules in strong laser fields. *Physical Review A*, 58(6):R4271, 1998.

[96] KWD Ledingham, RP Singhal, DJ Smith, T McCanny, P Graham, HS Kilic, WX Peng, SL Wang, AJ Langley, PF Taday, et al. Behavior of polyatomic molecules in intense infrared laser beams. *The Journal of Physical Chemistry A*, 102(18):3002–3005, 1998.

[97] C Cornaggia and Ph Hering. Nonsequential double ionization of small molecules induced by a femtosecond laser field. *Physical Review A*, 62(2):023403, 2000.

[98] Chunlei Guo, Ming Li, JP Nibarger, and George N Gibson. Single and double ionization of diatomic molecules in strong laser fields. *Physical Review A*, 58(6):R4271, 1998.

[99] TS Zyubina, AM Mebel, M Hayashi, and SH Lin. Theoretical study of multiphoton ionization of cyclohexadienes and unimolecular decomposition of their mono-and dications. *Physical Chemistry Chemical Physics*, 10(17):2321–2331, 2008.

[100] N Takahashi, S Hosokawa, M Saito, and Y Haruyama. Measurement of absolute detection efficiencies of a microchannel plate using the charge transfer reaction. *Physica Scripta*, 2011(T144):014057, 2011.

[101] Steven M Hankin, David M Villeneuve, Paul B Corkum, and David M Rayner. Nonlinear ionization of organic molecules in high intensity laser fields. *Physical review letters*, 84(22):5082, 2000.

[102] David N Fittinghoff, Paul R Bolton, Britton Chang, and Kenneth C Kulander. Polarization dependence of tunneling ionization of helium and neon by 120-fs pulses at 614 nm. *Physical Review A*, 49(3):2174, 1994.

[103] Peter Dietrich, Neil H Burnett, M Ivanov, and Paul B Corkum. High-harmonic generation and correlated two-electron multiphoton ionization with elliptically polarized light. *Physical Review A*, 50(5):R3585, 1994.

[104] Xu Wang and JH Eberly. Elliptical polarization and probability of double ionization. *Physical review letters*, 105(8):083001, 2010.

[105] Francois Mauger, Cristel Chandre, and Turgay Uzer. Recollisions and correlated double ionization with circularly polarized light. *Physical review letters*, 105(8):083002, 2010.

[106] Haruyuki Nakano. Quasidegenerate perturbation theory with multiconfigurational self-consistent-field reference functions. *The Journal of chemical physics*, 99(10):7983–7992, 1993.

[107] MW Schmidt, KK Baldridge, JA Boatz, ST Elbert, MS Gordon, JH Jensen, S Koseki, N Matsunaga, KA Nguyen, S Su, et al. Computation of conical intersections by using perturbation techniques. *J. Comput. Chem*, 14:1347, 1993.

[108] Clifford Dykstra, Gernot Frenking, Kwang Kim, and Gustavo Scuseria. *Theory and Applications of Computational Chemistry: the first forty years.* Elsevier, 2011.

[109] Yihan Shao, Laszlo Fusti-Molnar, Yousung Jung, Jurg Kussmann, Christian Ochsenfeld, Shawn T Brown, Andrew TB Gilbert, Lyudmila V Slipchenko, Sergey V Levchenko, Darragh P ONeill, et al. Ad-

vances in quantum chemical methods and algorithms in the q-chem 3.0 program package. *Phys Chem Chem Phys*, 8:3172, 2006.

[110] Arno Vredenborg, Wim G Roeterdink, Cornelis A de Lange, and Maurice HM Janssen. Revealing femtosecond multiphoton induced multichannel molecular ionization and fragmentation dynamics by photoelectron–photoion coincidence imaging. *Chemical Physics Letters*, 478(1):20–27, 2009.